National Library of Canada
Bibliothèque nationale du Canada

Canadian Theses Service
Service des thèses canadiennes

Ottawa, Canada
K1A 0N4

NOTICE

The quality of this microform is heavily dependent upon the quality of the original thesis submitted for microfilming. Every effort has been made to ensure the highest quality of reproduction possible.

If pages are missing, contact the university which granted the degree.

Some pages may have indistinct print especially if the original pages were typed with a poor typewriter ribbon or if the university sent us an inferior photocopy.

Previously copyrighted materials (journal articles, published tests, etc.) are not filmed.

Reproduction in full or in part of this microform is governed by the Canadian Copyright Act, R.S.C. 1970, c. C-30.

AVIS

La qualité de cette microforme dépend grandement de la qualité de la thèse soumise au microfilmage. Nous avons tout fait pour assurer une qualité supérieure de reproduction.

S'il manque des pages, veuillez communiquer avec l'université qui a conféré le grade.

La qualité d'impression de certaines pages peut laisser à désirer, surtout si les pages originales ont été dactylographiées à l'aide d'un ruban usé ou si l'université nous a fait parvenir une photocopie de qualité inférieure.

Les documents qui font déjà l'objet d'un droit d'auteur (articles de revue, tests publiés, etc.) ne sont pas microfilmés.

La reproduction, même partielle, de cette microforme est soumise à la Loi canadienne sur le droit d'auteur, SRC 1970, c. C-30.

NL-339 (r. 88/04)

Canada

THE UNIVERSITY OF ALBERTA

SHORT-TERM MICROCLIMATIC CHANGE RESULTING FROM ALTERED AERODYNAMICS IN A SQUARE FENCED PLOT

by

JOSEFINA C. ARGETE

A THESIS

SUBMITTED TO THE FACULTY OF GRADUATE STUDIES AND RESEARCH

IN PARTIAL FULFILMENT OF THE REQUIREMENTS FOR THE DEGREE

OF DOCTOR OF PHILOSOPHY

IN

METEOROLOGY

GEOGRAPHY

EDMONTON, ALBERTA

FALL, 1988

Permission has been granted to the National Library of Canada to microfilm this thesis and to lend or sell copies of the film.

The author (copyright owner) has reserved other publication rights, and neither the thesis nor extensive extracts from it may be printed or otherwise reproduced without his/her written permission.

L'autorisation a été accordée à la Bibliothèque nationale du Canada de microfilmer cette thèse et de prêter ou de vendre des exemplaires du film.

L'auteur (titulaire du droit d'auteur) se réserve les autres droits de publication; ni la thèse ni de longs extraits de celle-ci ne doivent être imprimés ou autrement reproduits sans son autorisation écrite.

ISBN 0-315-45716-3

THE UNIVERSITY OF ALBERTA

RELEASE FORM

NAME OF AUTHOR JOSEFINA C. ARGETE

TITLE OF THESIS SHORT-TERM MICROCLIMATIC CHANGE RESULTING FROM ALTERED AERODYNAMICS IN A SQUARE FENCED PLOT

DEGREE FOR WHICH THESIS WAS PRESENTED DOCTOR OF PHILOSOPHY

YEAR THIS DEGREE GRANTED FALL, 1988

Permission is hereby granted to THE UNIVERSITY OF ALBERTA LIBRARY to reproduce single copies of this thesis and to lend or sell such copies for private, scholarly or scientific research purposes only.

The author reserves other publication rights, and neither the thesis nor extensive extracts from it may be printed or otherwise reproduced without the author's written permission.

(SIGNED) Josefina C. Argete

PERMANENT ADDRESS:
San Francisco St.
Tanza, Cavite
Philippines

DATED 6 Oct 1988

THE UNIVERSITY OF ALBERTA

FACULTY OF GRADUATE STUDIES AND RESEARCH

The undersigned certify that they have read, and recommend to the Faculty of Graduate Studies and Research, for acceptance, a thesis entitled SHORT-TERM MICROCLIMATIC CHANGE RESULTING FROM ALTERED AERODYNAMICS IN A SQUARE FENCED PLOT submitted by JOSEFINA C. ARGETE in partial fulfilment of the requirements for the degree of DOCTOR OF PHILOSOPHY in METEOROLOGY.

.....

Supervisor

.....

.....

.....

.....

.....

.....

External Examiner

Date.....21 April 88.....

Abstract

A series of experiments was conducted at Ellerslie, Alberta to investigate the aerodynamically-induced microclimatic changes in a square plot surrounded by a porous fence. A dimensionless formulation describing transport of a passive scalar whose surface emission rate is spatially constant was derived in analogy to diffusion of a gas from a ground-level area source. This formulation involved a scaled equivalent temperature $\Delta\bar{T}_{eq}/T_{eq_*}$ where $T_{eq} = T + \frac{\epsilon}{\gamma}$ measures the total thermodynamic energy content of the air and the normalizing variable T_{eq_*} is the slope (with respect to the logarithm of the height) of the T_{eq} profile of the approach flow. Since the flux density of total energy, which is the sum of the surface sensible and latent heat flux densities, may be assumed to be reasonably constant across the field, differences in T_{eq} between the approach flow and the plot measured at a common height reflect changes in flow due to the fence. Wind reduction was expressed as $\Delta\bar{u}/\bar{u}_o$. The dependence of $\Delta\bar{u}/\bar{u}_o$, $\Delta\bar{T}_{eq}/T_{eq_*}$ are presented as functions of the following parameters: $\frac{z}{H}$ measurement height; $\frac{x}{H}$ horizontal extent; $\frac{H}{z_o}$ surface roughness parameter; $\frac{H}{L}$ atmospheric stability parameter; $\frac{D}{H}$ aspect ratio; and β wind direction (where H is the fence height).

The results were interpreted in the light of the known existence of the quiet and turbulent zones in the lee of a barrier. Based on the fact that the diffusivity is related to both the size (i.e., length scale) and intensity (i.e., velocity scale) of turbulent motions, it is expected qualitatively that turbulent transport of energy

will be less efficient in the quiet zone where eddy size and intensity are reduced, and conversely for the turbulent zone. Turbulence (σ_w) measurements indicated a quiet zone condition prevailing in the center of the small plot ($\frac{D}{H} = 8; \frac{z}{H} = 4$) and the opposite for that of the big plot ($\frac{D}{H} = 16; \frac{z}{H} = 8$). The scaled T_{eq} was consistently positive (warming in T_{eq}) in the former and negative (cooling in T_{eq}) in the latter for all daytime unstable runs ($\frac{H}{L} \lesssim 0$). Nightime stable runs ($\frac{H}{L} > 0$) showed the reverse. The magnitude of the scaled T_{eq} in the center of the small plot was found to be influenced by $\frac{z}{H}$ and $\frac{H}{z_o}$ only for near-neutral runs, but with increasing instability ($\frac{H}{L} \to -1$), $|\Delta\tilde{T}_{eq}/T_{eq\cdot}| \to 0$ regardless of $\frac{z}{H}, \frac{H}{z_o}$, suggesting a shortened extent of the daytime quiet zone. Interpolation from the u, T_{eq} and σ_w data, sets this horizontal extent at $\frac{z}{H} \approx 5$ compared to $\frac{z}{H} \approx 7 - 8$ for a long straight fence of similar porosity. These results imply that in the agronomic practice of sheltering, rather small plots have to be employed in order to obtain a shelter benefit other than a reduction in windspeed, viz., reduced turbulence and possibly evapotranspiration.

ACKNOWLEDGEMENT

I would like to thank a number of people who have significantly contributed to the completion of this thesis. Dr. John D. Wilson shared his scientific expertise on windbreak flow and spent an inordinate amount of time going over the manuscript in its many transformations. The field experiments would not have been possible without the assistance of Terry Thompson (Division of Meteorology) for technical support; Ray Holowach and Steve Melnyk (U of A Farm, Ellerslie) for the use of the experimental site; and Claude Labine (Campbell Scientific, Canada) for loaning us the sonic anemometers.

The Tensar Corporation provided the windbreak material.

The members of the examining committee: Dr. T. Gillespie (Department of Land Resource Science, University of Guelph), Dr. R.B. Charlton and Dr. E.P. Lozowski (Division of Meteorology, University of Alberta), Dr. D. Chanasyk (Department of Soil Science, U of A), and Dr. K. Fairbairn (Department of Geography, U of A), carefully reviewed the manuscript and corrected a large number of mistakes. Those which remain are, of course, entirely my own responsibility.

The Department of Geography granted financial support in the form of a three-year graduate assistantship.

Finally, Kais Al-Jumily provided emotional support during difficult times.

TABLE OF CONTENTS

CHAPTER		PAGE
I.	INTRODUCTION	1
II.	UNDISTURBED SURFACE LAYER FLOW	9
	Introduction	9
	Governing Equations	10
	Constant Flux Layer	13
	The Closure Problem	14
	First-Order Closure	14
	Second-Order Closure	16
	The Logarithmic Wind Profile	17
	Monin-Obukhov Similarity	18
	Estimation of Φ for Diabatic Profiles	23
III.	WINDBREAK FLOW	29
	Introduction	29
	Internal Boundary Layer Flow	30
	Windbreak Aerodynamics	32
	Overview	32
	Governing Equations	34
	Quiet and Turbulent Zones	36
	Other Factors Influencing Windbreak Flow	42
	Microclimate Modification	45
	Considerations in Describing Transport of Passive Scalars in Shelter	45
	Scaling Analogy to the Diffusion Problem from a Ground Level Area Source	48
	Expected Trends of $\Delta\bar{T}_{eq}/T_{eq}$. in Shelter	52
IV.	EXPERIMENTAL PROCEDURE	59
	Site Description	59
	Set-Up and Measurements	61

CHAPTER PAGE

Diode Psychrometry 65
Diodes as Temperature Sensors 65
Construction of the Diode Sensors 67
Description of the Psychrometer Assembly 69
Laboratory Calibrations 72
Field Comparisons 74
Sources of Error in Psychrometry 76
Definition of T_{eq}, T_w 77

V. DATA ANALYSIS 82

Determination of z_o, d 82
Determination of u_*, T_* and T_{eq*} 85
Moisture Correction for L, T_{v*} 85
The Least-Squares Procedure 86
Criteria for Selection of Acceptable Runs 96
Determination of Q_H and Q_{LE} 99
Determination of σ_w 100

VI. RESULTS AND DISCUSSION 106

Trends in windspeed reduction $\Delta\bar{u}/\bar{u}_o$ 106
Influence of $\beta, \frac{z}{H}, \frac{D}{H}$ 106
Influence of $\frac{H}{L}, \frac{H}{z_o}$ 112
Trends of w' in the quiet and turbulent zones 116
Trends in $\Delta\bar{T}_{eq}/T_{eq*}$ 120
Influence of $\frac{D}{H}$ 121
Influence of $\frac{H}{L}, \frac{H}{z_o}, \frac{z}{H}$ 124
Influence of $\beta, \frac{z}{H}$ 128
Trends of $\Delta\bar{T}_{eq}/T_{eq*}$ under stable stratification 133

VII. SUMMARY 137

BIBLIOGRAPHY 140

LIST OF TABLES

TABLE		PAGE
2.1	Qualitative interpretation of $\xi = \frac{z}{L}$ and Ri_g.	24
4.1	Summary of measurements.	66
5.1	PROAN.BAS input and results for a representative unstable stratification run.	90
5.2	PROAN.BAS input and results for a representative near-neutral run.	91
5.3	PROAN.BAS input and results for a representative stable stratification run.	92
6.1	Scaled T_{eq} interpretation.	121

LIST OF FIGURES

FIGURE		PAGE
2.1	Plot of Φ_M as a function of $\frac{z}{L}$.	26
2.2	Plot of Φ_H as a function of $\frac{z}{L}$.	27
3.1	Schematic representation of the development of an internal boundary layer: flow from smooth to rough.	31
3.2	Streamline sketches of windbreak flow.	33
3.3	Schematic representation of turbulence in the wake and quiet zone behind a model windbreak.	37
3.4	Profile of $\bar{u}/\bar{u}_H$ referred to streamline coordinate axes.	39
3.5	Variations of $\bar{u}/\bar{u}_H$ along streamlines.	39
3.6	Profiles of $-\overline{u'w'}/u_H^2$ and $\bar{e}/u_H^2$.	40
3.7	Horizontal profiles of the normalized variance of v, w at $\frac{z}{H} = 0.5$ and of w at $\frac{z}{H} = 1$.	40
3.8	Two-dimensional diffusion problem; the downwind concentration $c(x,z)$ of a gas diffusing from a ground level area source of strength Q_A and with the wind constant with height.	51
3.9	Schematic and partly speculative representation of $\Delta T_{eq}/T_{eq}$. across a sheltered field where available energy is uniform $[H/z_o = 150, -0.05 < \frac{H}{L} < 0, \phi = 50\%]$.	53
3.10	Map of the horizontal and vertical fluxes Q_{cx} and Q_{cz} on a surface layer disturbed by a fenced plot.	55

FIGURE		PAGE
3.11	Expected changes in T_{eq} in a fenced plot during the day (unstable stratification) at two observation points: (a) turbulent zone and (b) quiet zone.	57
4.1	Field layout.	60
4.2	Experimental set-up.	62
4.3	Actual size trace of the 45% porosity Tensar fence.	63
4.4	Mounting of the IN270 germanium diode.	73
4.5	Circuit diagram of the diode psychrometer setup.	70
4.6	Cross-section of the diode psychrometer assembly.	71
4.7	Typical calibration curves and regression equations for a diode pair.	73
4.8	Psychrometer corrections determined at various dates of field calibrations: (a) August, 1986; (b) October, 1986 and (c) April-May, 1987.	75
4.9	Adiabatic isobaric process showing T_{eq} and T_w on a vapor pressure - temperature diagram.	81
5.1	Graphical method of determining z_o.	84
5.2	Approch flow theoretical and measured profiles of the wind for three representative runs.	93
5.3	Same as in Figure 5.2 but for dry-bulb temperature.	94
5.4	Same as in Figure 5.2 but for equivalent temperature.	95
5.5	Trends of u_*, T_*, T_{v*} and T_{eq*} with time of day.	98

FIGURE		PAGE
5.6	Comparison of sensible heat flux Q_H [W/m^2] determined by the gradient method and by direct measurement using eddy correlation.	101
5.7	Comparison of the total energy flux $Q_H + Q_{LE}$, [W/m^2] determined by gradient method and by direct measurement using the combined energy balance and eddy correlation approach.	102
5.8	Field comparison of two sonic anemometers positioned at $z =$ 0.31 m. Each data point represents σ_w [m/s] averaged over a 15-min period.	104
5.9	Variation of σ_w/u_* with $\frac{z}{L}$ ($z = 0.31$m) in the approach flow.	105
6.1	Plot of wind reduction $\Delta\bar{u}/\bar{u}_o$ taken at the center of the four quadrants of the big plot ($\frac{D}{H} = 16, \frac{z}{H} = 0.5, \frac{H}{z_o} = 25$) as a function of wind direction β.	107
6.2	Data points of Figure 6.1 plotted as a function of the scaled horizontal distance $\frac{x}{H}$.	110
6.3	Wind reduction for two plot sizes: (i) $\frac{D}{H} = 8$, (ii) $\frac{D}{H} = 16$; as a function of β, with $\frac{z}{H} = 0.5, \frac{H}{z_o} = 25$.	111
6.4	Wind reduction for two plot sizes: (i) $\frac{D}{H} = 8$, (ii) $\frac{D}{H} = 16$; with atmospheric stability ranging from near-neutral to unstable and with $\frac{z}{H} = 0.5, \frac{H}{z_o} = 25$.	113
6.5	Wind reduction for the small plot ($\frac{D}{H} = 8, \frac{z}{H} = 0.5$) at two values of surface roughness: (i) $\frac{H}{z_o} = 25$, (ii) $\frac{H}{z_o} = 200$; as a function of β.	115
6.6	Scaled standard deviation of w' at two plot sizes: (i) $\frac{D}{H} = 8$, (ii) $\frac{D}{H} = 16$; with atmospheric stability ranging from near-neutral to unstable and with $\frac{z}{H} = 0.25, \frac{H}{z_o} = 200$.	117

FIGURE		PAGE
6.7	Scaled standard deviation of w' for the small plot ($\frac{D}{H} = 8, \frac{z}{H} = 0.25, \frac{H}{z_o} = 200$) as a function of β for two stability classes: (i) near-neutral to unstable, (ii) stable stratification.	118
6.8	Standard deviation of w' for the big plot as a function of β for near-neutral to unstable runs.	119
6.9	Scaled T_{eq} at two plot sizes and at $\frac{z}{H} = 0.5; \frac{H}{z_o} = 25$ with atmospheric stability ranging from near-neutral to unstable.	122
6.10	Scaled T_{eq} at two plot sizes and at $\frac{z}{H} = 0.25; \frac{H}{z_o} = 200$ with atmospheric stability ranging from near-neutral to unstable.	123
6.11	Scaled T_{eq} comparison in the small plot: (i) $\frac{z}{H} = 0.25, \frac{H}{z_o} = 200$; (ii) $\frac{z}{H} = 0.50, \frac{H}{z_o} = 25$.	126
6.12	Scaled T_{eq} comparison in the big plot.	127
6.13	Influence of wind direction β on wind reduction and scaled T_{eq} in the center of the small plot: $\frac{z}{H} = 0.50; \frac{H}{z_o} = 25$.	129
6.14	Influence of β on wind reduction and scaled T_{eq} in the center of the big plot: $\frac{z}{H} = 0.50; \frac{H}{z_o} = 25$.	130
6.15	Influence of β on scaled T_{eq} in the small and big plots: $\frac{z}{H} = 0.25; \frac{H}{z_o} = 200$.	131
6.16	Horizontal profiles of mean wind reduction and scaled T_{eq} based on measurements in the center and four quadrants of the big plot.	132
6.17	Variation of scaled T_{eq} with $\frac{H}{L}$ under stable stratification.	135

LIST OF SYMBOLS

B	Bowen ratio
c	local gas concentration
C_d	drag coefficient of fence
c_p	specific heat of air at constant pressure
c_*	gas concentration scale
D	fence sidelength
D	molecular diffusivity of matter
d	displacement height
d_p	fence-protected horizontal distance (zone within which $\bar{u}/\bar{u}_o \leq 0.8$)
E	evaporative flux density
e	vapor pressure
e	turbulent kinetic energy
g	acceleration due to gravity
H	fence height
h	crop height
k	von Karman's constant
K_{ij}	eddy transfer coefficient in tensor form
$K_{M,H,W}$	scalar eddy transfer coefficient for momentum, heat and water vapor
k_r	fence resistance coefficient
L	Monin-Obukhov length
l	turbulent length scale
L_v	latent heat of vaporization
m_d	mean molecular weight for dry air
m_w	mean molecular weight for water vapor
P	pressure scale
p	atmospheric pressure
q	turbulent velocity scale
q	specific humidity
Q_A	area source strength
Q_{cz}	horizontal energy flux density
Q_{cz}	vertical energy flux density
Q_G	soil heat flux density

Q_H	sensible heat flux density
Q_L	line source strength
Q_{LE}	latent heat flux density
Q_*	net radiation flux density
R	gas constant for dry air
r	mixing ratio
R_*	universal gas constant $(= R_*/m_d)$
Re	Reynold's number
Ri_c	critical Richardson number
Ri_f	flux Richardson number
Ri_g	gradient Richardson number
S_E	source term for turbulent kinetic energy
S_H	heat source term
S_Q	sink term for total energy
S_U	horizontal momentum source term
S_V	water vapor source term
S_W	vertical momentum source term
T	dry-bulb temperature
t	time
T_{eq}	equivalent temperature
T_{eq*}	equivalent temperature scale
T_o	temperature of reference state
T'	perturbation temperature
T_*	surface layer temperature scale
T_{v*}	virtual temperature scale
T_v	virtual temperature
T_w	wet-bulb temperature
u	horizontal velocity component
u_i	velocity components $(i = 1, 2, 3)$
u_*	friction velocity
v	lateral velocity component
w	vertical velocity component
x_i	spatial coordinates $(i = 1, 2, 3)$
x	horizontal cooordinate $(i = 1)$
y	lateral coordinate $(i = 2)$
z	vertical coordinate $(i = 3)$
z_o	roughness length

Greek letters

α	exchange coefficient ratio
β	wind direction (degrees)
γ	psychrometric constant $(= \frac{c_p P}{\epsilon L_v})$
γ_d	dry adiabatic lapse rate
Δ	difference from upstream value
δ_{ij}	Kronecker delta: $\delta_{ij} = 1$ if $i = j$
δ_{IBL}	IBL depth
δ_{PBL}	PBL depth
ϵ	$\frac{M_a}{M_w} = 0.622$
ε	turbulent kinetic energy dissipation rate
κ	thermal diffusivity of air
λ	scaling length for stable boundary layer
ν	kinematic viscosity of air
ξ	dimensionless height
ρ	air density
ρ_o	representative density of the surface layer
ρ_v	absolute humidity
ρ_{v*}	absolute humidity scale
σ_β	standard deviation of wind direction
$\sigma_{u,v,w}$	standard deviation of horizontal, lateral and vertical velocity fluctuations
τ	surface shear stress
ϕ	fence porosity
$\Phi_{M,H,W}$	dimensionless wind, temperature and vapor pressure gradients in the surface layer
ψ	integrated forms of the Φ functions
$\vec{\Omega}$	earth rotation vector

Subscripts

m	measured value of a variable
t	theoretical value of a variable
o	upstream reference value of a variable

Superscripts

D	non-dimensional variable
p	plot measurements
t	tower measurements

CHAPTER I

INTRODUCTION

Shelterbelts and windbreaks are agricultural devices used by man since time immemorial, primarily as a protection against strong winds. This is evident in the network of trees in the Rhone Valley which, because of its topography, is often exposed to gusting valley winds, and the extensive shelterbelt project in the Great Plains of the United States and the Prairie Provinces of Canada where the topsoil can be lifted off the ground and carried away in duststorms. Stated in broad terms, the ultimate goal of shelter researchers is to provide design guidelines for such purposes as increasing crop yields; protecting livestock, farm steads and home sites; controlling snow drifts and reducing erosion. Windbreaks in use may consist of stubble strips, trees or shrubs, fences, reed mats, or porous cloth. As well, the choice of a windbreak depends on such factors as establishment and maintenance costs, delay in establishment, portability, shading, water use, disease and pest control, etc.

It is convenient to view the changes produced by windbreaks in three stages. First, windbreaks change the airflow in their vicinity. Second, the changed airflow patterns produce a microclimate and soil climate different from those in the open field. Finally, the altered microclimate and soil climate in the sheltered area pro-

duce a response in plants, livestock, etc. Of course in reality, these changes are interrelated and cannot in general be viewed in isolation from each other.

The shelter effect has been a topic of study in agronomy, forestry, agricultural engineering and micrometeorology for several decades and the resulting literature is voluminous. Comprehensive reviews are given by van Eimern et al. (1964), Rosenberg (1979) and Alcorn and Dodd (1984). Most of the work is empirical, being mainly concerned with measuring reductions in mean wind speed, evaporation and more recently the changes in turbulence carried by this wind. Little attempt has been made to model theoretically the flow across the windbreak for a reason which is not difficult to understand. For complete treatment, the analytical solution to the windbreak problem requires solution of the time-averaged Navier-Stokes equation which is not possible. The complexity of the problem is exemplified in the review of Plate (1971a) where no less than seven distinctive regimes of flow in the vicinity of the windbreak are proposed. Nevertheless, some workers (Kaiser, 1959; Counihan et al., 1974; Wilson, 1988) have given analytical solutions for a two-dimensional turbulent flow across the windbreak with limited success. This explains the preference for empirical descriptions of windbreak flow based on field and wind-tunnel data. Aside from the ease in making measurements on scale models, the experimental conditions can be easily controlled. The specific factors controlling the flow can be studied separately or in combination and without the added complication of vegetation responses. Moreover, similarity requirements are now sufficiently well understood to allow translation of model results to full-scale shelters.

The situation of least complexity is the case of a long thin fence standing per-

pendicular to the wind on a large flat horizontally-uniform field. The similarity law for windspeed reduction $\frac{\Delta \bar{u}}{\bar{u}_o}$ may be deduced by dimensional analysis to be

$$\frac{\Delta \bar{u}}{\bar{u}_o} = f(\frac{x}{H}, \frac{z}{H}, \frac{H}{z_o}, \frac{H}{L}, \phi, k_r, \frac{\bar{u}_o H}{\nu}, \frac{\delta_{PBL}}{H}) \qquad (1.1)$$

where f denotes a universal function that describes wind flow about the fence. Here, $\Delta \bar{u}$ is the difference between the mean windspeed in the open $\bar{u}_o$ and that in any position in the lee, H is the height of the fence of uniform porosity ϕ and resistance coefficient k_r, z_o is the roughness length, L is the Monin-Obukhov length and δ_{PBL} is the planetary boundary layer depth. The Reynolds number $Re = \frac{\bar{u}_o H}{\nu}$ is so large in the atmosphere that the flow becomes independent of Re. Establishing quantitative relations between these dimensionless parameters and windspeed reduction became the concern of many windbreak researchers in the past ten years.

One of the most illuminating wind tunnel experiments is that of Raine and Stevenson (1977). These authors showed that the leeward zone consists of (i) a triangular *quiet* zone of reduced turbulence and smaller eddy size immediately behind the fence; and (ii) an extended *wake* region of increased turbulence. The quiet zone extends from the top of the fence to the surface at about eight fence-heights ($\frac{x}{H} = 8$), the extent varying slightly as conditions depart from the experiment's reference case of a 50% porous fence. A detailed discussion of the aerodynamic aspects of windbreak flow is given in Chapter III.

The microclimate modification in the lee of a windbreak is closely linked to the aerodynamic effect; in fact, the former may be considered a consequence of the latter. However, a description of the microclimatic influence of the windbreak cannot

be obtained solely from a knowledge of momentum transport, inasmuch as microclimatic processes involve transport of scalars. For example, behind a solid windbreak where bleed flow does not occur, the drag on the ground is negative or towards the fence in the reverse flow area very close to the fence, zero at the stagnation point and positive further on. This same pattern does not hold for heat and mass transport. At the stagnation point where eddy contributions to momentum transfer cancel each other, the net heat or mass transport is not necesarily zero.

Microclimate is the sum of many interacting elements, so that a shelter effect may also be measured in terms of a change in the radiation and energy balance of the crops in the lee, air and soil temperatures, humidity, carbon dioxide concentration and the concentration of pollutants. Of prime concern to agriculture is evaporation, a process driven by differences in temperature and humidity between the evaporating surface and the air (and modulated by resistances such as stomatal resistance which are themselves linked to the microclimatic state). Information on patterns of heat and mass transport behind windbreaks is therefore a prerequisite to determining the efficiency of a windbreak in altering evaporation in its lee.

The level of research on heat and mass tranport behind windbreaks is currently comparable to studies of the aerodynamic aspect a decade ago, from which in retrospect few insights into heat and mass transport can be gained. Experimental conditions were poorly defined, results were not scaled for easy comparison with the results of others, and the problem was not examined in wind tunnel simulations.

The problem can be approached using the concept of the quiet and turbulent

zones. Based on the fact that the diffusivity is related to both the size (i.e., length scale) and intensity (i.e., velocity scale) of turbulent motion, it is expected qualitatively that turbulent transport of heat and mass will be less efficient in the quiet zone where eddy sizes are small and velocity scales reduced, and conversely for the wake. Some field results confirm this. Hagen and Skidmore (1971) recorded a rise in surface temperature behind their slat-fence windbreaks to about $\frac{x}{H} = 6$ for very low porosity fences (to about $\frac{x}{H} = 10$ for higher porosity fences); beyond these points, cooling was observed. Woodruff et al. (1959) reported similar results for their full-scale shelterbelt. In the latter case, the warm zone extended only to about $\frac{x}{H} = 4$. This reduced extent may likely be attributed to a change in atmospheric stability.

There is a catch here. One cannot attribute changes in temperature solely to the alteration in the aerodynamic regime, unless the surface heat flux density Q_H is spatially uniform, and there is no reason to assume the sensible heat flux to be unaltered by the fence. In both the above experiments, the importance of this assumption was not mentioned.

In contrast the available energy $(Q_* - Q_G)$ where Q_* is the net radiant energy and Q_G is the soil heat flux may often reasonably be assumed constant across the field because there is no reason to expect alteration of incoming fluxes or large changes in albedo or surface temperature. From the energy balance

$$Q_* - Q_G = Q_H + Q_{LE} \tag{1.2}$$

the available energy is partitioned into latent and sensible heat fluxes. It follows

that even if the fluxes of sensible and latent heat, Q_H and Q_{LE}, may vary, their sum will be reasonably constant across the field. This is true of $(Q_* - Q_G)$, which should be constant provided there are no shadows cast and the outgoing longwave is not substantially altered (a reasonable assumption if the changes in surface temperature are small).

A measure of the total thermodynamic energy content of the air is the equivalent temperature, T_{eq}, defined as

$$T_{eq} = T + \frac{e}{\gamma} \tag{1.3}$$

where T and e are the dry bulb temperature and the vapor pressure of the air, and γ is the psychrometric constant. Thus, ΔT_{eq}, representing differences between windward and leeward T_{eq} measured at a common height, will then reflect changes in the energy content of the flow due to shelter. If the field is dry so that $Q_{LE} \sim 0$, patterns of T_{eq} and T in the lee of a fence will be the same.

A convenient normalizing variable for ΔT_{eq} is $T_{eq}*$ defined as

$$T_{eq_*} = \frac{-(Q_H + Q_{LE})}{\rho c_p u_*} \tag{1.4}$$

Following similarity arguments presented for $\frac{\Delta \overline{u}}{\overline{u}_o}$, one expects $\frac{\Delta \overline{T}_{eq}}{T_{eq^*}}$ to depend on the same parameters. McNaughton (1985), in an unpublished experiment using straight 50% porous fences in near-neutral flow, reported a zone of warming in T_{eq} up to $\frac{x}{H} = 8$ and cooling in T_{eq} beyond, the latter corresponding to Raine and Stevenson's turbulent zone. The maximum $\frac{\Delta \overline{T}_{eq}}{T_{eq^*}}$ was measured at $\frac{x}{H} = 4$ where the windspeed was a minimum. No other experiments of similar nature appear in the literature.

The present study investigates the dependence of $\frac{\Delta \overline{u}}{\overline{u}_o}$ and $\frac{\Delta \overline{T}_{eq}}{T_{eq^*}}$ on various di-

mensionless parameters governing the flow in a square fenced plot. The parameters include $\frac{x}{H}$, $\frac{z}{H}$, $\frac{H}{z_o}$, $\frac{H}{L}$, $\frac{D}{H}$, and β, where $\frac{D}{H}$ is the fence sidelength to height ratio (sometimes refered to as the aspect ratio) and β is the wind direction.

The rationale for using a square plot is a response to the need to better understand airflow and microclimate changes in square sheltered plots which are a typical field practice especially for valuable horticultural crops. With this configuration, it is expected that the small aspect ratio ($\frac{D}{H}$) and the confining wall of the fenced plot will cause strong lateral flows, a feature shown to be very complex by Mulhearn and Bradley (1977). In their wind tunnel flow-visualization study using an oil paint technique, these authors concluded that fluid mechanics still has a long way to go before it can describe the effectiveness of shelterbelts in reducing evaporation, wind damage to crops, and soil erosion, because in practice the flows behind windbreaks are never two-dimensional. The present work aims to contribute to a better description of this three-dimensional problem. Results using a square-plot layout will be useful eventually in problems concerning fence design for an isolated small farmer's plot, or with the modern-day practice of network sheltering, for the more complicated case of multiple windbreaks.

The subject matter is developed in seven chapters. Chapter II reviews the characteristics of an undisturbed surface layer flow. Understanding this type of flow is very important inasmuch as description of any type of disturbed flow is always expressed as a departure from this reference state. An example of disturbed flow (IBL flow) is introduced in Chapter III, but the main emphasis is given to aerodynamics and microclimate modification of a windbreak analyzed with similarity

arguments. Transport of momentum is discussed first, followed by that of heat and mass analyzed in terms of equivalent temperature. Chapters IV to VI cover the field experiment at Ellerslie, Alberta; the method used in analyzing the data; and the discussion of results. Finally, Chapter VII gives a summary of the results and suggests areas for further study.

CHAPTER II

UNDISTURBED SURFACE LAYER FLOW

2.1 Introduction

The flow near the ground is almost always turbulent to a height of 1 km or more in daytime over land, to 100 m or so over land at night and to a few hundred meters over ocean. This mixed layer is the planetary boundary layer (PBL). The turbulence carries the fluxes of momentum, heat and mass which are of basic interest in such fields as agricultural and forest meteorology, pollution dispersal or building aerodynamics.

The two main approaches to the study of turbulent motions are to consider its dynamics as controlled by the equations of fluid flow and to study its properties as observed from measurements. The basic features of turbulence are not yet explained theoretically primarily because turbulence is a strongly non-linear phenomenon. It is strongly rotational and apparently chaotic. It is for this reason that for practical purposes, predictions about turbulent behavior are usually obtained by using the equations of fluid motion with certain simplifications derived from empirical data.

This chapter concentrates on the atmospheric surface layer (ASL), usually envisaged as the lowest fifty meters or so of the PBL. In this layer, the vertical gradients

of mean temperature, humidity and windspeed are large and the corresponding fluxes are approximately height independent. Under conditions of steady-state and horizontal homogeneity, the empirical flux-profile relations in the ASL are considered more or less established. In the study of the less-understood disturbed surface layer flow, the case of the undisturbed surface layer flow is used as the frame of reference. The effects of any obstruction to this flow are then translated in terms of the deviations from this reference state.

2.2 Governing Equations

The time-averaged conservation equations for momentum, heat and vapor for the ASL under the Boussinesq approximation are (Busch, 1973; Businger, 1982)

$$\frac{\partial \overline{u}_i}{\partial t} + \frac{\partial}{\partial x_j}(\overline{u}_i\overline{u}_j + \overline{u_i'u_j'}) = -\frac{1}{\rho_o}\frac{\partial \overline{p}}{\partial x_i} + g\frac{\overline{T}}{T_o}\delta_{3i} + \nu\nabla^2\overline{u}_i \tag{2.1}$$

$$\frac{\partial u_i}{\partial x_i} = 0 \tag{2.2}$$

$$\rho c_p\frac{\partial \overline{T}}{\partial t} = -\frac{\partial}{\partial x_j}(\rho_o c_p \overline{u}_j\overline{T} + \overline{u_j'T'}) + S_H \tag{2.3}$$

$$\frac{\partial \rho_v}{\partial t} = -\frac{\partial}{\partial x_j}(\overline{u}_j\overline{\rho_v} + \overline{u_j'\rho_v'}) + S_v \tag{2.4}$$

Here

(a) $\overline{p}$ is the time-averaged departure from a hydrostatic reference state $P_o(z)$ with

$$\frac{\partial P_o}{\partial z} = -g\rho_o$$

(b) $\overline{T}$ is the time-averaged departure from an adiabatic reference state $T_o(z)$ with

$$\frac{\partial T_o}{\partial z} = -\gamma_d$$

(c) The Coriolis acceleration $2\vec{\Omega} \times \vec{u}$ is small compared to the pressure and buoyancy terms and the turbulent diffusion term on the left-hand side of equation (2.1) and thus omitted.

(d) S_H contains source terms such as viscous dissipation of turbulent kinetic energy, radiative flux divergence $\frac{1}{\rho c_p}\frac{\partial Rn_i}{\partial z_i}$, conductive flux divergence $\kappa\frac{\partial^2 \overline{T}}{\partial z_i^2}$ and condensation/evaporation. Henceforth, assume $S_H = 0$.

(e) S_v contains source terms due to diffusive flux divergence $D\frac{\partial^2 \rho_v}{\partial z_i^2}$ and condensation/evaporation. Assume $S_v = 0$.

All instantaneous variables, $q(t)$, in the above equations have been decomposed into a mean $\overline{q}$ and fluctuation q' such that

$$q(t) = \overline{q} + q'$$

The Reynolds averaging scheme applies, some key features of which are:

- $\overline{q'} = 0$ for any $q(t)$
- $\overline{\overline{q}p'} = 0$ for any $q(t)$, $p(t)$
- $\overline{\overline{q}} = \overline{q}$
- $\overline{q(t)p(t)} = \overline{q}\overline{p} + \overline{q'p'}$
- $\overline{aq(t)} = a\overline{q}$ if a is a constant.

The terms $\overline{u_i'u_j'}$, $\overline{u_i'T'}$, $\overline{u_i'\rho_v'}$ which are due to the fluctuating part of the flow field can be interpreted as turbulent additions to, respectively, the viscous stress, heat flux and vapor flux. The first is known as Reynolds' stress, the last two as the turbulent heat and vapor flux densities.

Assuming

(i) steady state so that $\frac{\partial}{\partial t}$ (for any mean variable) = 0;

(ii) horizontal homogeneity so that $\frac{\partial}{\partial x} = \frac{\partial}{\partial y} = 0$ for any mean variable;

(iii) molecular transport negligible relative to convective transport; and

(iv) choosing axes such that $\overline{v} = 0$

the continuity equation (2.2) becomes especially simple

$$\frac{\partial \overline{w}}{\partial z} = 0$$

$$\overline{w} = 0$$

Similarly, the equations for the averaged quantities (2.1, 2.3, 2.4) when written in component form reduce to

u-momentum

$$\frac{\partial \overline{u'w'}}{\partial z} = -\frac{1}{\rho_o}\frac{\partial \overline{p}}{\partial x} \tag{2.5}$$

v-momentum

$$\frac{\partial \overline{v'w'}}{\partial z} = -\frac{1}{\rho_o}\frac{\partial \overline{p}}{\partial y} \tag{2.6}$$

w-momentum

$$\frac{\partial \overline{w'^2}}{\partial z} = -\frac{1}{\rho_o}\frac{\partial \overline{p}}{\partial z} + g\frac{\overline{T}}{T_o} \tag{2.7}$$

heat

$$0 = -\frac{\partial}{\partial z}\rho c_p \overline{w'T'} \tag{2.8}$$

vapor

$$0 = -\frac{\partial}{\partial z}\overline{w'\rho_v'} \tag{2.9}$$

In equation (2.7), $\frac{\partial \overline{w'^2}}{\partial z}$ is much smaller than the terms on the right (provided we are above any vegetation) and may be considered negligible. Note that in reality the

small rates of change of $\bar{T}$, $\bar{\rho}_v$ constantly occuring are the result of small (practically immeasurable) vertical gradients in the corresponding vertical fluxes, so that equations (2.8) and (2.9) are not strictly correct, but convenient approximations.

2.3 Constant Flux Layer

Had the Coriolis force been included in the derivation, it would have been seen that the Reynolds' stress $\overline{u'w'}$ changes with height at its *greatest* rate near $z = 0$. Nevertheless, it is normal practice to consider the shear stress (in addition to the heat and vapor fluxes) as constant over the depth of the ASL, by which is meant that the change over the ASL is a small fraction (say, $< 10\%$) of the surface value. Likewise, though in reality trends in the temperature and humidity imply height changes in Q_H and Q_{LE}, it is a useful approximation to consider Q_H, Q_{LE} constant within the ASL; measurement of their changes with height over small intervals of height is in any case beyond present instrumental capabilities. Therefore, we define these fluxes to be height-independent in the ASL

momentum flux

$$\tau = -\rho_o \overline{u'w'} \tag{2.10}$$

sensible heat flux

$$Q_H = \rho_o c_p \overline{w'T'} \tag{2.11}$$

latent heat flux

$$Q_{LE} = L_v \overline{\rho_v' w'} \tag{2.12}$$

2.4 The Closure Problem

The averaging process imposed on the momentum, heat and mass conservation equations from which the equations of the mean flow (equations 2.1, 2.3 and 2.4) are derived introduces new unknowns in the form of the stress-gradient terms. These terms play a major role in turbulent transport in the ASL as equations (2.5-2.9) indicate. In order to close this set of equations at first order, expressions relating the covariances $\overline{u'w'}$, $\overline{w'T'}$ and $\overline{w'\rho_v'}$ to the mean flow have to be formed.

2.4.1 First-Order Closure

The simplest scheme which has been used with considerable success in the ASL is to model turbulent transfer after its molecular counterpart. Boussinesq in 1877 was first to apply this to the momentum flux by introducing an eddy viscosity K_m so that

$$\overline{u'w'} = -K_m \frac{\partial \bar{u}}{\partial z} \tag{2.13}$$

This may be generalized for any quantity whose concentration is c using an eddy diffusivity K_c

$$\overline{w'c'} = -K_c \frac{\partial \bar{c}}{\partial z} \tag{2.14}$$

The most general linear relation between a vector flux density and a driving gradient is

$$F_j = -K_{ij} \frac{\partial \bar{c}}{\partial x_i} \tag{2.15}$$

where K_{ij} is now a tensor diffusivity permitting *cross* fluxes. In the ASL, it suffices to limit these expressions to vertical exchange and scalar K's so that we have

equation (2.13) and the equivalent forms for heat and mass transfer

$$\overline{w'T'} = -K_H \frac{\partial \overline{T}}{\partial z} \tag{2.16}$$

$$\overline{w'\rho_v'} = -K_v \frac{\partial \bar{\rho}_v}{\partial z} \tag{2.17}$$

The K's however, unlike their molecular counterparts ν and D, are not constant fluid properties depending only on temperature and pressure. They have to absorb the complexities of turbulence. To relate them to the mean characteristics of the flow, Prandtl in 1932 introduced the mixing length concept in analogy to the molecular mean free path. In effect, it was recognized that

$$K \sim ql \tag{2.18}$$

where q and l are velocity and length scales of the energy-containing eddies. Since both q and l vary with height, it follows that K is also height (as well as stability) dependent. An array of suggested theoretical and empirical K-profiles exists in the literature (Wyngaard, 1984) reflecting the difficulty of determining K analytically, the lack of data in prescribing K empirically, and the inherent variability of K itself in response to the wide variety of possible states of the PBL. From the now extensive surface layer measurements, the K 's can be related to the universal functions Φ_M, Φ_H and Φ_W which will later be discussed. However, some objections to the K-theory remain, particularly in cases in which the property being transported has sources or sinks in the mixing region (i.e., an elevated source) or when the turbulent length scale exceeds the scale upon which there are changes in the property concentration gradient (i.e., heat transport within a crop). K-theory becomes progressively less

reliable as one approaches a rough vegetated surface and fails entirely within the canopy, where negative K's are sometimes observed (Raupach and Legg, 1984).

There are also problems in applying K-theory for turbulent transport far from the ground. This is partly attributed to the lack of good data, but mostly to the turbulence structure aloft which is influenced by many processes such as horizontal inhomegeneity, baroclinicity, entrainment through a capping inversion, gravity waves, etc., all probably affecting distributions of the effective diffusivity/viscosity.

Two important features of turbulent transfer are inferred from equation (2.18)

1. For a typical boundary layer ($q \sim 1$ m/s, $l \sim 300$ m), $\frac{K_M}{\nu} \sim 10^7$ showing the dominance of turbulent transport over molecular processes.

2. K is a property of the flow, not a property of the fluid.

The problem of specifying this dependence remains the major weaknesses of the K-theory (Businger, 1982).

2.4.2 Second-order Closure

The limitations of K-theory may in some but not all circumstances be resolved by higher-order closures. The procedure is to derive variance and covariance equations from the basic conservation equations of motion, heat and mass. This is quite straightforward, as shown by Businger (1982). The main difficulty, however, is again closure since each equation introduces new unknowns in terms of triple correlations, pressure-velocity correlations, etc. With certain assumptions on these higher-order terms, and of course the considerable computation time involved, this procedure appears to be part and parcel of most of the recent PBL models. Modelling, however,

is beyond the scope of this work and the interested reader is referred to Donaldson (1973) and Wyngaard (1982).

2.5 The Logarithmic Wind Profile

For a neutrally stratified atmosphere, the variation of $\bar{u}$ with height is described by the classical logarithmic wind profile. Defining a scaling velocity u_*, equation (2.10) may be written as

$$\tau = -\rho_o \overline{u'w'} = u_*^2 \tag{2.19}$$

Similarly, K_m from the mixing length hypothesis may be defined as

$$K_m = k u_* z \tag{2.20}$$

where k is the von Karman's constant. Substituting the above into equation (2.13) gives

$$\frac{\partial \bar{u}}{\partial z} = \frac{u_*}{kz} \tag{2.21}$$

which upon integration from $z = z_o$ (defined to be the height where $\bar{u} = 0$ according to the analysis) to height z yields

$$\bar{u}(z) = \frac{u_*}{k} \ln \frac{z}{z_o} \tag{2.22}$$

The von Karman's constant has been variously estimated over the last two decades to have numerical values ranging between 0.33 and 0.41. Recently, the value of 0.40 is in favor as result of investigations by Wieringa (1980), Dyer and Bradley (1982), and Högstrom (1985). The friction velocity u_* represents the shear stress at the surface caused by the wind field.

When extended to plant communities, equation (2.22) is usually written in the form of a *displaced* log profile

$$\overline{u}(z) = \frac{u_*}{k} \ln \frac{z-d}{z_o} \tag{2.23}$$

where d, the displacement height, is a major fraction of the plant height h. In effect, d indicates the mean level at which momentum is absorbed by the plants (Thom, 1975).

It should be noted that equations (2.21 - 2.23) are valid only for $z \gg z_o$; i.e., one does not expect the wind profile within or close above the canopy to be logarithmic. The parameter z_o, known as the roughness length, enters the log profile equation as a surface boundary condition. It stands for the height where the log profile, when extrapolated to the surface, vanishes. The graphical method of determining z_o is discussed in Chapter V.

2.6 Monin-Obukhov Similarity

The ASL is very seldom neutral. The diurnal changes in solar radiation set up a cycle of cooling and heating of the layer which influences the turbulence and therefore the variations of the mean variables. Even the short period in the early morning and early evening which represent the transition from lapse to stable stratification (and vice versa) cannot be strictly considered neutral if one is to conform to the definition of zero heat flux or zero potential temperature vertical gradient. The more general situation with a heat flux present is the *diabatic* case.

Two factors that play important roles in the diabatic case are the mechanical (shear) and buoyancy forces. This is shown explicitly in the turbulent kinetic energy

(TKE) balance, which for the special case of horizontal homogeneity can be written as

$$\frac{\partial \bar{e}}{\partial t} = -\overline{u'w'}\frac{\partial \bar{u}}{\partial z} + \frac{g}{T}\overline{w'T'} - \frac{\partial}{\partial z}\left(\frac{\overline{w'p'}}{\rho} + \overline{w'e'}\right) - \varepsilon \qquad (2.24)$$

S B P T

where

$\bar{e} = \frac{1}{2}(\bar{u'}^2 + \bar{v'}^2 + \bar{w'}^2)$

S= mechanical (shear) production term

B= buoyant production term

P= pressure transport term

T= turbulent transport term

ε= viscous dissipation term

Since the production terms are driving the turbulence, Richardson (1920) devised a stability parameter by taking the ratio of these two terms. This is the flux Richardson number

$$Ri_f = \frac{g}{T}\frac{\overline{w'T'}}{\overline{u'w'}\frac{\partial \bar{u}}{\partial z}} \qquad (2.25)$$

The drawback of Ri_f as a stability parameter is that it contains a mixture of covariances and mean profile information which is usually difficult to determine in practice. Using equations (2.13) and (2.16), a simpler expression containing only mean quantities can be derived. This is the gradient Richardson number

$$Ri_g = \frac{g}{T}\frac{\partial \overline{T}/\partial z}{(\partial \bar{u}/\partial z)^2} = \frac{K_M}{K_H}Ri_f \qquad (2.26)$$

When $Ri_g = 0$, the heat flux is zero and the atmosphere is neutral ; when $Ri_g > 0$, the atmosphere is statically stable; when $Ri_g < 0$, unstable.

One disadvantage of Ri_g is that it is a function of height. As such, it cannot be easily represented in simple scaling parameters such as a scaling velocity, length or time. For this reason, meteorologists tend to replace Ri_g by the dimensionless ratio z/L where L is the Monin-Obukhov length.

Very near the surface, mechanical forces dominate, but since the wind shear decreases with height much more rapidly than the buoyancy term, there is usually a height above which buoyancy becomes dominant. Monin and Obukhov (1954) used this height as a scaling length and from similarity arguments estimated the length L.

The outline of reasoning behind the Monin-Obukhov scaling is as follows (Calder, 1966; Wilson, 1985a). Complete similarity between systems A and B is said to obtain if the governing equations (and boundary and initial conditions) expressed in non-dimensional form by use of scale factors can be made identical. Consider the Navier-Stokes equation under the Boussinesq approximation

$$\frac{\partial u_i}{\partial t} + u_j \frac{\partial u_i}{\partial x_j} = -\frac{1}{\rho_o}\frac{\partial p}{\partial x_i} + g\frac{\overline{T}}{T_o}\delta_{3i} \tag{2.27}$$

where the viscous and Coriolis terms are neglected in the surface layer for the purpose at hand. Next, non-dimensional variables are defined such that

$$u_j^D = \frac{u_j}{V}$$

$$x_j^D = \frac{x_j}{L}$$

$$T^D = \frac{\overline{T}}{\overline{T}_.}$$

$$p^D = \frac{p}{P}$$

where V, L, T_* and P are velocity, length, time and pressure scales.

Substituting in equation (2.27) and rearranging gives

$$\frac{\partial u_i^D}{\partial t^D} + u_j^D \frac{\partial u_i^D}{\partial x_j^D} = (-\frac{P}{\rho_o V^2}) \frac{\partial p^D}{\partial x_i^D} + (\frac{g T_* L}{T_o V^2}) T^D \delta_{3i}$$

where $t^D = t/(L/V)$. This non-dimensional equation contains two dimensionless ratios. If these ratios can be kept constant regardless of the nature of the flow, then a universal solution of u_i^D is found.

In the special case of the constant flux layer for which

$$\overline{w'T'} = \frac{Q_H}{\rho c_p} = constant$$

$$-\overline{u'w'} = u_*^2$$

the following choice of scales is justified

$$\begin{aligned} T_* &= -\frac{\overline{w'T'}}{u_{*_o}} = -\frac{Q_H}{\rho c_p u_*} \\ V &= u_{*_o} \\ P &= \rho_o u_{*_o}^2 \end{aligned} \tag{2.28}$$

This reduces the dimensionless ratios to

$$1, \quad \frac{g}{T_o} \frac{L}{u_{*_o}^2} \frac{1}{u_{*_o}} \frac{Q_H}{\rho c_p}$$

Thus, the external parameters governing surface layer flow are g/T_o , u_*, $Q_H/\rho c_p$ and z. Strictly, the molecular diffusivities ν, κ, and D should also be included for a complete solution but in the ASL where the flow is completely turbulent, these terms are justifiably ignored. Also, a scaling length to represent the surface roughness, z_o, is not included. Therefore, the similarity formulation is restricted to $z/z_o \gg 1$,

which, to be recalled, is the boundary condition imposed on the log profile (2.23). Hence, the breakdown of the similarity theory in canopy flow.

Now define L such that

$$L = -\frac{u_{*_o}^3}{k\frac{g}{T_o}\frac{Q_H}{\rho c_p}} \tag{2.29}$$

The ratios are by this choice always unity, independent of such turbulence parameters as as u_{*_o}, $\frac{g}{T_o}$ and $\frac{Q_H}{\rho c_p}$. Here, k, the von Karman's constant, is added solely as a matter of convenience. This leaves the two length scales z and L as the governing parameters from which a non-dimensional ratio

$$\xi = \frac{z}{L}$$

may be defined.

The non-dimensional wind shear may now be written as

$$\frac{kz}{u_*}\frac{\partial \overline{u}}{\partial z} = \Phi_M(\xi) \tag{2.30}$$

Similarly

$$\frac{kz}{T_*}\frac{\partial \overline{T}}{\partial z} = \Phi_H(\xi) \tag{2.31}$$

where Φ_M and Φ_H are universal functions of ξ, and T_* as in equation (2.28). These are now valid for all stability conditions.

In summary, the ASL profile equations can be written in their more conventional form

$$\frac{\partial \overline{u}}{\partial z} = \frac{u_*}{kz}\Phi_M(\xi) \tag{2.32}$$

$$\frac{\partial \overline{T}}{\partial z} = \frac{T_*}{kz}\Phi_H(\xi) \tag{2.33}$$

$$\frac{\partial \bar{\rho}_v}{\partial z} = \frac{\rho_{v*}}{kz}\Phi_W(\xi) \tag{2.34}$$

where $\rho_{v*} = -Q_{LE}/\rho c_p L_v u_*$.

In equation (2.29), the minus sign is added in order for L to have the same sign as Ri_g, the gradient Richardson number. Stratification is neutral ($Q_H = 0$) for $L = \pm\infty$, unstable ($Q_H > 0$) for $-\infty < L < 0$ and stable ($Q_H < 0$) for $0 < L < \infty$. Table 2.1 summarizes the general properties of ξ and Ri_g.

2.7 Estimation of Φ for Diabatic Profiles

The shapes of Φ_M, Φ_H and Φ_W cannot be determined from similarity theory but must come from careful experimentation. The literature of the past twenty years is liberally scattered with suggestions regarding empirical formulations of these Φ functions. The more recent and important ones are reviewed by Busch (1973), Dyer (1974) and Yaglom (1977). Some of the differences in the formulations arise from the disagreement on the value of the von Karman's constant k to be used. The present work will adopt Dyer and Bradley's (1982) Φ functions obtained from the 1976 International Turbulence Comparison Experiment. These authors concluded from their analysis that within the statistical limitations of the data, k=0.4 and for unstable stratification

$$\Phi_M = (1 - 28\frac{z}{L})^{-\frac{1}{4}} \tag{2.35}$$

$$\Phi_H = (1 - 14\frac{z}{L})^{-\frac{1}{2}} \tag{2.36}$$

$$\Phi_W = \Phi_H \tag{2.37}$$

For stable stratification, Webb's (1970) log linear form will be used

$$\Phi_M = \Phi_H = \Phi_W = 1 + 5.2(\frac{z}{L}) \tag{2.38}$$

Table 2.1. Qualitative Interpretation of $\xi = \frac{z}{L}$ and Ri_g

$\xi = \frac{z}{L}$, Ri_g	Description
Strongly negative	When the shear production is zero or negligibly small and the buoyancy term is positive, the turbulent convection is known as free convection.
Negative but small	Mechanical turbulence dominates over the buoyancy term.
Zero	When the buoyancy term is zero or negligible and the shear production term is the only input to turbulent energy, the condition of pure mechanical turbulence is known as forced convection.
Slightly positive	Mechanical turbulence is slightly damped by temperature stratification.
Strongly positive	When the bouyancy term is negative and becomes more important than shear production, a transition from turbulent to laminar flow may take place. The transition occurs at a critical value of Ri_g, believed to be about $Ri_c \sim 0.25$.

Figures 2.1 and 2.2 present Φ_M and Φ_H as a function of $\frac{z}{L}$ according to equations (2.35-2.38) compared to that of Dyer and Hicks (1970) who used k=0.41 and suggested for unstable stratification

$$\Phi_M = (1 - 16\frac{z}{L})^{-\frac{1}{4}} \tag{2.39}$$

$$\Phi_H = (1 - 16\frac{z}{L})^{-\frac{1}{2}} \tag{2.40}$$

Without commitment to the exact form of Φ, the profile equations were integrated by Paulson (1970) to give the following more explicit profiles

A. Wind

$$\overline{u} = \frac{u_*}{k}(\ln \frac{z}{z_o} - \psi_M) \tag{2.41}$$

where (i) for $\frac{z}{L} < 0$

$$\psi_M = 2\ln[\frac{1}{2}(1+x)] + \ln[\frac{1}{2}(1+x^2)] - 2\arctan x + \frac{\pi}{2}$$

$$x = \Phi_M^{-1}$$

(ii) for $\frac{z}{L} > 0$

$$\psi_M = -5\frac{z}{L}$$

B. Temperature

$$\overline{T} - T_o = \frac{T_*}{k}(\ln \frac{z}{z_o} - \psi_H) \tag{2.42}$$

where (i) for $\frac{z}{L} < 0$

$$\psi_H = 2\ln[\frac{1}{2}(1+x)]$$

$$x = \Phi_H^{-1}$$

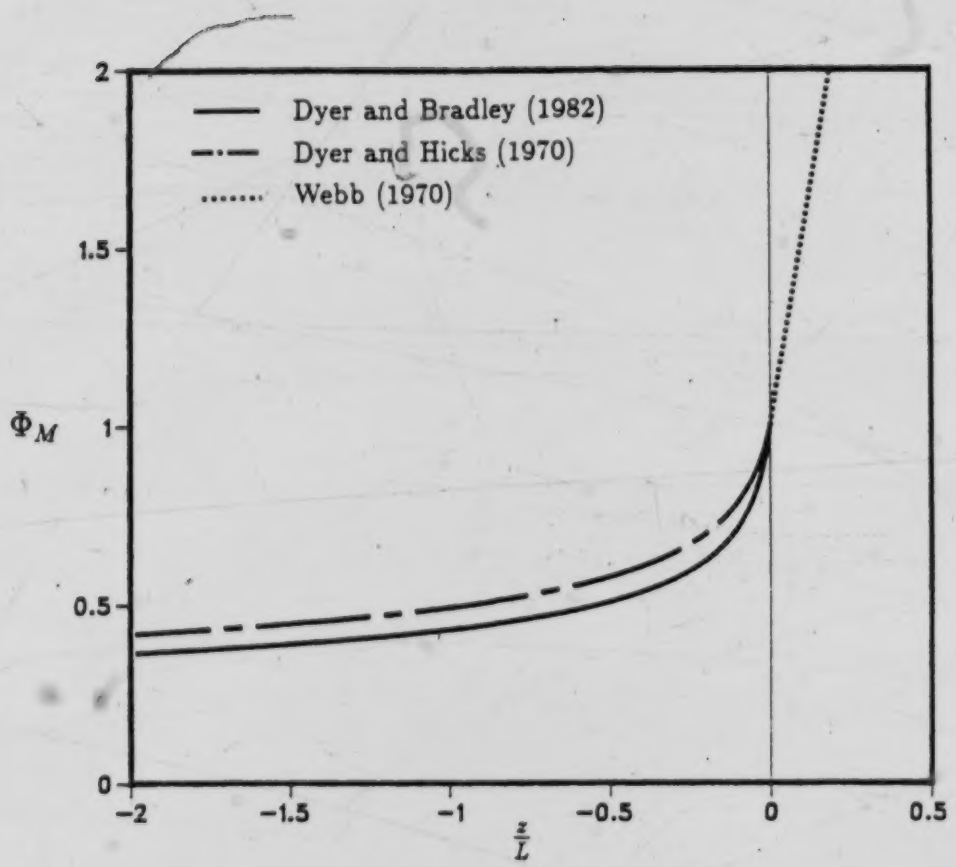

Figure 2.1 Plot of Φ_M as a function of $\frac{z}{L}$.

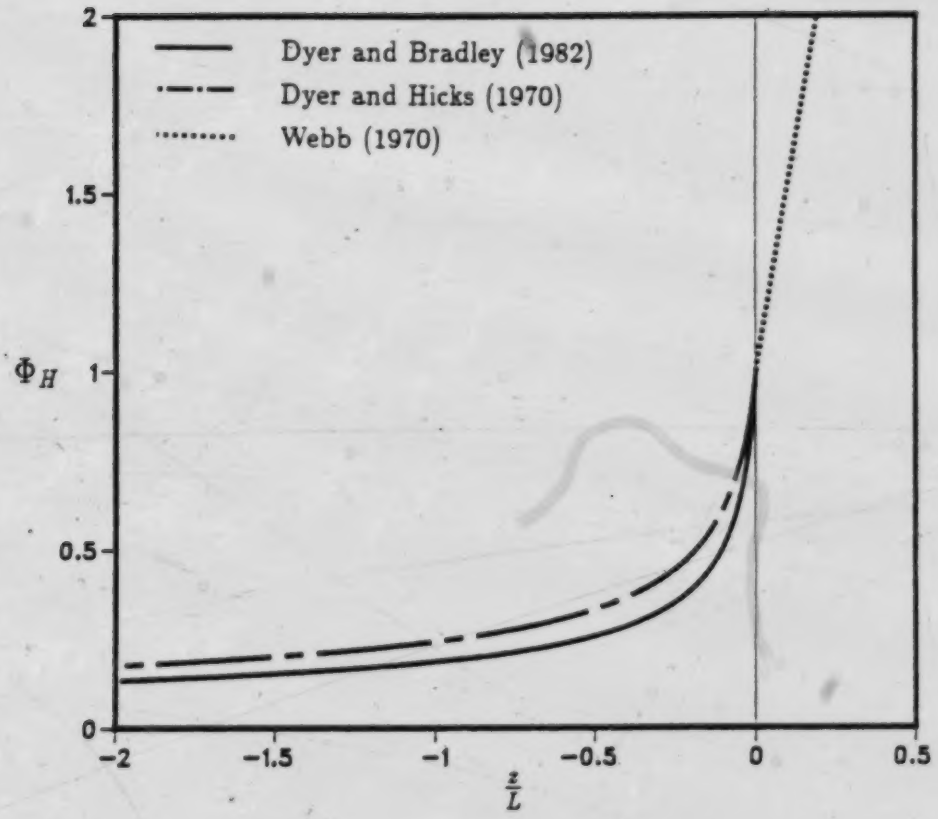

Figure 2.2 Plot of Φ_H as a function of $\frac{z}{L}$.

(ii) for $\frac{z}{L} > 0$

$$\psi_H = -5\frac{z}{L}$$

From the foregoing equations (which do not depend on the adoption of the K-theory) effective diffusivities may be defined

$$K_M = \frac{ku_*z}{\Phi_M} \tag{2.43}$$

$$K_H = \frac{ku_*z}{\Phi_H} \tag{2.44}$$

$$K_W = \frac{ku_*z}{\Phi_W} \tag{2.45}$$

The exchange coefficient ratio, α, may be written as

$$\alpha = \frac{K_H}{K_M} = \frac{\Phi_M}{\Phi_H} \tag{2.46}$$

Also, the gradient Richardson number Ri_g takes the form

$$Ri_g = \frac{g}{T_o}\frac{\frac{\partial \overline{T}}{\partial z}}{(\frac{\partial \overline{u}}{\partial z})^2} = \xi\frac{\Phi_H}{\Phi_M^2} \tag{2.47}$$

Since Φ_M and Φ_H are functions of ξ only, Ri_g and α are also functions of ξ only. For unstable conditions, we may write $Ri_g = \xi$. This follows exactly from (2.39, 2.40) and is a good approximation for (2.35, 2.36).

CHAPTER III

WINDBREAK FLOW

3.1 Introduction

The one-dimensional profile laws described in the preceding chapter apply only for an extensive, flat, horizontally homogeneous surface to which natural terrain corresponds only in exceptional cases. In many examples of practical importance, there are obstructions, man-made or otherwise, which disturb the flow from its equilibrium state. For instance, in land-lake interface problems and in flows over finite areas of irrigated land, abrupt changes in surface conditions such as roughness, temperature and humidity occur simultaneously. For the simplest case of the wind blowing perpendicular to the discontinuity, the resulting flow structure now depends on the distance downstream of the discontinuity as well as the height above the surface. The treatment of these problems is thus permitted to be two-dimensional. The additional component is accounted for by the streamwise divergence of the horizontal transport of momentum, heat or mass (known as local advection).

3.1.1 Internal Boundary Layer (IBL) Flow

The IBL is the boundary layer that develops inside the PBL when the approach flow encounters a change in surface condition. The situation illustrated in Figure 3.1 and which was adapted from Plate (1971b) typifies a flow over a surface with a smooth to rough transition. Far upstream and at large heights downstream of the discontinuity, the flow is essentially not affected by the surface change (although it should be noted that in an incompressible flow, the pressure at any point depends on the velocity field everywhere; the sensitivity however decreases rapidly with distance, so that velocity changes near the ground should have little influence on pressure and hence velocity far aloft and far upstream). The region influenced by the downwind roughness can be identified by the curve $\delta_{IBL}(x)$ in the figure and is called the internal boundary layer of thickness δ_{IBL}. Above this is the outer region whose flow characteristics are the same as the approach flow, except for a slight displacement δ'. Within the IBL are two sublayers. Very close to the ground is the inner layer where the flow is governed by the roughness length z_{o2} and $u_{*2}(x)$ and is in equilibrium with the new surface in the sense that the shear stress at the outer edge of the inner layer is almost equal to the shear stress at z=0. Above this is the blending region in which the log profile from below gradually changes to that of the outer layer. The thickness δ_{IBL} is generally indicated to increase with fetch x as $\delta_{IBL} \sim x^n$ where $n = 0.8$ for a neutral atmosphere (Elliot, 1958) and increases to about $n = 1.4$ with increasing instability (Rao, 1975).

For micrometeorologists, interest in the IBL grew out of the necessity to explain results of field experiments which yielded flow characteristics significantly different

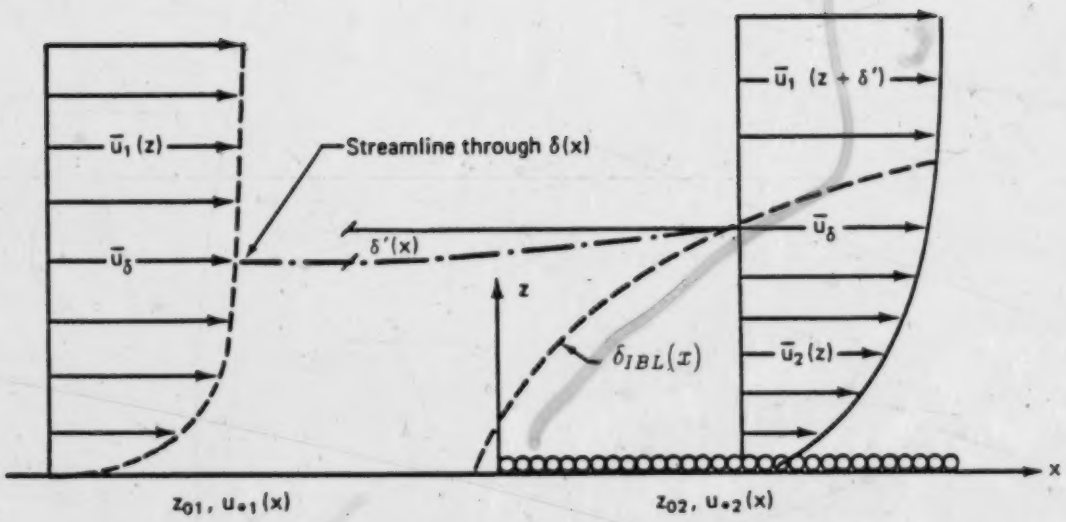

Figure 3.1 Schematic representation of the development of an internal boundary layer: flow from smooth to rough.

from those expected over truly uniform terrain. Plate (1971b) considers that the IBL is sufficiently understood to provide quantitative estimates of advective errors in micrometeorological experiments. The most direct application is the height-to-fetch ratio generally set at 1% in field experiments. This criterion ensures that the constant flux layer extends over the height of the measuring instruments (Bradley, 1968). Apart from this application, IBL studies are useful in the quantitative prediction of evaporation from small lakes and from irrigated fields in dry lands (Philip, 1959; Rao et al., 1974).

3.2 Windbreak Aerodynamics

3.2.1 Overview

The most important aspect of the shelter problem is the aerodynamic effect, since this has a major impact on the lee microclimate. The windbreak exerts a drag force on the wind, causing a net loss of momentum of the air. In an incompressible fluid, a reduction in mometum implies a reduction in velocity and thus the drag causes the wind reduction desired for sheltering. The greater the drag, the greater is the momentum loss from the flow. As the permeability of the windbreak is reduced, the *bleed* flow through the windbreak decreases and the drag force increases. Further decrease in permeability may result in intermittent reverse flow (large eddies) in the lee of the windbreak (refer to Figure 3.2). Perera (1981) found that separation flow occured only for porosities less than about 30%. For a solid barrier in a wind tunnel, Ogawa and Diosey (1980) estimated the reattachment point at $\frac{x}{H} = 7$ while Raine and Stevenson (1974) set it at $\frac{x}{H} = 8$. Windbreaks of fairly high porosities (30 %

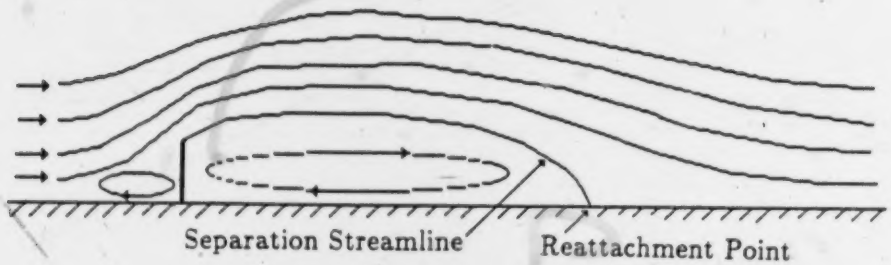

Solid Windbreak

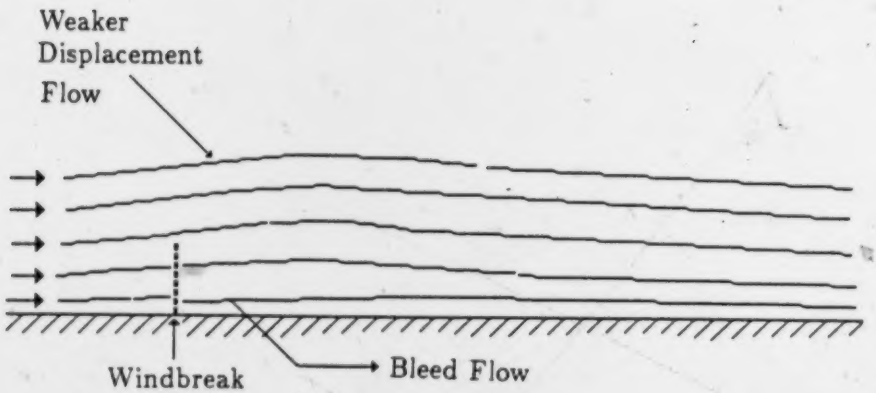

Porous Windbreak

Figure 3.2 Streamline sketches of windbreak flow.

to 50 %) are generally recommended to avoid the reverse flow which is associated with large-scale turbulence in the lee.

It is therefore important to distinguish between maximum reduction of the mean flow and optimal wind reduction, since maximum reduction of the mean flow may be accompanied by undesirably high turbulence. In the aerodynamic sense, optimal refers to a compromise between levels of wind reduction and turbulence to suit, for example, a certain agricultural need.

3.2.2 Governing Equations

For a neutrally-stratified incompressible flow disturbed by a two-dimensional obstruction, the streamwise (x) and cross-stream (z) momentum conservation equations under steady state are (Wilson, 1985b)

$$\frac{\partial}{\partial x}(\overline{u}\overline{u} + \overline{u'^2} + \frac{\overline{p}}{\rho}) + \frac{\partial}{\partial z}(\overline{u}\overline{w} + \overline{u'w'}) = SU \tag{3.1}$$

$$\frac{\partial}{\partial x}(\overline{u}\overline{w} + \overline{u'w'}) + \frac{\partial}{\partial z}(\overline{w}^2 + \overline{w'^2} + \frac{\overline{p}}{\rho}) = SW \tag{3.2}$$

The overbar denotes spatial average along the windbreak (i.e., crosswind). The source terms SU and SW contain such terms as form drag and skin friction derived from airflow-fence interaction. For a porous fence, the rate of extraction of momentum may be parameterized as

$$SU = -k_x \overline{u}|\overline{u}|\delta(x,0)s(z,H) \tag{3.3}$$

$$SW = 0 \tag{3.4}$$

where $\delta(x,0)$ is the delta function (zero unless $x = 0$) having dimensions [length^{-1}] and $s(z,H)$ is a dimensionless unit step function defined by ($s = 1$ for $z \leq H$;

$s = 0$ for $z > H$) where H is the fence height. The term k_r is the fence resistance coefficient defined with respect to a blockage flow in a wind tunnel, with the fence blocking the working section. The resistance coefficient is defined by

$$k_r = \frac{\Delta p}{\rho u_o^2} \tag{3.5}$$

where Δp is the pressure drop across the material and u_o is the flow velocity. This parameter is an aerodynamic property of the fence whereas porosity ϕ is a geometric property. Unfortunately, k_r values have not been reported in many shelter studies, so the less satisfactory ϕ is often used to characterize the windbreak.

For vegetative shelter, the momentum sink term may be written as

$$SU = -C_D(x,z)a(x,z)\overline{u}|\overline{u}| \tag{3.6}$$

$$SW = 0 \tag{3.7}$$

where $a(x,z)$ is the leaf area density [length^{-1}] and C_D is a local drag coefficient for the porous medium.

The budget equation for the turbulent stresses in the momentum conservation equation may be written as

$$\begin{aligned}\overline{u}_j\frac{\partial\overline{u_i'u_k'}}{\partial x_j} &= -\overline{u_k'u_j'}\frac{\partial\overline{u}_i}{\partial x_j} - \overline{u_i'u_j'}\frac{\partial\overline{u}_k}{\partial x_j} - \frac{\partial}{\partial x_j}\overline{u_i'u_k'u_j'} \\ &\quad - \frac{1}{\rho}\frac{\partial\overline{u_k'p'}}{\partial x_i} + \frac{1}{\rho}\frac{\partial\overline{u_i'p'}}{\partial x_k} + \overline{\frac{\rho'}{\rho}\left(\frac{\partial u_k'}{\partial x_i} + \frac{\partial u_i'}{\partial x_k}\right)} - 2\nu\overline{\frac{\partial u_i'}{\partial x_j}\frac{\partial u_k'}{\partial x_j}} + S_{ik}\end{aligned} \tag{3.8}$$

where S_{ik} contains the airflow-solid interaction terms.

By setting $i = k$, the TKE budget equation may be obtained

$$\begin{aligned}\frac{\partial}{\partial x}(\overline{ue}) + \frac{\partial}{\partial z}(\overline{we}) &= -\overline{u'^2}\frac{\partial\overline{u}}{\partial x} - \overline{w'^2}\frac{\partial\overline{w}}{\partial z} - \overline{u'w'}\left(\frac{\partial\overline{u}}{\partial z} + \frac{\partial\overline{w}}{\partial x}\right) \\ &\quad - \frac{\partial}{\partial x}\left(\overline{u'e} + \frac{1}{\rho}\overline{u'p'}\right) + \frac{\partial}{\partial z}\left(\overline{w'e} + \frac{1}{\rho}\overline{w'p'}\right) - \varepsilon + SE\end{aligned} \tag{3.9}$$

where $e = \frac{1}{2}\overline{u_k' u_k'}$ and $SE = \frac{1}{2}S_{ii}$ represents conversion of mean flow kinetic energy into TKE of the wake flow. On the left-hand side of the TKE budget are the advection terms. The first three terms on the right-hand side, the production terms, represent the rate at which the mean flow contributes to the TKE: normal stress for the first two terms and shear stress for the third. The fourth and fifth terms are the combined turbulent and pressure transport, and ε is the viscous dissipation term.

Numerical solutions to the momentum equations have met considerable success especially in simulating the air flow in the near-wake zone. Hagen et al.,(1981) imposed an extra boundary condition by specifying the velocity profile at the fence, while Wilson (1985b) included the above momentum sinks SU and SW and solved the momentum equations using various closure schemes.

3.2.3 Quiet and Turbulent Zones

The concept of Raine and Stevenson's (1977) turbulent and quiet zones as determined in a wind tunnel was introduced in Chapter I and is shown here as a schematic diagram in Figure 3.3. In the immediate lee of the fence, the quiet zone characterized by reduced turbulent velocity scale and smaller eddy sizes extends from the fence-top to the surface at about $\frac{x}{H} = 8$. Further leeward and overlying the quiet zone is a wedge-shaped zone of increased turbulence.

(1) Turbulent zone. The increased turbulence in the wake can be explained qualitatively by the following sequence of events. As the wind moves across the fence, the streamlines are compressed just above the fence top, causing a region

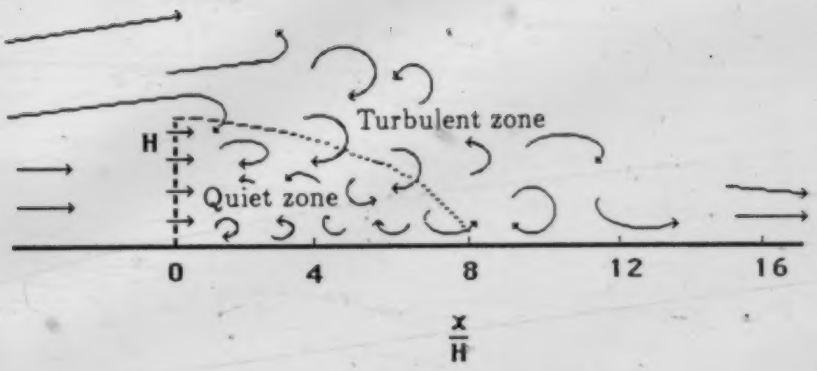

Figure 3.3 Schematic representation of turbulence in the quiet and turbulent zones behind a model windbreak.

of very strong wind shear and consequent shear production of turbulent kinetic energy. This zone widens and follows the streamlines as the air moves downwind. The results of Finnigan and Bradley (1983) shown here in Figures 3.4, 3.5 and 3.6 are some of the best available to illustrate these features quantitatively. These authors analyzed the TKE budget equation behind a porous fence in atmospheric flow using streamline coordinates. The enhanced vertical scale of Figures 3.4 and 3.6 masks the fact that the distortion of the streamline patterns is small, less than 6% even in the immediate fence vicinity. This means that the interpretation of the figures if referenced to the TKE budget (equation 3.9) in Cartesian coordinates will not be at great variance with each other. From the TKE budget, the increased shear (Figures 3.4 and 3.5) and the increased Reynolds' stresses (Figure 3.6), whose maxima occur in the same region ($\frac{z}{H} \approx 1$), result in strong production of turbulent energy. The strong mixing resulting from this turbulence leads to a large downward momentum transport in the wake causing re-acceleration.

In the field, this advection of turbulence in the wake flow, generated by the strong shear zone caused by the windbreak itself, was reportedly responsible for the observed pattern of kiwifruit damage in a New Zealand orchard sheltered by a network of natural and artificial windbreaks (McAneney and Judd, 1987). The damage was due to windrub which increases in proportion to the strength of the turbulent eddies.

(2) Quiet zone. Turbulence measurements in the lee of solid (Ogawa and Diosey, 1980; Jacobs, 1985) and porous (Hagen and Skidmore, 1971; Raine and Stevenson, 1977; Wilson, 1987) fences showed a zone of reduced velocity variance from the

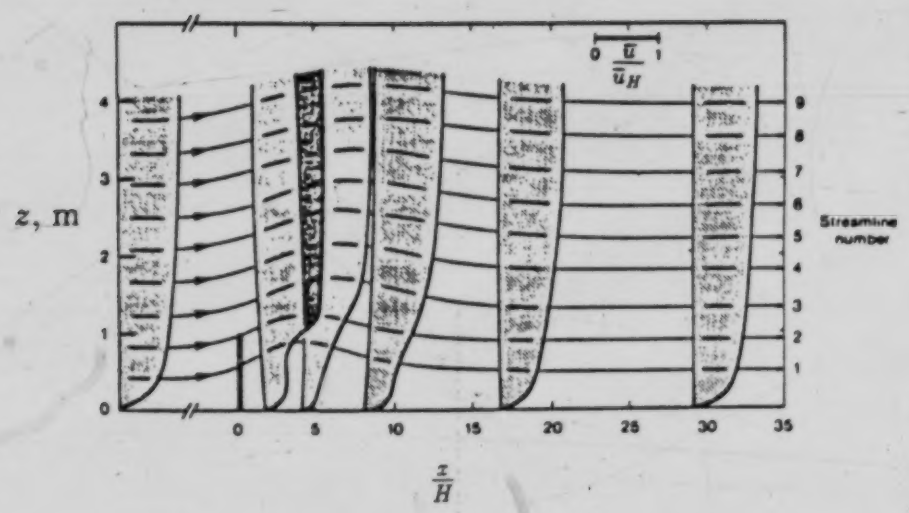

Figure 3.4 Profile of $\frac{\bar{u}}{\bar{u}_H}$ referred to streamline coordinate axes. $\bar{u}_H$ is the horizontal wind velocity at fence height H.

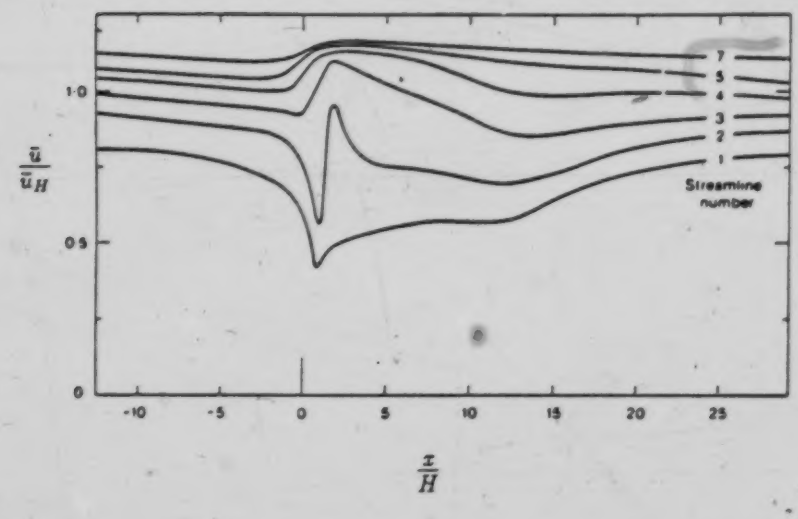

Figure 3.5 Variations of $\frac{\bar{u}}{\bar{u}_H}$ along streamlines.

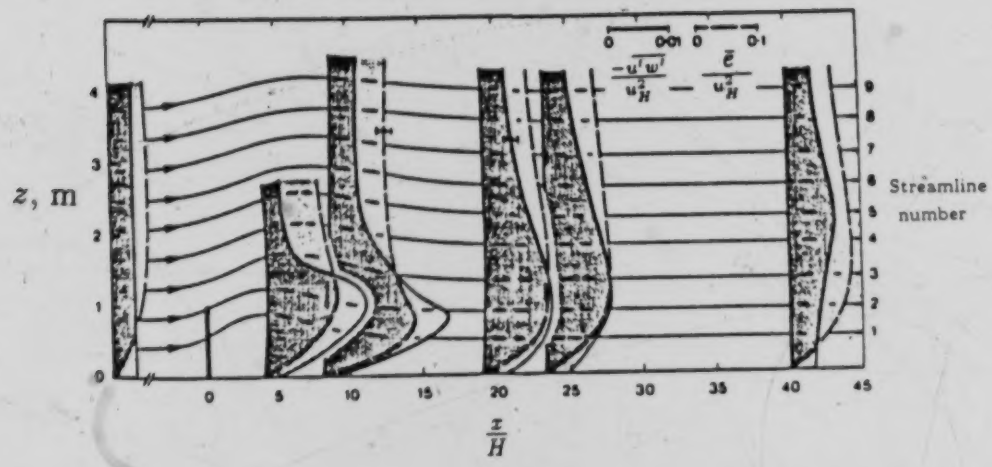

Figure 3.6 Profiles of $-\overline{u'w'}/u_H^2$ and $\bar{e}/u_H^2$ (Finnigan and Bradley, 1983).

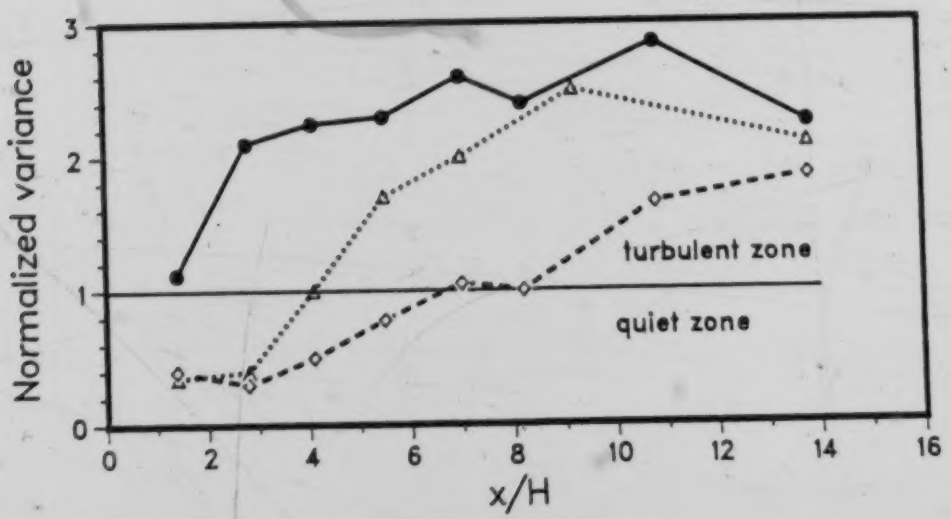

Figure 3.7 Horizontal profiles of the normalized variance of v, w ($\diamond, \triangle$) at $\frac{z}{H} = 0.5$ and of w ($\bullet$) at $\frac{z}{H} = 1$ (Wilson, 1987).

fence-top to the ground. The extent of reduction of variance and the rate of return to upstream values (a measure of the horizontal extent of the quiet zone) were found to depend on fence porosity and to some extent on atmospheric stability. Horizontal profiles of the variance ratios $\overline{w'^2}(z)/\overline{w'^2_o}(z)$ and $\overline{v'^2}/\overline{v'^2_o}(z)$ at two measurement heights $\frac{z}{H} = 1.0, 0.5$ under near-neutral stratification with $\phi = 0.5$, $\frac{H}{z_o} = 75$, $\frac{D}{H} = 45$ are shown in Figure 3.7. These results, obtained from an experiment at Ellerslie, Alberta (Wilson, 1987), correspond to a fence of spatially-uniform porosity. The quiet zone is evident in the v and w components at $\frac{z}{H} = 0.5$. The figure also shows that the return to upstream value is faster for the w-component ($\frac{z}{H} \approx 4$) than the v-component ($\frac{z}{H} \approx 8$). It will also be noted that the horizontal profile of the v-component is similar to that of the streamwise component measured by Raine and Stevenson in a wind tunnel.

The latter authors also demonstrated shifts in the dominant frequency of the turbulence. They measured spectra of u' in the open and at three points behind fences of different porosity. At all porosities ($\phi = 0, 0.20, 0.34, 0.50$), the peak frequency increased in the lee. Behind a 50% porous fence at $\frac{z}{H} = 2, \frac{z}{H} = 0.6$, the frequency of peak energy was an order of magnitude higher than in the open. Further downstream at the edge of the quiet zone ($\frac{z}{H} = 6, \frac{z}{H} = 0.6$), the increase in peak frequency was about a factor of three. For the vertical velocity, Wilson (1987) measured the peak frequency of the w' spectra closer to the fence-top ($\frac{z}{H} = 1.4, \frac{z}{H} = 1.0$) to be higher than the upstream value by about a factor of two. These results indicate that close to the fence, the spectrum is dominated by the relatively small scale turbulence shed by the structural elements of the fence, but

further downstream, the spectrum is dominated by the displacement flow and fence top generated turbulence. At $\frac{z}{H} = 15$, the u-spectra have largely recovered the approach flow shape, even if the power at the peak frequency is still two to three times higher. At this point, it is considered that the flow has more or less *forgotten* the influence of fence permeability.

3.2.4 Other Factors Influencing Windbreak Flow

The rate of recovery of mean wind speed also depends on the mean velocity and turbulence of the approaching wind, and so depends on $\frac{H}{z_o}$ and $\frac{H}{L}$. Some workers express the latter as Ri_g at windbreak height (Seginer, 1975a,b; Ogawa and Diosey, 1980). At higher values of $\frac{H}{z_o}$ (obtained either by increasing H or reducing z_o), the drag exerted by the shelter is greater for a given value of the friction velocity u_*. The wind speed minimum behind the shelter is deeper and the windspeed remains slower over the whole lee region (van Eimern et al., 1964). Seginer (1975b) found that increasing roughness to reduce $\frac{H}{z_o}$ from 670 to 80 caused $\overline{u}/\bar{u}_o$ in the lee of a porous fence ($\phi = 0.50$) to increase by 10 to 12% for the horizontal range $7.5 \leq \frac{z}{H} \leq 30$ at $\frac{z}{H} = 0.25$ while remaining unchanged at $\frac{z}{H} < 7.5$. For a fence on a dry disked and harrowed field ($\frac{H}{z_o} = 670, \phi = 0.50$), Seginer (1975a) measured increased $\overline{u}/\bar{u}_o$ in the range $0 \leq \frac{z}{H} \leq 30$ as stability changed from neutral ($Ri_g = \frac{H}{L} = 0$) to extremely unstable ($Ri_g = -1.5; \frac{H}{L} = -1.6$). The maximum effect of the difference in stability was at $\frac{z}{H} \approx 10$ where $\overline{u}/\bar{u}_o$ was about 32% greater for the unstable case. These results suggest that the influence of $\frac{H}{L}$ on the wind field is stronger than that of $\frac{H}{z_o}$, in terms of horizontal range of influence $\frac{z}{H}$ although as Seginer (1975a) noted,

such extreme instabilities, while meteorologically possible, do not occur frequently. Measurements of Jacobs (1985) for σ_u around a solid two-dimensional barrier in atmospheric flow also showed the dramatic effect of thermal stratification of the approach flow on the resulting leeward turbulence. Jacob's results suggest that the effect of $\frac{H}{L}$ on fence-produced turbulence can be of the same order of magnitude as that of porosity effects.

Another consideration is the wind direction, β. Here, the convention that $\beta = 90$ for flow perpendicular to the fence is used. The protected distance d_p is defined to be the horizontal distance normal to the windbreak up to which the mean windspeed near the surface is less than 80% of the approach windspeed, both measured at the same height. With oblique winds, $\bar{u}/\bar{u}_o$ is expected to increase. Seginer (1975b) suggest the relation $\frac{d_p(\beta)}{d_p(90)} \propto \cos\beta$ while Richards (1983; cited by Heissler and deWalle, 1986) suggest proportionality to $\cos^2\beta$.

An additional factor is that the wind reduction is also dependent on the aspect ratio $\frac{D}{H}$ or the fence sidelength to height ratio. Nägeli (1953; cited by van Eimern et al., 1964) stated that $\frac{D}{H}$ must be at least 11.5 with $\beta = 90°$ for the assumption of two-dimensionality of the flow to be justified, although some recent measurements suggests this value to be an underestimate. Mulhearn and Bradley (1977) compared wind reduction in the field at $\frac{z}{H} = 15$ behind Nägeli's fence ($\frac{D}{H} = 11.5$) and a much longer one ($\frac{D}{H} = 47$). It was concluded that at $\frac{z}{H} > 0.5$, the mean velocity field for both fences was not greatly affected by wind direction (and the consequent generation of lateral flows) although the Reynolds shear stress is. This suggests that it is valid to carry out experiments measuring mean velocities behind fences

of modest length in order to test theories which assume two-dimensionality of the mean flow. Shear stress measurements, however, must only be taken on those rare occasions when the wind direction is close to normal ($\pm 10°$, perhaps) to the fence.

In the same study, flow visualization experiments in a wind tunnel using an oil paint technique were conducted for short straight and curved fences in normal and oblique winds to illustrate surface flow patterns in the near lee. Edge effects were obvious for the short porous fences at normal incidence, and at 15° incidence, generation of secondary flows rendered the flow patterns very complicated.

The flow around a semi-circular belt ($\phi = 0.43$), with the convex side facing upstream, was also examined. This configuration would apparently overcome flow distortions due to variable β inasmuch as the air passing over the fence and reaching an observer at the center of the curvature would have followed a vector perpendicular to the fence. Surprisingly, significant divergence of surface flow was revealed, and the mean velocity profiles showed that this surface divergence brought faster moving air down towards the ground and reduced sheltering to a marked degree.

In practice, no matter how long the windbreak is, points near the ends of the windbreak will recieve no protection especially under oblique winds. Flow around ends and the corner effect in which an excess speed and turbulence develop at the corners in such a way as to encroach on the sheltered zone were studied in a wind tunnel by Gandemer (1979). Different types of treatment were proposed, such as placing lateral guiding fins which widen the windbreak and placing *porous cheeks* upwind for about 1H at each end.

3.3 Microclimate Modification

3.3.1 Considerations in Describing Transport of Passive Scalars in Shelter

The fact that changes in mean wind and turbulence patterns caused by the fence are coupled with the changes in microclimatic elements in the lee has been referred to, although qualitatively, in various field measurements done before 1960 in the summary of van Eimern, et al. (1964) and in the recent review by Rosenberg (1979). Despite the large volume of work, however, little insight can be gained regarding the direct effect of shelter. This is chiefly the result of the agronomic nature of many of the works cited. In most of the experiments, a sheltered crop was grown to maturity while various meteorological elements were monitored in the hope that they would aid interpretation of the observed crop growth and final yield responses. With this approach, the direct shelter effect on the microclimate is often masked and becomes indistinguishable from a cumulative biological effect. Sheltered plants may for example develop larger leaf areas and have more open stomata than plants growing in the open, leading to increased evaporation, although the primary effect of shelter may be to reduce water loss. Increased evaporation rates may lower the temperature, although the primary effect of shelter may be to raise air temperatures in the immediate lee of the fence. Another weakness here is that the time scale of the measurements is inappropriate. Micrometeorological processes are best studied using measurements averaged over periods of a few minutes to one hour while meteorological conditions are steady, whereas evaporation estimates, for instance, often cover a period of a day or more (McNaughton, 1983).

In the carefully designed experiment of Miller et al. (1973) using a semi-circular slat fence ($\phi = 0.50$) windbreak constantly moved around in a well-watered, uniform soybean field, measurements of temperature and vapor pressure gradients in conjunction with lysimetrically determined evaporation were done for short averaging times. Reduced water use based on lysimetric measurements was noted leeward when the radius-to-height ratio $\frac{R}{H} = 4.6$. Increased vertical gradients in vapor pressure and temperature were observed and hypothesized to be caused by reduced exchange coefficients. This hypothesis was supported by the observation of reduced values of the exchange coefficient for the vertical turbulent transport of water vapor, K_W, calculated as

$$K_W = \frac{E}{\rho} \frac{p}{\epsilon} \frac{\Delta z}{\Delta e}$$

where E is the amount of water evaporated and $\epsilon = 0.622$.

These results can be loosely interpreted in terms of the quiet and turbulent zones. Diffusivity is related to both the size and energy of turbulent motions, so that in the quiet zone where both TKE and eddy size are reduced, it is expected that turbulent transport will be less efficient. That is, concentration gradients of scalars normal to streamlines are expected to be larger for a given value of the turbulent flux. The converse holds for the turbulent zone. Simplistically, we might postulate that the observed reduction in water use resulted from increased aerodynamic resistance to vapor transport away from the leaves and soil, though the counteracting feedbacks must also be noted (increased resistance to heat loss would imply higher leaf temperature and stronger vapor pressure gradient).

In Miller's experiment, the purpose of regularly moving the fence around was

to assure spatially unbiased soil and crop properties so that when the field was sheltered, short-term changes in evaporation then reflected changes caused directly by the fence. This is to be contrasted to the measurements of Woodruff et al. (1959) behind a 16-year old shelterbelt in Kansas. Although the recorded rise in daytime air temperature at $\frac{z}{H} \approx 4$ relative to upstream conditions is consistent with the concept of turbulent transport in the quiet and wake zones, it cannot be fully attributed to aerodynamic fence effects. The shelterbelt, being a permanent fixture in the field, may have brought about cumulative changes in the soil and crop status so that a cumulative effect cannot be ruled out.

From the foregoing, it may be stated that if the concentration changes of a passive scalar in the lee of a fence are to be attributed directly to aerodynamic fence effects, then there must be a spatially uniform source strength, that is, the flux of that scalar across the surface must be constant. As discussed in Chapter I, the sensible and latent heat fluxes Q_H and Q_{LE} cannot individually be considered as spatially constant sources, but their sum $Q_H + Q_{LE}$ can reasonably be assumed constant. From the flux-profile definitions

$$Q_H = -\rho c_p K_H \frac{\partial \overline{T}}{\partial z} \tag{3.10}$$

$$Q_{LE} = -L_v K_W \frac{\partial \overline{\rho}_v}{\partial z} \tag{3.11}$$

and if $K_H = K_W = K$ (Dyer, 1974), then

$$Q_* - Q_G = Q_H + Q_{LE} = -\rho c_p K(\overline{T} + \frac{L_v}{\rho c_p}\bar{\rho}_v) \tag{3.12}$$

The mean equivalent temperature $\overline{T}_{eq}$ may be written as

$$\overline{T}_{eq} = \overline{T} + \frac{L_v}{\rho c_p}\bar{\rho}_v \tag{3.13}$$

which may be further simplified by using

$$\overline{\rho_v} = \frac{\rho\epsilon\bar{e}}{p}$$

$$\gamma = \frac{c_p p}{\epsilon L_v}$$

to

$$\overline{T}_{eq} = \overline{T} + \frac{\bar{e}}{\gamma} \tag{3.14}$$

Equation (3.12) reduces to

$$Q_H + Q_{LE} = -\rho c_p K \frac{\partial \overline{T}_{eq}}{\partial z} \tag{3.15}$$

which by definition of T_{eq_*} yields

$$Q_H + Q_{LE} = -\rho c_p u_* T_{eq_*} = Q_* - Q_G \tag{3.16}$$

Equation (3.16) defines the scaling temperature T_{eq_*} which will be used to normalize measured changes in $\Delta\overline{T}_{eq}$. The dimensionless parameter $\frac{\Delta T_{eq}}{T_{eq_*}}$ now describes changes in total thermodynamic energy distribution which under some circumstances may be solely and directly a result of the altered aerodynamics.

3.3.2 Scaling Analogy to the Diffusion Problem from a Ground Level Area Source

The governing diffusion equation that is usually used as a basis for describing turbulent dispersion is a statement of the conservation of the suspended material.

Denoting the local concentration of a gas by c [kg/m^3]

$$\begin{aligned}\frac{\partial c}{\partial t} &= -\nabla \cdot \vec{F} \\ &= -[\frac{\partial (uc)}{\partial x} + \frac{\partial (vc)}{\partial y} + \frac{\partial (wc)}{\partial z}] \end{aligned} \tag{3.17}$$

where $\vec{F}$ is the flux vector and it has been assumed that the gas is not destroyed/produced within the flow. Writing u, v, w and c as the sum of the mean and fluctuating parts, expanding, averaging and rearranging gives

$$\frac{\partial \overline{c}}{\partial t} + \overline{u}\frac{\partial \overline{c}}{\partial x} + \overline{v}\frac{\partial \overline{c}}{\partial y} + \overline{w}\frac{\partial \overline{c}}{\partial z} = -[\frac{\partial (\overline{u'c'})}{\partial x} + \frac{\partial (\overline{v'c'})}{\partial y} + \frac{\partial (\overline{w'c'})}{\partial z}] \tag{3.18}$$

Replacing the eddy flux terms by the simplest gradient- transfer forms (cf equation 2.15 et seq) and adopting the Lagrangian derivative $\frac{d}{dt} = \frac{\partial}{\partial t} + \vec{u} \cdot \nabla$

$$\frac{d\overline{c}}{dt} = \frac{\partial}{\partial x}(K_x \frac{\partial \overline{c}}{\partial x}) + \frac{\partial}{\partial y}(K_y \frac{\partial \overline{c}}{\partial y}) + \frac{\partial}{\partial z}(K_z \frac{\partial \overline{c}}{\partial z}) \tag{3.19}$$

For steady-state ($\frac{\partial \overline{c}}{\partial t} = 0$), horizontally homogeneous surface and aligning axes such that $\overline{v} = 0$ equations (3.18) and (3.19) reduce to

$$\overline{u}\frac{\partial \overline{c}}{\partial x} = \frac{\partial}{\partial z}(K_z \frac{\partial \overline{c}}{\partial z}) \tag{3.20}$$

For the lower atmosphere, the wind varies with the logarithm of height but this variation makes the manipulation of equation (3.20) difficult. Some workers adopt a power-law form of the wind profile, i.e., $\overline{u}(z) = \overline{u}_1(\frac{z}{z_1})^m$ (Sutton, 1953). For simplicity, the case of the wind constant with height and diffusivity $K = ku_*z$ will be adopted. Solution to equation (3.20) takes the basic form (Pasquill, 1974)

$$\overline{c} = \frac{c_1}{x} e^{-c_2 \frac{z}{x}} \tag{3.21}$$

where c_1 and c_2 are constants. Substituting equation (3.21) into (3.20) fixes c_2

$$c_2 = \frac{\overline{u}}{ku_*} \tag{3.22}$$

To obtain c_1, a boundary condition is needed. For a line source Q_L [kg/ms] at $x = z = 0$ (refer to Figure 3.8) it is clear that

$$Q_L = \int_0^\infty \overline{uc} dz \tag{3.23}$$

must hold true for all $x > 0$ and therefore the value of c_1 is fixed as

$$c_1 = \frac{Q_L}{ku_*} \tag{3.24}$$

Now consider an area source Q_A [kg/m^{2}s] at $z = 0$. By letting an infinitely small segment dx be represented by a line source at its center so that

$$Q_L = Q_A dx \tag{3.25}$$

equation (3.23) may be written as

$$\frac{c}{Q_A/ku_*} = \int_0^\infty \frac{dx}{x} e^{-(u/ku_*)(z/x)} \tag{3.26}$$

The concentration c is scaled by $\frac{Q_A}{ku_*}$ which makes the expression on the left-hand side of equation (3.26) dimensionless

$$\frac{[kg/m^3]}{[kg/m^2s] \div [m/s]}$$

Note the analogy of the expressions

$$\frac{Q_A}{ku_*} = -c_* \tag{3.27}$$

$$\frac{Q_* - Q_G}{\rho c_p u_*} = -T_{eq*} \tag{3.28}$$

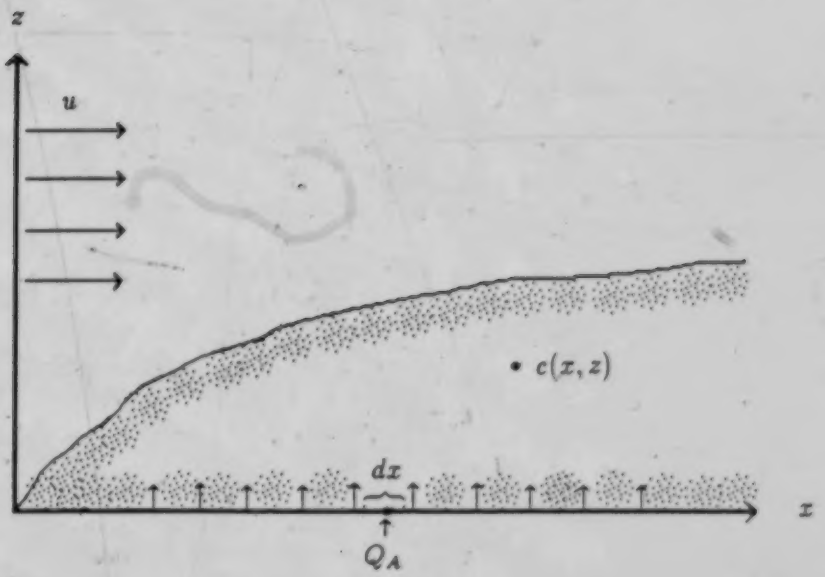

$$Q_L = Q_A dx$$

Figure 3.8 Two-dimensional diffusion problem; the downwind concentration $c(x, z)$ of a gas diffusing from a ground level area source of strength Q_A and with the wind constant with height. The area source is considered to consist of a series of crosswind line sources of strength Q_L so that $Q_L = Q_A dx$ where dx is an infinitely small segment with Q_L at its center.

where c_* is a concentration scale. Here, the negative sign is added in keeping with the convention of defining a positive flux as directed away from the surface.

So by adopting c_* (or T_{eq*}) as a scaling concentration, a formulation is obtained which is insensitive to the variations in the surface flux and the friction velocity.

3.3.3 Expected Trends of $\frac{\Delta \overline{T}_{eq}}{T_{eq*}}$ in Shelter

The only available set of experimental data on $\frac{\Delta \overline{T}_{eq}}{T_{eq*}}$ is provided by McNaughton (1986) for a 50% porous straight fence standing on pasture ($\frac{H}{z_o} = 150$). Measurements were made during the day at near-neutral stratification at $\frac{z}{H} = 0.15$. Inspection of $\frac{\Delta \overline{T}_{eq}}{T_{eq*}}$ will show that positive values denote warming in T_{eq} in the fence lee, since Δ is (by convention herein) the *upstream* $-$ *downstream* value and $T_{eq*} < 0$ during the day when $Q_* - Q_G > 0$. Results showed a zone of warming in T_{eq} extending to about $\frac{x}{H} = 8$, equivalent to Raine and Stevenson's quiet zone. Measurements did not extend beyond $\frac{x}{H} = 9$ but a trend in cooling in T_{eq} beyond $\frac{x}{H} = 8$ was consistently obtained. The maximum scaled T_{eq} was measured at $\frac{x}{H} = 4$ where windspeed was minimum. A schematic diagram of the horizontal trend of scaled T_{eq} in shown in Figure 3.9. The figure speculates that the recovery of T_{eq} to upwind values, after a zone of cooling due to enhanced turbulent difusion will follow the pattern of momentum recovery (Figure 3.5).

In a form similar to the momentum conservation equations describing two-dimensional fence flow (equations 3.1-3.2), the total thermodynamic energy conservation equation is

$$\frac{\partial}{\partial x}(\overline{u}\overline{T}_{eq} + \overline{u'T'_{eq}}) + \frac{\partial}{\partial z}(\overline{w}\overline{T}_{eq} + \overline{w'T'_{eq}}) = S_Q \qquad (3.29)$$

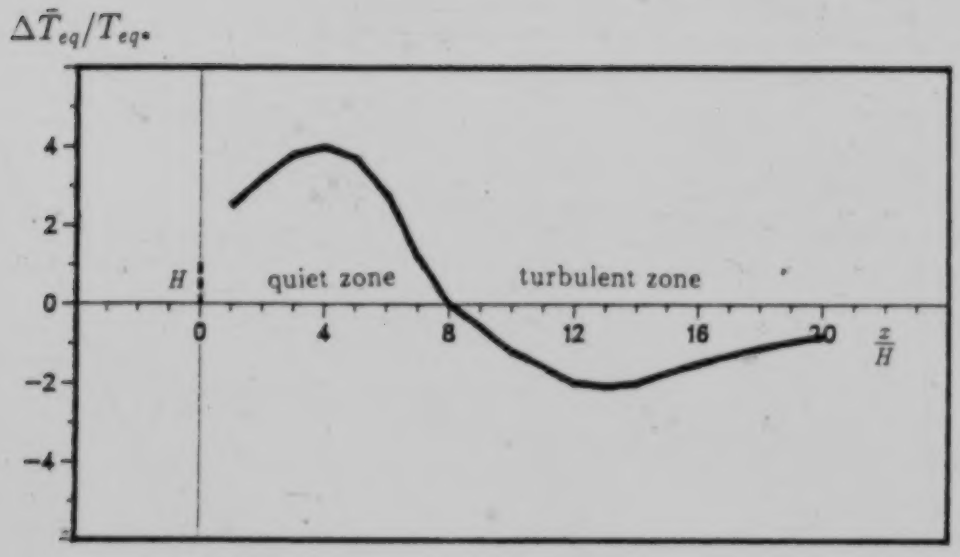

Figure 3.9 Schematic and partly speculative representation of $\Delta\tilde{T}_{eq}/T_{eq}$ across a sheltered field where available energy is uniform $[H/z_o = 150; -0.05 < \frac{H}{L} < 0; \phi = 0.5]$.

The energy sink term S_Q contains such terms as radiant, convective and dissipative flux divergences due to flow/fence interaction. These will be considered negligible so that $S_Q = 0$. An equivalent expression of equation (3.29) is

$$\nabla . \vec{Q}_c = 0 \tag{3.30}$$

where the horizontal energy flux density is

$$\overline{Q}_{cx} = \rho c_p (\overline{u}\overline{T}_{eq} + \overline{u'T'_{eq}}) \tag{3.31}$$

and the vertical energy flux density is

$$\overline{Q}_{cz} = \rho c_p (\overline{w}\overline{T}_{eq} + \overline{w'T'_{eq}}) \tag{3.32}$$

$\overline{Q}_{cz}$ will be termed the advective flux. At $z = 0$ where $\overline{w} = 0$, the vertical flux equals the net available energy

$$\overline{Q}_{cz}(z = 0) = \overline{w'T'_{eq}} = Q_* - Q_G = Q_H + Q_{LE} \tag{3.33}$$

A schematic interpretation of these fluxes is shown in Figure 3.10. All fluxes are averaged values. Far upstream and downstream of the fence, where the surface is essentially undisturbed and horizontally homogeneous, the advective flux $Q_{cz}(x, z)$ is constant in the x-direction. Similarly since we are operating in the constant flux layer, $Q_H(x, z)$, $Q_{LE}(x, z)$ and their sum $Q_{cz}(x, z)$ are constant both with respect to x and z at large distances from the fence. The diagram assumes net energy supply $Q_* - Q_G$ is equally partitioned to heat the air and evaporate surface moisture (Bowen ratio = 1 in undisturbed flow). The convention that positive fluxes are directed as shown by the solid arrows in the diagram is adopted. Here, Q_G is assumed to be horizontally uniform.

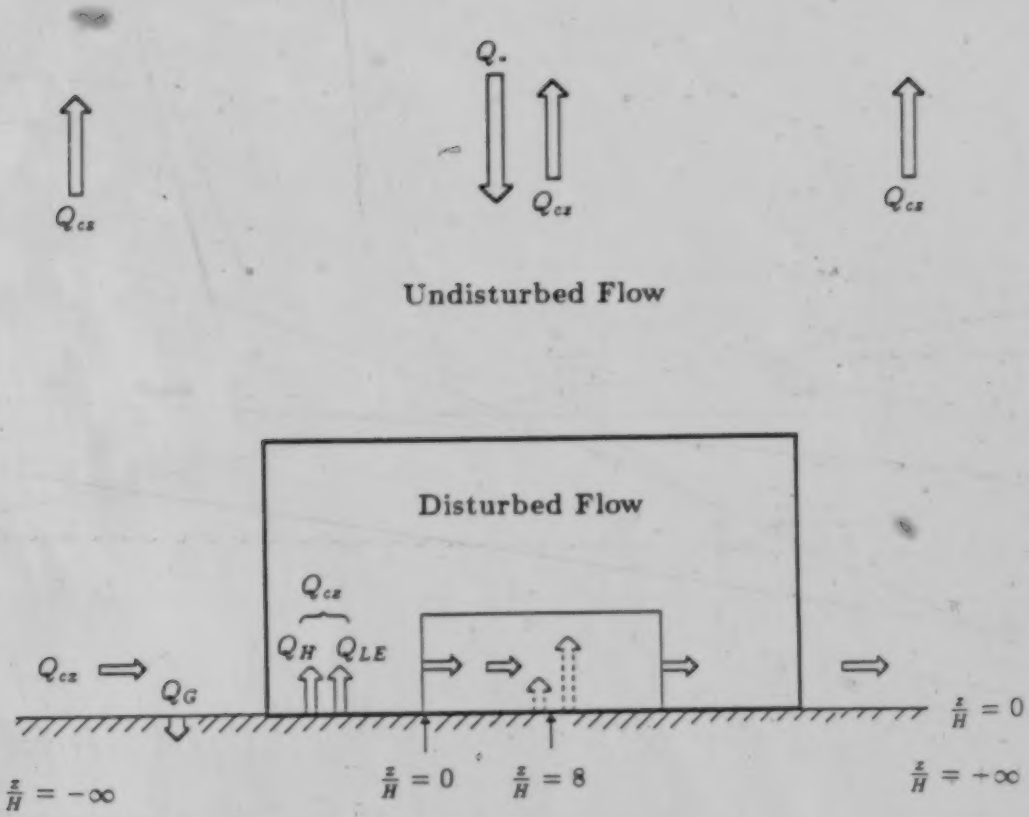

$$
\begin{aligned}
Q_{cz} &= f(x,z) && \text{for } \tfrac{z}{H} > 0 \\
Q_{cx} &= g(x,z) && \text{for } \tfrac{z}{H} > 0 \\
Q_{cz} &= Q_{\cdot} - Q_G && \text{for } \tfrac{z}{H} = 0
\end{aligned}
$$

Figure 3.10 Map of the horizontal and vertical fluxes Q_{cx} and Q_{cz} on a surface layer disturbed by a fenced plot.

Near the fence, Q_{cz} now becomes a function of $\frac{x}{H}$ and $\frac{z}{H}$ as the air flow is modified by the fence. At $\frac{x}{H} = 0$, Q_{cz} retains its upstream value (as long as no shadows are cast) but the partitioning into Q_H and Q_{LE} may change (shown as dashed arrows in the figure) since these two surface fluxes are functions of temperature and moisture both at the surface and directly overhead. At higher levels, $\frac{x}{H} > 0$, changes in Q_{cz} are now coupled with vertical wind velocity changes due to the fence.

Now consider the fenced plot in Figure 3.10 to measure 20m x 20m and the fence height to be 1.25m. $\overline{T}_{eq}$ is measured in the middle of the plot ($\frac{x}{H} = 8$) at $\frac{z}{H} = 0.5$. This observation point is in the turbulent zone where eddy sizes are large and energetic. Let us rewrite the vertical flux profile equation

$$\overline{Q}_{cz} = -\rho c_p K \frac{\partial \overline{T}_{eq}}{\partial z} \tag{3.34}$$

Since the diffusivity K is related to both the size and energy of turbulent motions, it follows from equation (3.34) that at constant $\overline{Q}_{cz}$ (actually for small changes in $\overline{Q}_{cz}$), the vertical gradient of $\overline{T}_{eq}$ will decrease relative to the undisturbed T_{eq} profile, leading to a lower T_{eq} in the plot. This is shown as the dashed curve (a) in Figure 3.11. Decreased gradients imply efficient transport of energy. If the plot size is now reduced to 10m x 10m so that the observation point in the plot center ($\frac{x}{H} = 4; \frac{z}{H} = 0.5$) is in the quiet zone, decreased K and increased gradients lead to warming in T_{eq}, as shown by dashed curve (b). In the figure, $\Delta\overline{T}_{eq}(z)$ is the difference between upstream and plot $\overline{T}_{eq}$ measured at a common height.

In writing equation (3.34), the first term in the right-hand side of equation (3.32) is ignored. The effect of the small downward velocity $\bar{w}$ in the lee of the

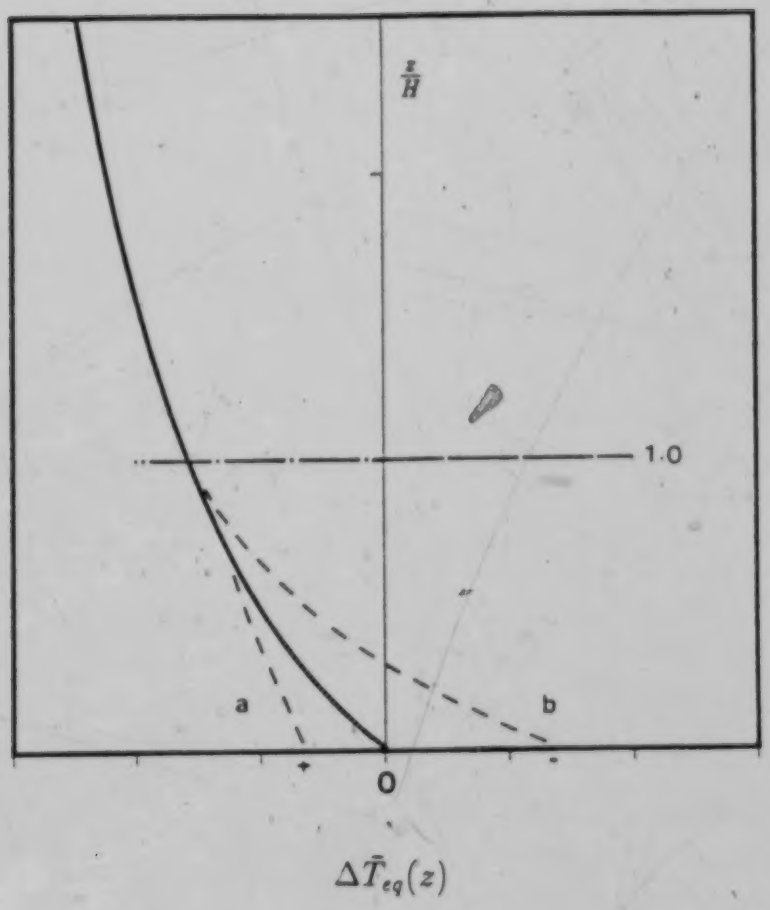

Figure 3.11 Expected changes in T_{eq} in a fenced plot during the day (unstable stratification) at two observation points: (a) turbulent zone and (b) quiet zone. The solid curve represents the T_{eq} profile on the undisturbed surface layer. Decreased (a) or increased (b) vertical gradients of T_{eq} in the plot relative to the undisturbed flow lead to cooling or warming in T_{eq} in the plot.

fence is to transport cool dry air (low T_{eq}) down into the plot (by day). Since it has been observed that the small plot is in fact a region of increased T_{eq} by day, it may be deduced that advection by the mean vertical velocity is not a strong effect. However, it should be emphasized that here a 1-dimensional description based on K-theory is used for a process which is at least 2-dimensional (if not 3-dimensional) involving flow disturbances which K-theory has a doubtful power to describe. Thus the argument must be seen as being qualitative only.

Aside from plot size $\frac{D}{H}$ and measurement height $\frac{z}{H}$, the influence of other scaled parameters such as atmospheric stability $\frac{H}{L}$, surface roughness $\frac{H}{z_o}$ and wind direction β on $\frac{\Delta \overline{T}_{eq}}{\overline{T}_{eq^*}}$ will be investigated.

CHAPTER IV

EXPERIMENTAL PROCEDURE

4.1 Site Description

A series of experiments was conducted at two sites at the University of Alberta farm, Ellerslie, Alberta. The first was done during August 2-21, 1986 over a large flat field covered with alfalfa about 25 cm tall. The second and third experiments were done during October 11-19, 1986 and April 25 - May 26, 1987 over a field about 1 km southwest of the previous site. The field was uniformly covered with closely mown stubble of the previous alfalfa crop. The stubble height was about 5 cm. Both sites, and the university farm as a whole, are relatively flat, with the slope estimated to be less than 1%.

The field layout is shown in Figure 4.1. Because of the prevailing westerly winds, the tower was positioned northwest of the plot so as to measure the undisturbed approach flow. Here, β is measured counterclockwise from the true north so that $\beta = 90°$ corresponds to flow normal to that side of the fence facing the tower. Thus winds blowing from the east ($\beta > 225°$ for the small plot and $\beta > 210°$ for the big plot) are undesirable because the flow approaching the tower is distorted by

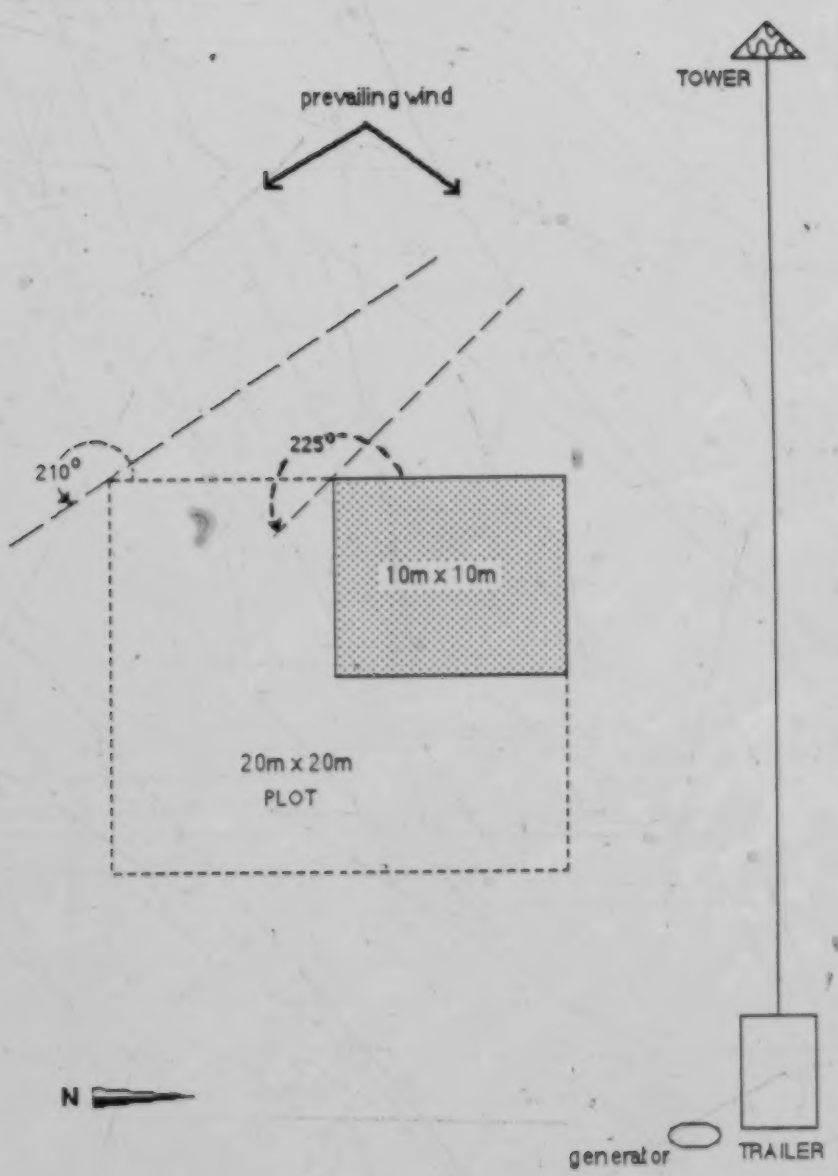

Figure 4.1 Field layout. Easterly winds result to distorted approach profiles at the tower.

the plot. Measurements taken on these occasions were discarded in the subsequent data analysis.

The field layout also considered provision of a height-to-fetch ratio of about 1% (Pasquill, 1972) meaning that a flow which encountered a distortion 100 m upwind may be assumed to have equilibrated to the new surface up to a height of 1 m. The tower being 5.5 m, a fetch of about 500 m was required. Throughout the experiments, the ground cover north, west and south of the tower was uniform within a radius of 500 m. Beyond this distance was a farm road running north-south and an open area growing wheat, barley and canola in various stages of development. The nearest clump of trees was about 800 m north of the tower.

4.2 Set-up and Measurements

The experimental set-up is outlined in Figure 4.2. The 5.5 m lattice-type tower was instrumented with five Climet 011-4 cup anemometers at various heights (z [m] = 0.61, 1.10, 2.10, 3.55, 5.50) and four shielded and ventilated wet- and dry-bulb diode psychrometers (z [m] = 0.61, 1.10, 2.10, 5.50). These instruments provided values of $\overline{u}(z)$, $\overline{T}_{\ell}(z)$ and $\overline{T}_{w}(z)$ to be used in determining the wind and temperature profiles of the approach flow. The cup anemometers were mounted on 1-m long aluminum sidearms. The plot was about 20 m downwind of the tower. A plastic fence with a height H = 1.25 m and a porosity (manufacturer's specification) of 0.45 (Figure 4.3) was put up around a 10m x 10m plot to give a fence sidelength to height ratio $\frac{D}{H}$ = 8. The plot dimensions were doubled in some runs to 20m x 20m giving $\frac{D}{H}$ = 16. The plot center was instrumented with a cup anemometer and

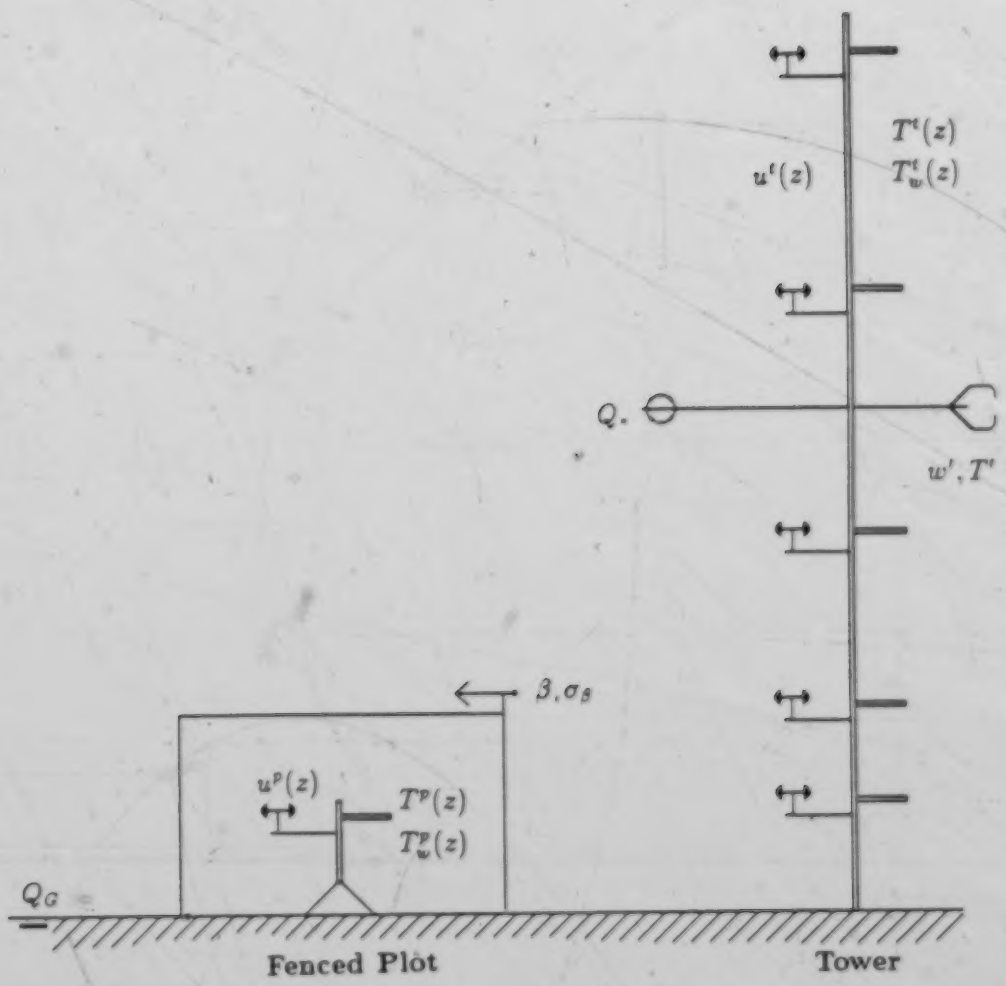

Figure 4.2 Experimental set-up.

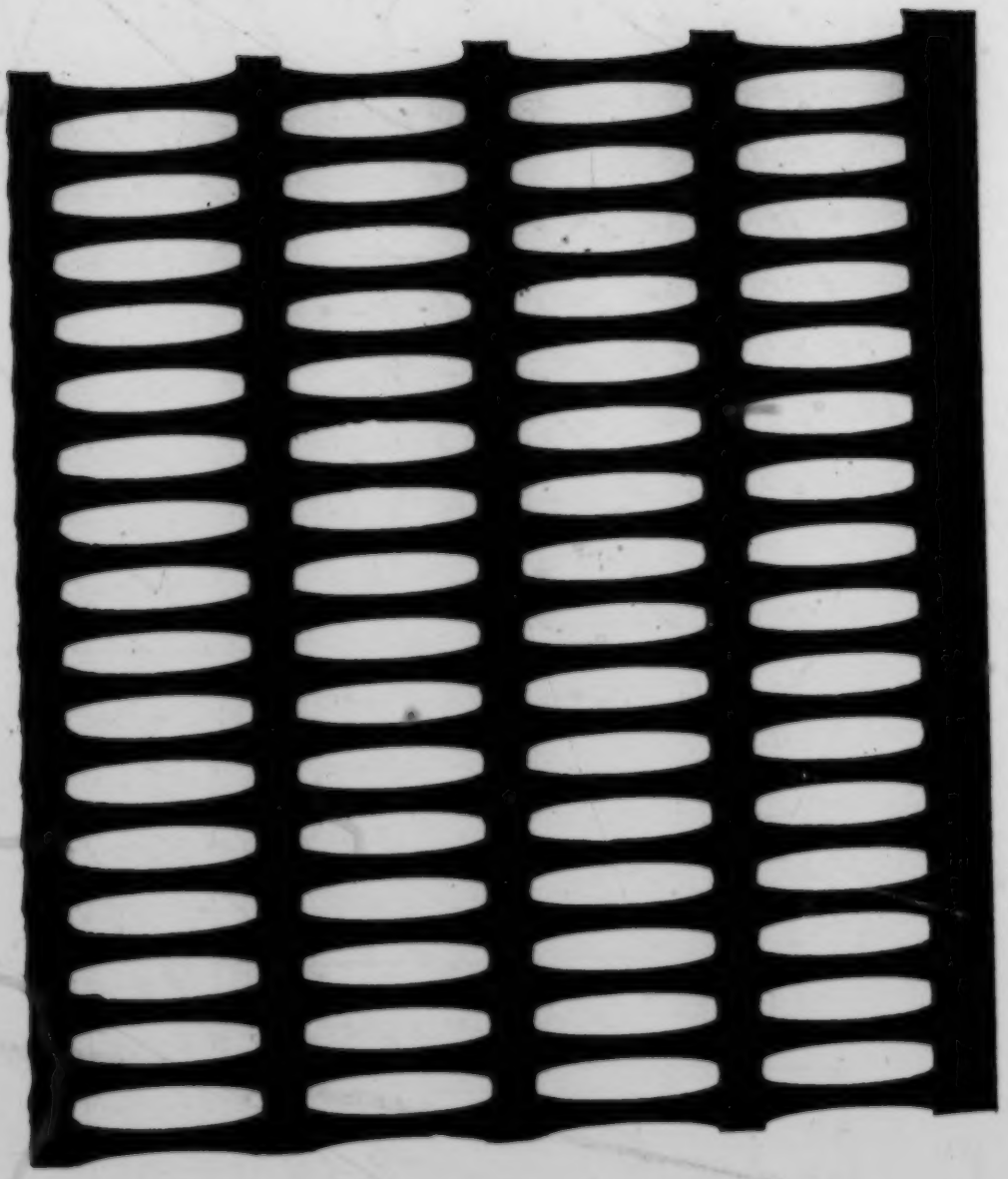

Figure 4.3 Actual size trace of the 45% porosity Tensar fence. (The Tensar Corporation, 2489 North Sheridan Way c/o Gulf Canada Research Centre, Mississauga, Ontario).

psychrometer mounted on tripods at $\frac{z}{H} = 0.5$ or 0.25. This was the same scaled height as the lowest anemometer and psychrometer on the tower. A wind vane was set up on top of an upwind post supporting the fence.

In August, 1986, a sonic anemometer-thermometer [1] and a net radiometer were mounted on the tower at $z = 2$ m. A soil heat flux plate was buried about 5 cm below the ground. These were intended to give direct measurements of Q_*, Q_H and Q_G and, by residual from the energy balance equation, Q_{LE}. The *direct* fluxes served as check on those derived from the profile measurements and thus gave a quantitative measure of confidence in the succeeding experiments.

Extra measurements were done on August 13-14. Four cup anemometers were positioned at $\frac{z}{H} = 0.5$ in the four quadrants of the big plot. At the same time, two psychrometers were employed in the plot: one in the center and the other moved around after two or three runs into each of the quadrants. This allowed measurement of wind and temperature changes relative to the tower at different positions inside the plot. Additional turbulence measurements were done in April-May, 1987 using two single-axis sonic anemometers: one upwind and another at the plot center, both at $\frac{z}{H} = 0.25$. This auxiliary experiment was intended to determine whether changes in vertical velocity fluctuations (σ_w) could help interpret the scatter in the values of the equivalent temperature modification $\frac{\Delta T_{eq}}{T_{eq_*}}$ obtained in the two previous experiments.

Signals were routed to a small trailer and sampled continuously by a CR-7 [2]

---

[1] Campbell Scientific CA27, Campbell Scientific Inc., Logan, Utah

[2] Campbell Scientific Inc., Logan, Utah

data logger. The following sampling intervals were used: psychrometer, 20 s; sonic anemometer, 0.2 s; wind vane, 20 s. Each run lasted 15 minutes. The CR-7 was used as a programmable A/D converter; digitized signals were transmitted to an IBM-PC. A compiled Basic-language program calculated instantaneous vapor pressures and equivalent temperatures from sampled wet and dry-bulb temperatures and accumulated and stored averages. A CR-21X [3] data logger sampled and averaged signals from the sonic anemometers, soil heat flux plate and net radiometer.

Measurements were done from morning to late at night to cover a wide range of atmospheric stability. The experiments were suspended on rainy days. Table 4.1 summarizes the various measurements done at Ellerslie.

4.3 Diode Psychrometry

4.3.1 Diodes as Temperature Sensors

The use of diodes[4] for temperature measurement is based on the dependencies of reverse current on temperature and of the forward current on junction voltage, interacting to produce a linear junction voltage versus temperature relation (Sargeant, 1965). More explicitly

$$\begin{aligned} i &= i_s[\exp(\frac{eV}{kT}) - 1] \\ i_s &= AT^n \exp(\frac{-eE_g}{kT}) \end{aligned} \tag{4.1}$$

---

[3] Campbell Scientific Inc., Logan, Utah

[4] Properties of junction diodes are covered in any electronics or semi-conductor textbook and will not be discussed here.

Table 4.1 Summary of Measurements

Date	August,1986	October,1986	April-May,1987
Parameter			
Fence height H [m]	1.25	1.25	1.25
Grass height h [m]	0.25	0.05	0.05
Displ height d [m]	0.15	0.00	0.00
Porosity ϕ	0.45	0.45	0.45
H/z_o	25	200	200
z/H	0.50	0.50	0.25
D/H	8	8	8
	16	16	16
No. of runs	185	75	138
Variables			
Tower	$\overline{u'}(z), \overline{T'}(z), \overline{T'_w}(z)$		
Plot	$\overline{u^p}(z), \overline{T^p}(z), \overline{T^p_w}(z)$		
	β, σ_β		
	Q_*, Q_G, w, T		$\sigma^t_w(z), \sigma^p_w(z)$

where V = diode junction voltage

i = diode junction current

i_s = reverse saturation current

e = electronic charge

k = Boltzmann's constant

T = temperature, $^\circ K$

E_g = gap energy, V

A = constant for any diode

n = 3 from simple diffusion theory

Equation (4.1) has been verified for silicon and germanium diodes (Sargeant, 1965), both giving a very linear voltage- temperature characteristic, with a sensitivity of

$$\frac{\partial V}{\partial T}\Big|_i \simeq -2.3mV^\circ C^{-1}$$

for the atmospheric temperature range. The strong points for their use as temperature sensors are the linearity of response and high sensitivity. Several workers have documented the use of diode sensors in the field (Sargeant, 1967; Hinshaw, 1970; Black, 1972; McCaughey, 1977).

4.3.2 Construction of the Diode Sensors

The sensor used in the present work is the IN270 germanium diode. The mounting is shown in Figure 4.4. The diode was first mounted on one end of a 1.5 cm matchstick. The diode terminals (clipped close to the glass) were soldered to a pair of fine twisted pair copper wires (32 AWG) whose ends were then soldered to a

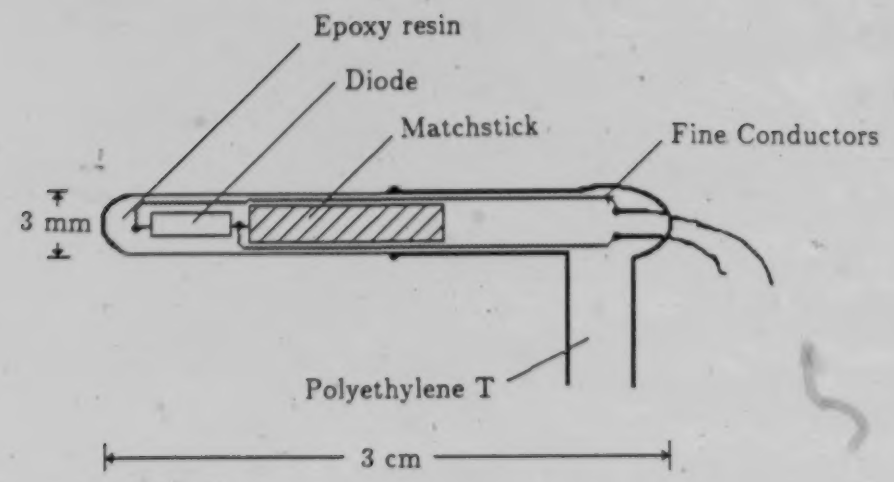

Figure 4.4 The IN270 germanium diode was mounted on wood and polyethylene T and sealed with epoxy resin.

heavier signal wire. The wood-end of the wood-diode assembly was inserted into an arm of a polyurethane T and the whole assembly was sealed with epoxy resin. The other arm of the poly-T was cut close to the junction, the signal wires were led out and the whole unit finally sealed with epoxy from the junction. The whole unit measured 3 cm. in length. Eight pairs, to be used in eight psychrometers, were prepared in the laboratory. Four psychrometers were intended for the tower, two for the plot and two spares.

The basic measurement circuit, patterned after McCaughey (1973) with slight modifications, is shown in Figure 4.5. A constant current is supplied to the diodes by an integrated circuit (Motorola MC1566L). The diodes are connected in series. The voltage drop V across the second diode and the total voltage drop V_t across the two diodes are measured and by difference, V_w is determined. The CR-7 inputs are in the differential mode.

4.3.3 Description of the Psychrometer Assembly

A schematic diagram of the psychrometer assembly is given in Figure 4.6. The sensor pair was housed in a PVC pipe 60 cm long and 2.54 cm ID. A section of the pipe served as trap door by making a longitudinal slice through half the pipe's length. The cut section was attached by masking tape on one side to serve as hinge. Three holes were drilled in the pipe below the trap door to mount the two diodes and the T plastic tubing for the wick. When mounted, the dry-bulb diode was about 7 cm from the air intake end, the tip of the wet-bulb diode 4 cm behind the dry-bulb diode and the wick tubing 3 cm further back. The wick tubing connected

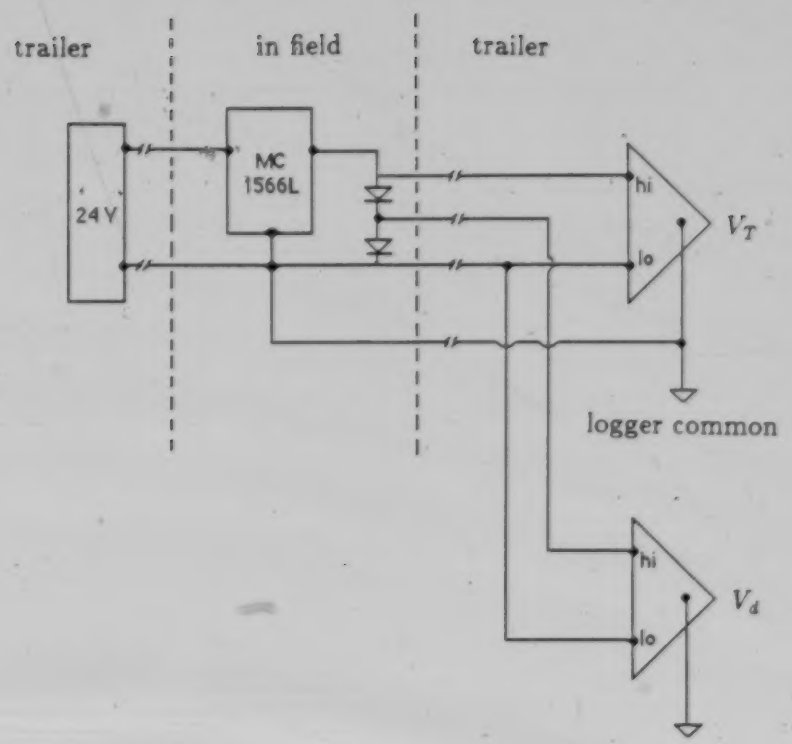

Figure 4.5 Circuit diagram of the diode psychrometer set up.

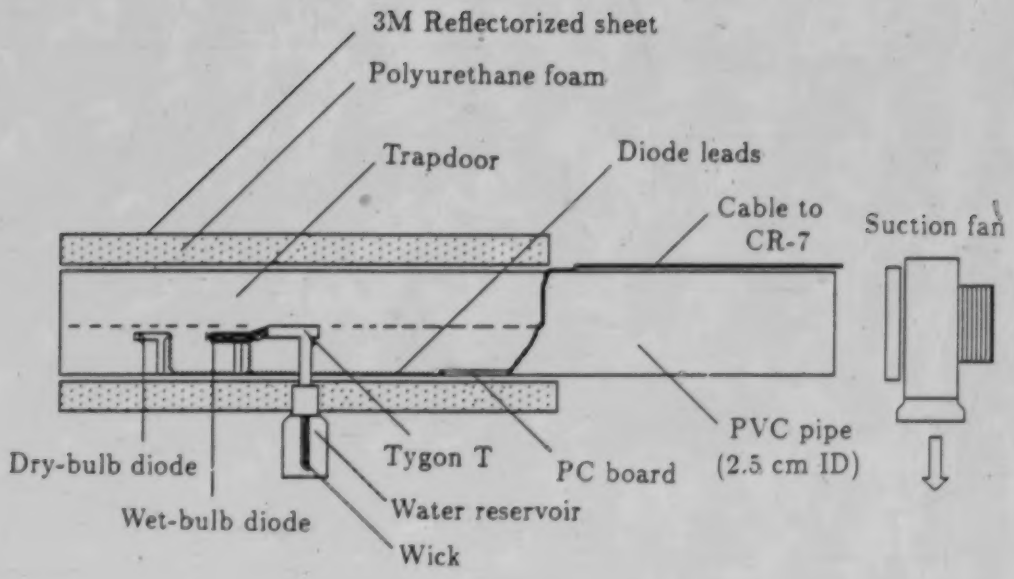

Figure 4.6 Cross-section of the diode psychrometer assembly (not drawn to scale).

through the screw-type lid of a 5-cc plastic water reservoir placed outside the pipe and held securely by epoxy resin onto the PVC. The wick consisted of a previously boiled hollow shoelace (100 % cotton). The wick passed from the reservoir through the plastic T-tubing onto the wet-bulb diode, the total distance from the lid of the bottle to the tip of the wet bulb being 8 cm. The end of the wick was sewn with nylon thread for a close fit around the diode. The PC-board for the constant current circuit was made to sit securely inside the uncut portion of the PVC pipe.

The air intake side of the pipe housing the sensors was covered with a layer of polyurethane 1.5 cm thick and adhesive (3M Scotchlite) reflective sheeting to minimize radiant heating. The diodes were ventilated at a rate slightly exceeding the minimum recommended rate of 5 m/s by a small mains-powered suction fan that was attached to the far end of the pipe.

4.3.4 Laboratory Calibrations

Each diode pair was calibrated in the laboratory before the field experiments. Using a copper-constantan thermocouple with one junction refered to the CR-7 logger panel as reference, the diode pair and the thermocouple were immersed in a temperature-controlled water bath. The CR-7 inputs were the same as in Figure 4.5. The sampling interval was 5 seconds, the averaging time was 1 minute, and each run lasted about 15 minutes to be absolutely certain that the diodes had equilibrated with the bath temperature.

A typical calibration curve and regression equation for the diode assembly are given in Figure 4.7. The reciprocal of the slope of the regression equation

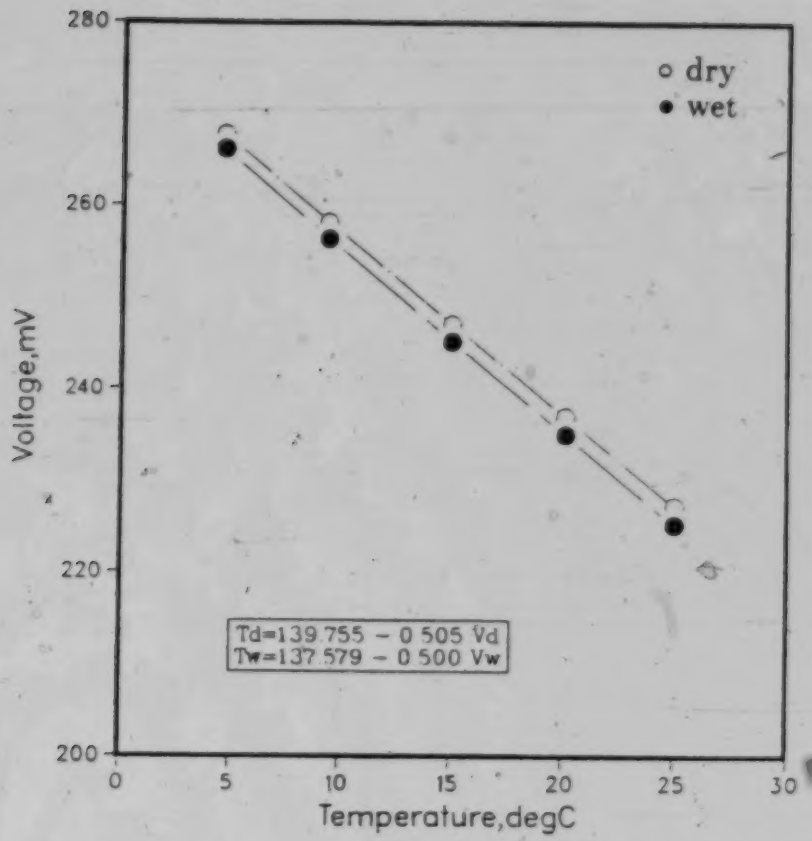

Figure 4.7 Typical calibration curves and regression equations for a diode pair: (○) and (•) represent the diode intended to measure T and T_w.

indicates the sensitivity of the sensor. After individual calibration of the sensors, six psychrometers simultaneously sampling laboratory air gave estimates of T and T_w spanning a range of $\pm 0.05°C$.

4.3.5 Field Comparisons

Field comparisons were done frequently during the experiment to check offsets. All the psychrometers were packed together at 1 m height, facing upstream. Three 15-min runs were then made from which a corrrection table was derived. The correction table consisted of differences in the measured T and T_w values relative to the values given by psychrometer #1. The differences were averaged for the three runs. The corrections for zero drift were then applied to the experimental data of the succeeding runs.

Figures 4.8 (a), (b) and (c) show the applied psychrometer corrections for the three experiments. It is desired that (i) the spread of the values of ΔT and ΔT_w is small and more importantly, (ii) that the corrections for each psychrometer are almost constant from one date of comparison to the next. Results of the August and April comparisons were reasonably stable. With the offsets accounted for, the uncertainty in T and T_w values is about $\pm 0.05°C$ which is the laboratory value. The same cannot be said for the October case. For this reason, the results of the October experiment were scrapped.

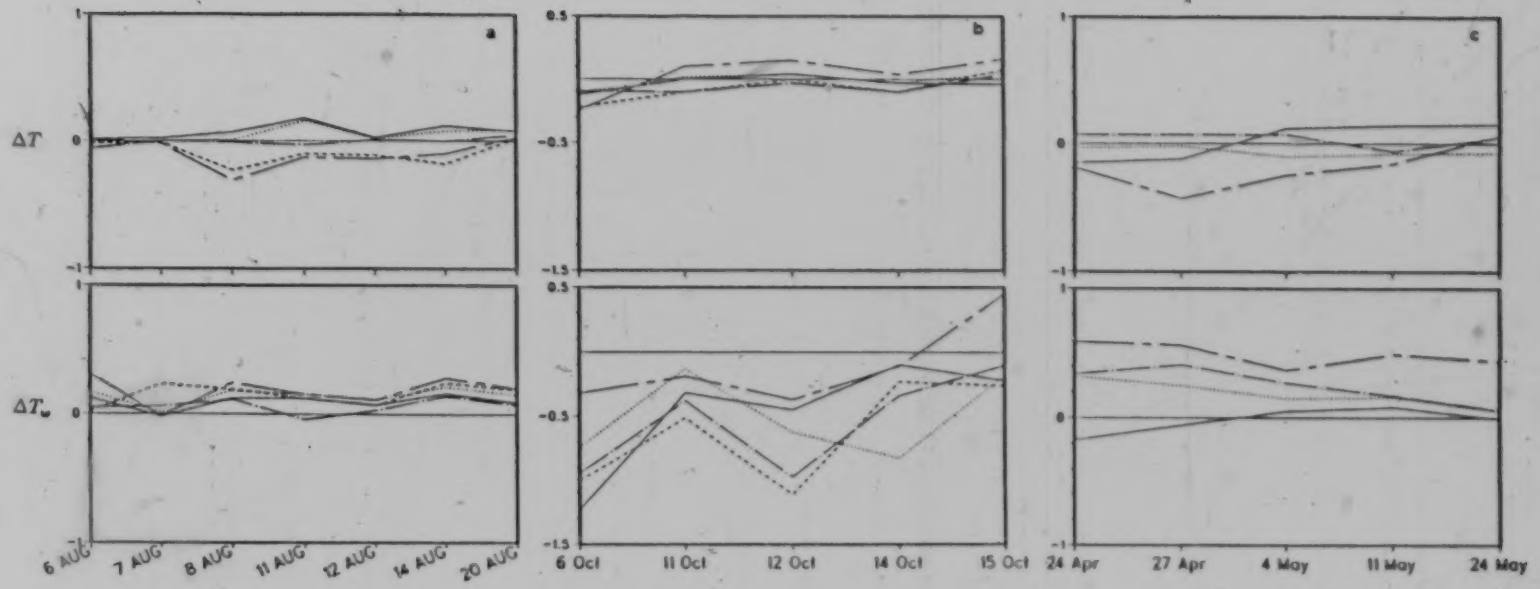

Figure 4.8 Psychrometer corrections determined during various field calibrations: (a) August, 1986; (b) October, 1986 and (c) April-May, 1987.

4.4 Sources of Error in Psychrometry

The errors commonly associated with steady-state psychrometry result from (Tanner, 1971)

1. Inadequate ventilation. This should not be a problem at the suction velocity used here of over 5 m/s.

2. Inaccurate and/or unmatched wet and dry-bulb thermometers.

3. Radiation errors. The psychrometer assembly was shielded with foam (1.5 cm thick) and wrapped with reflectorized sheet.

4. Improper wetting of the wet-bulb; contaminated or dirty wicks, contaminated water, inadequate or excessive water feed.

5. Blunders such as allowing insufficient time for equilibration, omission of pressure correction in γ, and location near local vapor sources, including the operator interaction.

A psychrometry problem was encountered in the experiment when the wick was changed from boiled shoelace to the standard nylon wick used in sling psychrometers. This was done for the October experiment. Since the diodes were much thinner than mercury-in-glass thermometers, the nylon wick fitted the diode quite loosely. The suspected consequence is inadequate wetting of the wet-bulb. The very thin layer of air in places where the wick did not touch the sensor could have presented a high resistance to heat flow. The error was manifested during field calibrations. As shown in Figure 4.8(b), the wet-bulb temperature corrections for

each psychrometer fluctuated wildly between comparisons.

4.5 Definition of T_{eq}, T_w

The enthalpy in a heterogeneous closed system consisting of moist air and water may be written as

$$dh = (\frac{\partial h}{\partial T})_{p,m}dT + (\frac{\partial h}{\partial p})_{m,T}dp + (h_v - h_w)dm_v \tag{4.2}$$

where the specific enthalpy h is refered to a unit mass of the system. It is actually the sum of the enthalpies of the components of the two phases

$$\begin{aligned} h &= m_d h_d + m_v h_v + m_w h_w \\ &= m_d h_d + m_v(h_v - h_w) + m_t h_w \\ &= m_d h_d + m_v Lv + m_t h_w \end{aligned}$$

where $m_t = m_v + m_w$ is the total mass of the water component and $m_d + m_t$ is the unit mass. For an isobaric process, the partial derivatives in equation (4.2) may be written as

$$\begin{aligned} (\frac{\partial h_d}{\partial T})_{p,m} &= c_{pd} \\ (\frac{\partial h_v}{\partial T})_{p,m} &= c_{pv} \\ (\frac{\partial h_w}{\partial T})_{p,m} &= c_w \end{aligned}$$

Substituting these into equation (4.2)

$$dh = (m_d c_{pd} + m_v c_{pv} + m_w c_w)dT + L_v dm_v \tag{4.3}$$

whose integrated form is

$$h = (m_d c_{pd} + m_t c_w)T + L_v(T)m_v + const \tag{4.4}$$

Here the terms T_o, h_o and m_{vo} were collected into an integration constant and the equality $L_v(T) - L_v(T_o) = (c_{pv} - c_w)(T - T_o)$ was used.

Now consider two states linked by an isobaric adiabatic (and therefore isenthalpic) process. The enthalpy h will refer to one and h' to the other state, and since $h = h'$, equation (4.4) may be written as

$$(m_d c_{pd} + m_l c_w)(T' - T) + L_v(T')m'_v - L_v(T)m_v = 0$$

or in simplified form

$$T + \frac{L_v}{c_p} r \cong T' + \frac{L_v}{c_p} r' \cong const \tag{4.5}$$

where the temperature variation of L_v was neglected and various other simplifications were made (Iribarne and Godson, 1973). The mixing ratio $r = m_v/m_d$.

Equation (4.5) is analogous to equation (3.13) and defines the equivalent temperature T_{eq} which is the temperature that moist air would reach if it was completely dried by condensation of all its water vapor, the water withdrawn in a continuous fashion under an isenthalpic process. This can be illustrated by a process which links two specific states; (T, r) consisting of unsaturated moist air and water and (T', r') consisting of unsaturated or saturated moist air without liquid water, where $r' > r$ and saturation is not reached at anytime. The liquid water evaporates and the mixing ratio increases from r to r'. As this water evaporates, it absorbs vaporization heat from the moist air and the water itself because the system is adiabatically isolated. The temperature decreases from T to T'. If the opposite effect is imagined, that is condensation of water, air temperature would increase as condensation heat is released. The process may not be realizable, but in any case

the theoretical temperature the air would have measures the total heat content of the air.

Next consider the case where the mixing ratio of the system goes from r to saturation r_s. This is the process involved in the wet-bulb psychrometer. If the air flowing past the wet bulb is unsaturated, water will evaporate until the air is saturated. If steady state has been reached, the necessary enthalpy must come from the air itself since the water is at a constant temperature. The wet-bulb temperature T_w may thus be defined as the temperature which air attains when water is evaporated into it until saturation is reached while the system is kept at constant pressure and does not exchange heat with the environment. Again using equation (4.5)

$$T_{eq} = T_w + \frac{L_v}{c_{pd}} r_s = T - \frac{L_v}{c_{pd}} r \tag{4.6}$$

In normal meteorological practice, T and T_w are known. To compute T_{eq} the approximations for r and r_s are invoked

$$r \cong \frac{\epsilon e}{p}$$

$$r_s \cong \frac{\epsilon e_s}{p}$$

where e and e_s are the vapor pressures of unsaturated and saturated air, p is the atmospheric pressure and

$$\epsilon = \frac{m_v}{m_a} = 0.622$$

From these it follows that

$$T_{eq} = T + \frac{e}{\gamma} \tag{4.7}$$

$$e = e_s(T_w) - \gamma(T - T_w) \tag{4.8}$$

$$\gamma = \frac{c_p p}{\epsilon L_v} \tag{4.9}$$

It will be noticed that T_{eq} and T_w as linked by equation (4.6) are the maximum and minimum values respectively that the air may attain through the isenthalpic process considered. This may be expressed graphically in Figure 4.9 on a vapor pressure-temperature diagram. The isenthalpic process occurs along the straight line passing through $P(T, e)$ and $P(T, e_s)$ with slope of $-\gamma$. Extending the line toward increasing temperatures, it will intersect the horizontal axis ($e = 0$) at T_{eq}.

The saturation line in the Figure 4.9 is defined by the Clausius-Clapeyron equation

$$\frac{d \ln e_s}{dT} = \frac{L_v}{R_v T^2}$$

which upon integration yields

$$\ln \frac{e_s(T)}{e_o} = \frac{L_v}{R_v}\left(\frac{1}{T_o} - \frac{1}{T}\right) \tag{4.10}$$

Convenient reference values of e_o and T_o are 6.11 mb at $273.15°K$.

The present work used an empirical formula suggested by Campbell (1977) which gave estimates of $e_s(T)$ very close to those obtained from equation (4.10)

$$e_s(T) = 1000 \exp(52.57633 - \frac{6790.4985}{T} - 5.02808 \ln T)$$

The theory of the wet bulb given above does not take into account the possibility that part of the air flowing around the wet bulb may not reach saturation, or that the temperature of air and water may not reach equilibrium. With forced convection (ventilation rate> 5 m/s) and radiation shielding of the sensors, these possible sources of error are minimized.

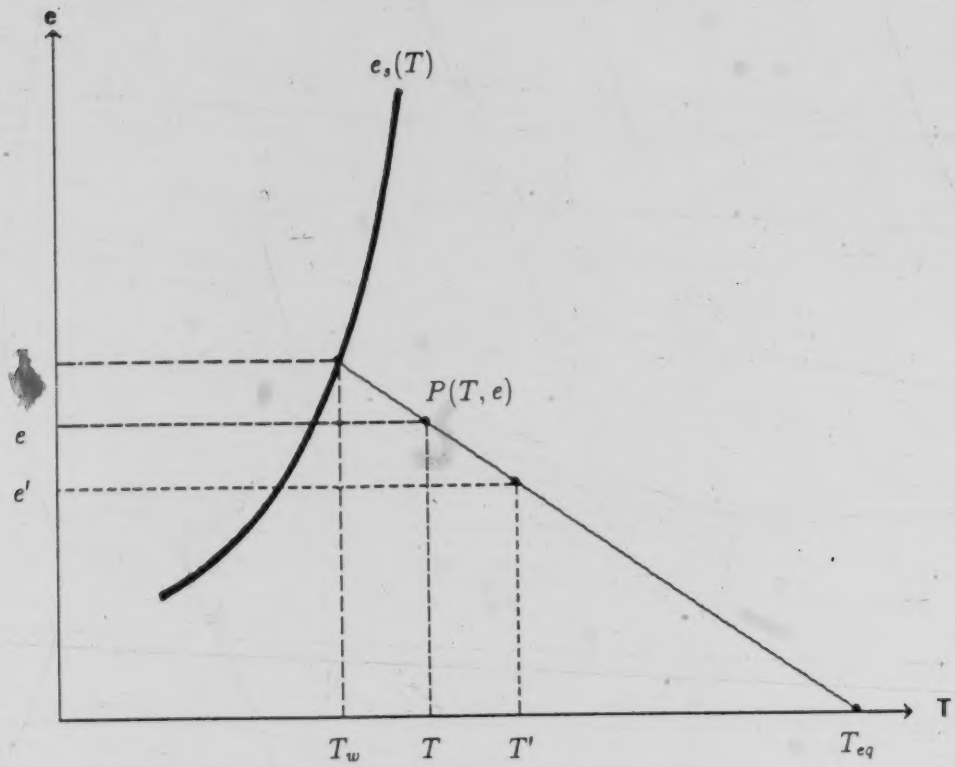

Figure 4.9 Adiabatic isobaric process showing T_{eq} and T_w on a vapor pressure - temperature diagram. The $e_s(T)$ curve is defined by the Clausius-Clapeyron equation.

CHAPTER V

DATA ANALYSIS

5.1 Determination of z_o, d

It will be recalled from Chapter II that for thermally neutral stratification, the air flow over level ground can be described by the log profile equation

$$\overline{u} = \frac{u_*}{k} \ln \frac{z}{z_o} \tag{5.1}$$

When extended to plant communities, the log profile takes the form

$$\overline{u}(z) = \frac{u_*}{k} ln(\frac{z-d}{z_o}) \tag{5.2}$$

where z_o and d are the roughness length and displacement height. The relation

$$d = 0.64h \tag{5.3}$$

suggested by Campbell (1977) was used in this work in calculating d. Here, h is the grass height. The following values of d were deduced: for August,1986, $d = 15$ cm; for October,1986 and April-May,1987, $d \cong 0$. The graphical method of determining z_o was used. For each of the three experiments, neutral runs were selected. These are runs where the heat flux is small and the Monin-Obukhov length extremely large. Inspection of the definition of L will show that such conditions are mostly obtained

on windy mornings a few hours after the surface inversion of the previous night starts to break up, in which case temperatures are almost constant with height, Q_H is low and u_* is high. From equation (5.2), a plot of $\ln(z-d)$ vs $\overline{u}(z)$ gives a straight line with slope $\frac{u_*}{k}$ and z-intercept z_o. A plot of representative neutral runs from the August and April experiments is shown in Figure 5.1. The two runs were taken on August 20,1986 and April 27,1987, both days well within the middle part of the respective experiments. It is expected that values of d would change as the experiment progressed and this would affect the graphically deduced value of z_o. For instance, within the period August 6 to August 20, d increased from 10 cm to 15 cm due to crop growth, and from neutral runs for those two dates, z_o increased from 2.6 to 5.0 cm. This corresponds to a two-fold decrease in $\frac{H}{z_o}$ from 50 to 25. Compared to the surface roughness for April, however, the two-fold change in $\frac{H}{z_o}$ within experiments may be considered small against a ten-fold change between experiments. Therefore, variations in d and z_o within experiments were considered negligible and the following values were considered characteristic

Date	$z_o, [m]$	$\frac{H}{z_o}$
August, October, 1986	0.05	25
April-May, 1987	0.00625	200

It should be noted that the numerical value of z_o depends not only on the size of the roughness elements but also on their spacing and orientation (Shaw, 1982). For rice, Tani (1963) attributes the additional dependence of d and z_o on wind speed to the streamlining effects of waving plants (honami). The determination

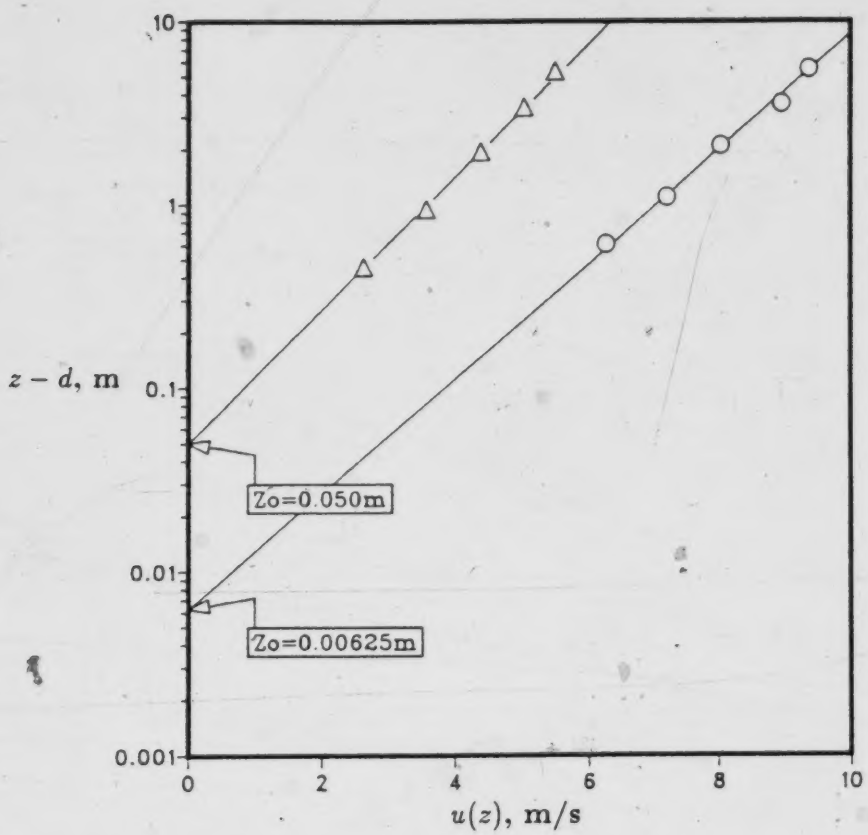

Figure 5.1 Graphical method of determining z_o. Plots of $\ln(z-d)$ against $\bar{u}(z)$ for two representative neutral stratification runs on August 20, 1986 and April 27, 1987 gave respectively z_o of 0.050 m and 0.00625 m.

of z_o, d becomes even more complicated for very rough surfaces ($\frac{z}{z_o} < 50 - 100$); for instance a 3-m sugarcane crop (Cellier, 1986), or a forest (Thom et al., 1975; Paw U, 1987). For the Ellerslie experiments, no such complications were present, so that the straight-forward graphical method was applied with reasonable confidence.

5.2 Determination of u_*, T_* and T_{eq*}

The diabatic profile relations set forth in equations (2.31 et seq.) were used in analyzing the approach flow profiles. These will be written in their basic forms

$$\overline{u}(z) = \frac{u_*}{k}[\ln\frac{z}{z_o} - \psi_M(\frac{z}{L})] \tag{5.4}$$

$$\overline{T}(z) - \overline{T}_o = \frac{T_*}{k}[\ln\frac{z}{z_o} - \psi_H(\frac{z}{L})] \tag{5.5}$$

$$\overline{T}_{eq}(z) - \overline{T}_{eqo} = \frac{T_{eq*}}{k}[\ln\frac{z}{z_o} - \psi_H(\frac{z}{L})] \tag{5.6}$$

where

$$L = -\frac{u_*^3}{\frac{kg}{T_o}\frac{Q_H}{\rho c_p}} = \frac{u_*^2}{\frac{kg}{T_o}T_*} \tag{5.7}$$

5.2.1 Moisture Correction for L, T_v

This definition of L neglects the effect of moisture fluctuations on the density and its effect on the buoyancy. This effect is normally small over land but quite considerable over water (McBean, 1971). For a perfect moist gas, the equation of state takes the form

$$p = \frac{R_*}{M_d}\rho_d T + \frac{R_*}{M_v}\rho_v T \tag{5.8}$$

where R_* is the universal gas constant and M_d and M_v are the molecular masses of air and water. Equation (5.8) may also be written as

$$p = R\rho T[1 + (\frac{M_d}{M_v} - 1)q] \tag{5.9}$$

where the gas constant for dry air $R = \frac{R_*}{M_d}$ and the specific humidity $q = \frac{\rho_v}{\rho_d - \rho_v}$. Now defining the virtual temperature, T_v

$$T_v = T[1 + (\frac{M_d}{M_v} - 1)q] = T(1 + 0.61q) \tag{5.10}$$

equation (5.9) simplifies to

$$p = R\rho T_v \tag{5.11}$$

Here, moisture is accounted for by using T_v in the basic form of the ideal gas law. From $q = \frac{\varepsilon e}{p}$, T_v in equation (5.10) can also be written as

$$T_v = T(1 + \frac{0.38e}{p}) \tag{5.12}$$

From the foregoing, the moisture-corrected L should take the form

$$L = \frac{u_*^2}{\frac{kg}{T_v}T_{v*}} \tag{5.13}$$

where T_{v*}, the slope of the T_v profile of the approach flow, takes the place of T_*.

5.2.2 The Least-Squares Procedure

The values of u_*, T_{v*}, T_* and Teq_* for the experimental runs were determined by fitting the measured profiles to the empirical profile relations using the method of least-squares. This procedure has been reported by Klug (1962) for obtaining u_* from the wind profile; by Paulson (1970) who derived u_* from the wind profile

and T_* from the temperature profile; and more recently by Nieuwstadt (1977) who made simultaneous estimates of u_* and T_* from both profiles. The analysis of the present work is a slight modification of Nieuwstadt's approach. One of the measured velocities (virtual temperatures) is designated the *reference* value, say at height z_u (z_T). These heights need not be the same, and one should not choose an obviously bad measurement to be the reference value. Having established the reference values, measured differences are formed with respect to the reference values

$$\Delta\bar{u}_{m,j} = \bar{u}_{m,j}(z_j) - \bar{u}_m(z_u) \qquad j = 1 \quad n_u - 1 \tag{5.14}$$

$$\Delta\bar{T}_{vm,k} = \bar{T}_{vm,k}(z_k) - \bar{T}_{vm}(z_T) \qquad k = 1 \quad n_T - 1$$

where n_u (n_T) is the number of velocity (temperature) measurement levels. Correspondingly, theoretical differences $\Delta\overline{u}_{t,j}$, $\Delta\overline{T}_{vt,k}$ may be formed over the same height intervals from equations (5.4, 5.5); note that both z_o and T_o vanish in the differences, which depend only upon u_*, T_{v*}. The procedure used was to systematically scan through possible pairs of values u_*, T_{v*} to optimize agreement between the measured and theoretical differences. An iterative procedure in the Basic language, here called PROAN.BAS, was used. The parameters u_* and T_{v*} were found from the condition that the function ϕ reaches a minimum

$$\phi(u_*, T_{v*}) = g_u\phi_u + g_{T_v}\phi_{T_v} \tag{5.15}$$

where

$$\phi_u = \sum_{j=1}^{n_u-1} (\Delta\overline{u}_{m,j} - \Delta\overline{u}_{t,j})^2 \tag{5.16}$$

$$\phi_{T_v} = \sum_{k=1}^{n_T-1} (\Delta\overline{T}_{vm,k} - \Delta\overline{T}_{vt,k})^2 \tag{5.17}$$

The weight factors g_u and g_{T_v} are defined as

$$g_u = \frac{1}{\delta u^2}$$

$$g_{T_v} = \frac{1}{\delta T_v^2}$$

where δu and δT_v are chosen so as to weight the velocity differences and virtual temperature differences in inverse proportion to their respective accuracy of measurement. The values used were

$$\begin{aligned} \delta u &= 0.05 \ m/s \\ \delta T &= 0.10^{\circ}C \\ \delta e &= 15 \ Pa \\ \delta T_v &= 0.10^{\circ}C \end{aligned}$$

The iterative sequence involved

1. determining L from assumed values of u_* and T_{v*};
2. solving equation (5.4) and the T_v version of equation (5.5);
3. solving equation (5.16) and equation (5.17);
4. substituting ϕ_u and ϕ_{T_v} in equation (5.15); and
5. finding u_* and T_{v*} corresponding to ϕ_{MIN}.

The value of L is now determined from the u_* and T_{v*} values found from the loop. Using similar iterations for equations (5.5) and (5.6), T_* and T_{eq*} associated with the minima of ϕ_T and $\phi_{T_{eq}}$ as in equations (5.16, 5.17) are also found.

The rest of the program calculated fluxes and other quantities of interest to be discussed in a later section. On the average, the iterations took about five minutes on an IBM-PC.

The theoretical profiles of $\overline{u}(z)$, $\overline{T}(z)$ and $\overline{T}_{eq}(z)$ defined in equations (5.4) to (5.6) were plotted using a plotting program, here named TEQPLOT.BAS, written in Basic. The inputs to this program were u_*, T_*, T_{v*} and T_{eq*} as well as the tower measurements $\overline{u}_m(z)$, $\overline{T}_m(z)$ and $\overline{T}_{eqm}(z)$. The latter were included in the plots for direct comparison with the theoretical profiles. All points were expressed as differences from a reference, here set as that corresponding to the lowest measurement height. The wind profile for instance is presented as a plot of $\ln(z-d)$ against $\Delta\overline{u}_t(z)$ for the theoretical and $\Delta\overline{u}_m(z)$ for the measured profile, where

$$\Delta\overline{u}_m(z) = \overline{u}_m(z) - \overline{u}(z_1)$$

$$\Delta\overline{u}_t(z) = \overline{u}_t(z) - \overline{u}_t(z_1)$$

The transformation sets the x-axis origin at 0.

Input data and results of analyses using PROAN.BAS are presented for representative unstable, near-neutral and stable stratification runs in Tables 5.1, 5.2 and 5.3. The first five wind data are tower measurements, the sixth is that of the plot center. The first four temperature data are from the tower, the fifth is from the plot center. Comparison of the theoretical approach flow profiles of the wind, dry-bulb and equivalent temperatures under these stratification conditions are then shown in Figures 5.2, 5.3 and 5.4. The tower measurements are denoted by the data points.

Table 5.1 PROAN.BAS input and results for a representative unstable stratification run.

Run no.	Teq9a4.dat			Wind Data	
Date	9 Aug 86			z,[m]	$\bar{u}(z)$[m/s]
Time	1126			Tower	
				0.61	1.11
				1.10	1.33
				2.10	1.57
				3.55	1.70
				5.50	1.78
				Plot	
				0.61	0.68

Thermodynamic Data

z,[m]	$\bar{T}(z)$ [C]	$\bar{T}_w$ [C]	$\bar{e}(z)$ [N/m^{-2}]	$\bar{T}_v(z)$ [C]	$\bar{T}_{eq}(z)$ [C]
Tower					
0.61	16.73	12.52	1190.00	291.13	35.70
1.10	16.32	11.98	1130.59	290.64	34.35
2.10	15.98	11.58	1090.26	290.26	33.38
3.55	15.89	11.33	1058.00	290.12	32.78
Plot					
0.61	17.88	13.00	1195.14	292.28	36.92

Best fit from gradients

u_* [m/s]	0.17	$\Delta\bar{u}/\bar{u}_o$	0.39
T_{v*} [C]	-0.40	$\Delta\bar{T}_{eq}/T_{eq*}$	1.02
T_* [C]	-0.34	H/L	-0.23
T_{eq*} [C]	-1.19	Q_H [W/m^2]	66.09
L [m]	-5.35	Q_{LE} [W/m^2]	165.22

Table 5.2 PROAN.BAS input and results for a representative near-neutral run.

Run no.	Teq21a1.dat			Wind Data	
Date	21 Aug 86			z,[m]	$\bar{u}(z)$[m/s]
Time	1022			Tower	
				0.61	2.09
				1.10	2.75
				2.10	3.51
				3.55	4.03
				5.50	4.36
				Plot	
				0.61	1.07

Thermodynamic Data

z,[m]	$\bar{T}(z)$ [C]	$\bar{T}_w$ [C]	$\bar{e}(z)$ [N/m^{-2}]	$\bar{T}_v(z)$ [C]	$\bar{T}_{eq}(z)$ [C]
Tower					
0.61	15.71	10.26	907.32	289.77	30.12
1.10	15.43	9.82	862.40	289.43	29.13
2.10	15.14	9.38	816.64	289.09	28.13
3.55	14.81	8.88	767.61	288.70	27.01
Plot					
0.61	17.06	11.15	955.48	291.17	32.21

Best fit from gradients

u_* [m/s]	0.44	$\Delta\bar{u}/\bar{u}_o$	0.49
T_{v*} [C]	-0.20	$\Delta\bar{T}_{eq}/T_{eq*}$	3.55
T_* [C]	-0.17	H/L	-0.02
T_{eq*} [C]	-0.59	Q_H [W/m^2]	86.06
L [m]	-71.29	Q_{LE} [W/m^2]	212.63

Table 5.3 PROAN.BAS input and results for a representative stable stratification run.

Run no.	Teq24m6.dat			Wind Data	
Date	24 May 86			z,[m]	$\bar{u}(z)$[m/s]
Time	2330			Tower	
				0.61	1.23
				1.10	1.56
				2.10	2.09
				3.55	2.98
				Plot	
				5.50	3.51

Thermodynamic Data

z,[m]	$\bar{T}(z)$ [C]	$\bar{T}_w$ [C]	$\bar{e}(z)$ [N/m^{-2}]	$\bar{T}_v(z)$ [C]	$\bar{T}_{eq}(z)$ [C]
Tower					
0.31	5.45	4.42	775.02	279.33	17.96
1.10	6.68	5.04	774.94	280.56	19.17
3.55	7.57	5.53	779.68	281.46	20.13
5.50	10.23	6.58	748.07	284.09	22.28
Plot					
0.31	5.76	4.50	765.70	279.63	18.11

Best fit from gradients

u_* [m/s]	0.20	$\Delta\bar{u}/\bar{u}_o$	n.a.
T_{v*} [C]	0.33	$\Delta\bar{T}_{eq}/T_{eq*}$	-0.53
T_* [C]	0.32	H/L	0.14
T_{eq*} [C]	0.29	Q_H [W/m^2]	-75.23
L [m]	8.78	Q_{LE} [W/m^2]	7.05

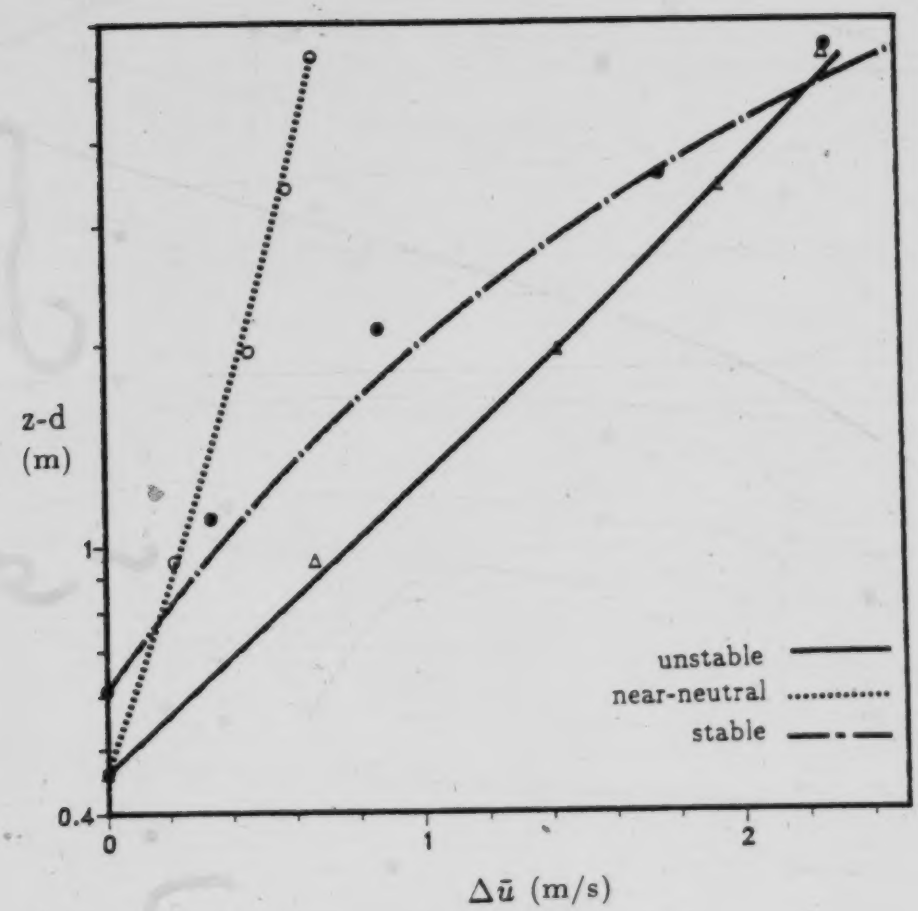

Figure 5.2 Approach flow theoretical (curves) and measured (points) profiles of the wind for the three representative runs in Tables 5.1 - 5.3.

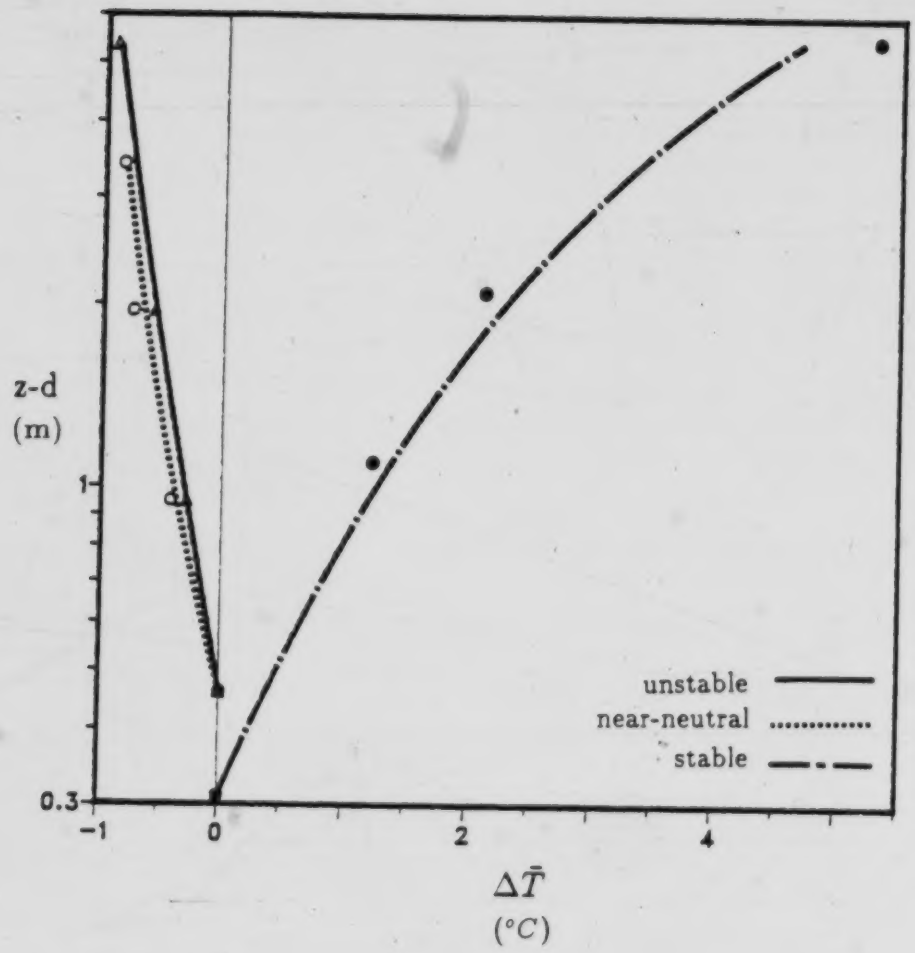

Figure 5.3 Same as in Figure 5.2 but for dry-bulb temperature.

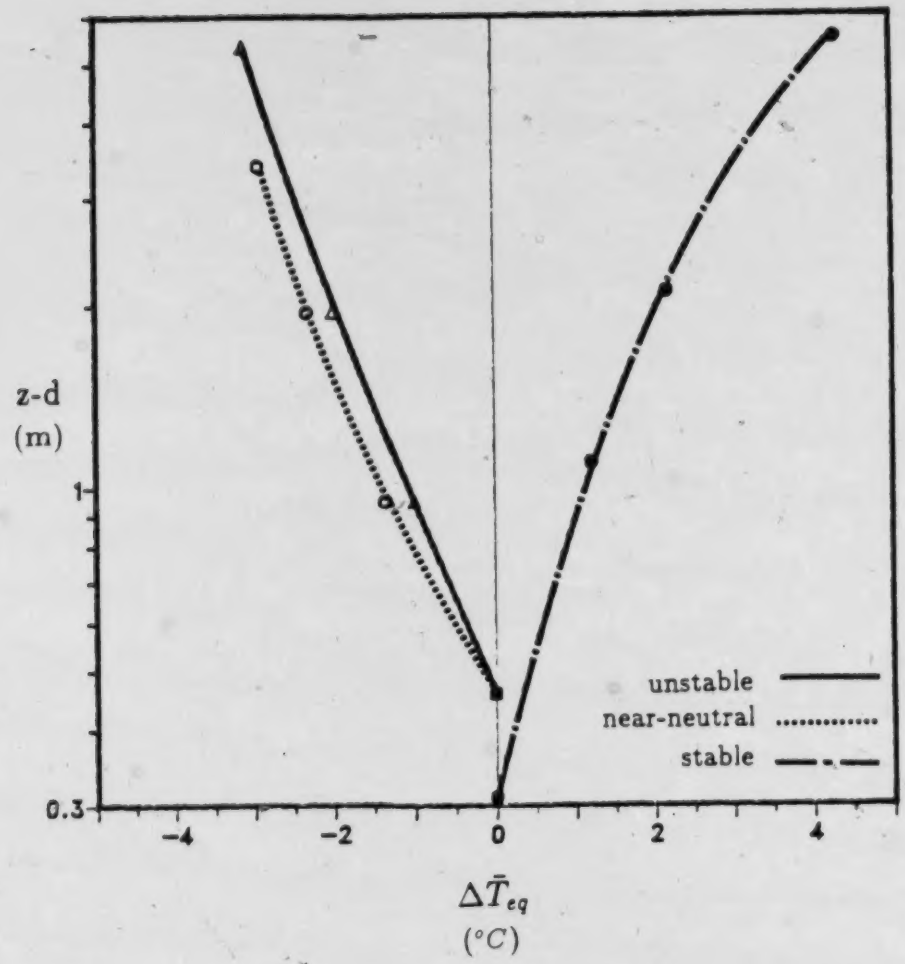

Figure 5.4 Same as in Figure 5.2 but for equivalent temperature.

Based on the terminologies set in Table 4.1, wind reduction and scaled equivalent temperature are henceforth defined as

$$\frac{\Delta \bar{u}}{\bar{u}_o} = \frac{\bar{u}^t(z) - \bar{u}^p(z)}{\bar{u}^t(z)} \tag{5.18}$$

$$\frac{\Delta \bar{T}_{eq}}{T_{eq\cdot}} = \frac{\bar{T}^t_{eq}(z) - \bar{T}_{e^p}(z)}{T_{eq\cdot}} \tag{5.19}$$

where the superscripts t and p refer to tower and plot measurements.

5.3 Criteria for Selection of Acceptable Runs

A run was considered acceptable if the tower measurements $\bar{u}(z)$, $\overline{T}(z)$ and $\overline{T}_{eq}(z)$ gave *good* fits to the theoretical profiles. This condition implies that $u_\cdot$, $T_\cdot$ and $T_{eq\cdot}$ were estimated with reasonable accuracy, that the approach flow was essentially undisturbed, and consequently that changes in plot and tower measurements, $\frac{\Delta \bar{u}}{\bar{u}_\cdot}$ and $\frac{\Delta \overline{T_{eq}}}{T_{eq\cdot}}$, could be attributed solely to fence effects.

As the vertical energy flux density becomes small in magnitude ($|Q_\cdot - Q_G|$ small), vertical gradients in T_{eq} become small so that measurements of differences on the tower are compromised by the limited accuracy of the sensors. The values of $T_{eq\cdot}$ (the slope of the measured $\overline{T}_{eq}$ profile-fit procedure) obtained become small, and subject to an uncertainty which is large relative to their magnitudes. At the same time, measured horizontal differences between the tower and the plot become small and are compromised by experimental error. Similar comments hold for the determination of $u_\cdot$ (which is an intrinsic part of the profile-fitting procedure). Therefore experimental runs were screened as follows

- Any run for which wind direction was not acceptable was immediately dis-

carded.

- Any run for which the theoretical and measured profiles disagreed very markedly was discarded.

- The remaining runs were accepted if

  1. $|T_{eq*}| > 0.15°C$

  2. $\overline{u}(z_1) > 0.6$ m/s

  3. $|T_*| > 0.08°C$

Here criterion (2) ensures accurate measurement of the wind profile (i.e., runs subject to cup stoppages are rejected) and (1), (3) ensure that temperature and equivalent temperature differences be large enough to be measurable.

The trends of u_*, T_*, T_{v*} and T_{eq*} with time on two particular days are shown in Figure 5.5. It is evident that runs with good fits, under the above selection criteria are generally obtained during daytime when winds are moderate and the incoming radiation flux is high, in other words when the atmosphere is unstable. In the early morning and late afternoon which marks the transition period during which the boundary layer adjusts from unstable stratification and vice versa, fits to the profiles were usually bad due to light winds and low radiation flux. Turbulence during this transition period is dominated by non-stationary effects rather than by stability. Good stable runs were obtained late at night on occasions when the winds started to pick up, in which case the wind shear was large enough to maintain a continuous turbulent state; and when dew started to form, in which case both the fluxes Q_H and Q_{LE} were directed downwards, giving $T_{eq*} > 0.15$. In Figure 5.5, it is

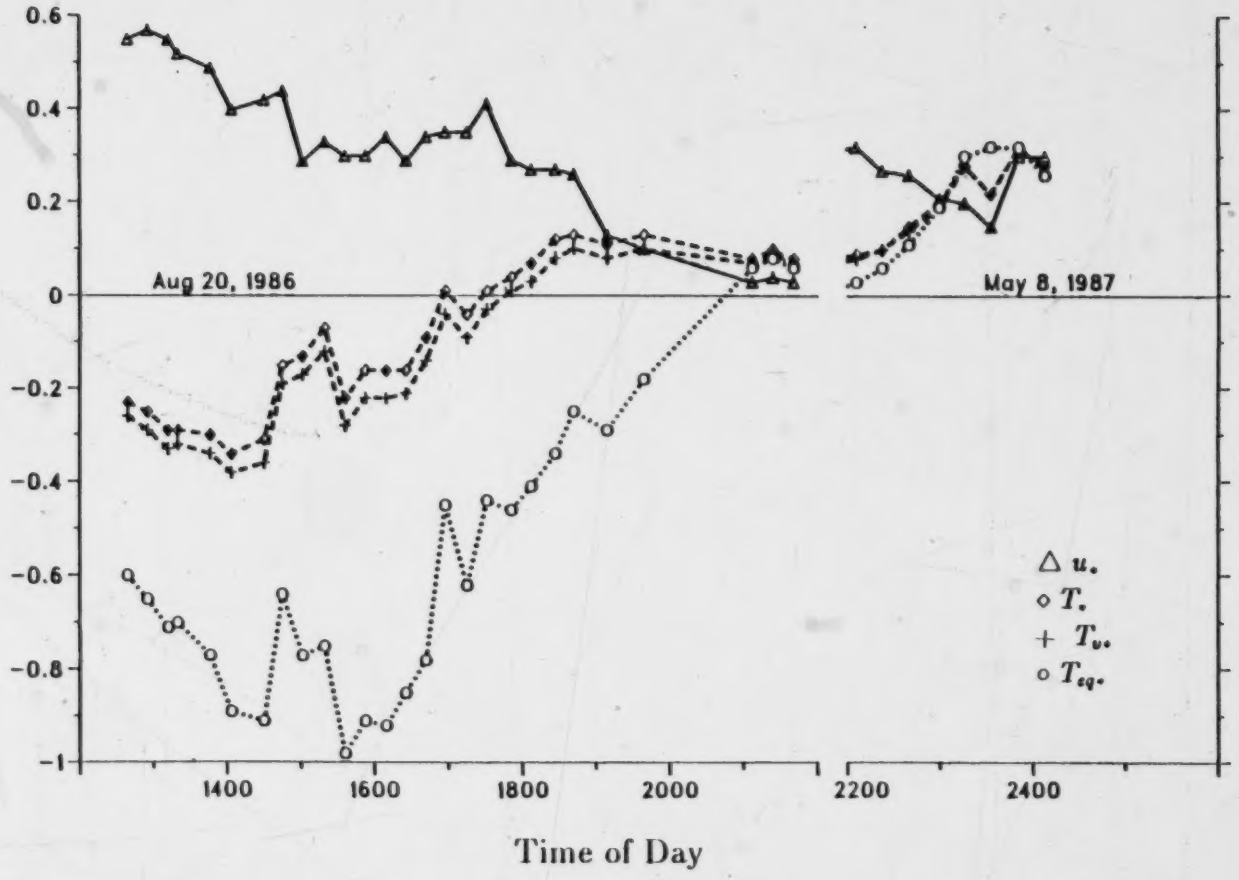

Figure 5.5 Trends of u_*, T_*, T_{v*} and T_{eq*} with time of day.

clear from the low values of u_*, T_*, T_{eq*} that conditions on August 20, 1986 did not give good stable runs but that conditions on the evening of May 8 were acceptable.

5.4 Determination of Q_H and Q_{LE}

The profile method was used for determining the turbulent fluxes of heat and mass, Q_H and Q_{LE}. These were easily derived from the definitions

$$T_* = -\frac{Q_H}{\rho c_p u_*} \tag{5.20}$$

$$Teq_* = -\frac{(Q_H + Q_{LE})}{\rho c_p u_*} \tag{5.21}$$

To check on the accuracy of this method, supplementary measurements were done in the August experiment. Q_H was determined by the eddy correlation method based on

$$Q_H = -\rho c_p \overline{w'T'} \tag{5.22}$$

$$\overline{w'T'} = \overline{wT} - \overline{w}\,\overline{T} \tag{5.23}$$

A sonic anemometer-thermometer measured the instantaneous vertical wind w and temperature T. The signals w, T and wT were logged by a CR21-X data logger, and averaged to obtain $\overline{w}, \overline{T}, \overline{wT}$ at the end of each run. Q_H obtained by eddy correlation will be termed $(Q_H)_{direct}$.[1] A net radiometer and a soil heat flux plate measured Q_* and Q_G. Using Q_H obtained from equation (5.22), the value of $(Q_{LE})_{direct}$ was then found by residual from the energy balance equation

$$Q_* - Q_G = Q_H + Q_{LE} \tag{5.24}$$

[1] The manufacturer's calibration was used.

Figures 5.6 and 5.7 compare the fluxes derived from the gradient method using equations (5.20, 5.21) and from the direct method using equations(5.22, 5.24). The standard deviation for each plot was calculated from

$$S.D. = [\frac{\sum_{i=1}^{n}(Q_{gradient} - Q_{direct})^2}{n-1}]^{\frac{1}{2}} \tag{5.25}$$

where n is the number of observations. From error estimates, the calculated values of S.D. for the two plots were found to be within the acceptable limit of uncertainty due to possible random and systematic error. This gives a quantitative measure of confidence in the profile-derived u_*, T_* and T_{eq_*}.

5.5 Determination of σ_w

The standard deviation of vertical wind velocity defined as

$$\sigma_w = [\frac{\sum_{i=1}^{n}(w - \overline{w})^2}{n}]^{\frac{1}{2}} \tag{5.26}$$

was determined as an auxiliary measurement in the April-May, 1987 experiment. Two sonic anemometers, one at the tower and another at the plot center, simultaneously measured σ_w at $\frac{z}{H} = 0.25$. The scaled difference

$$\frac{\Delta\sigma_w}{\sigma_w} = \frac{\sigma_w^t - \sigma_w^p}{\sigma_w^t} \tag{5.27}$$

gives a measure of turbulence suppression or enhancement in the lee of the fence.

Field comparisons were done on three separate occassions - start, middle and end - of the April-May experiment. With the sonic anemometers both positioned at $\frac{z}{H} = 0.25$ and spaced about 0.5 m apart near the foot of the tower, values of σ_w were logged for each 15-min run. Results of the field comparisons are plotted

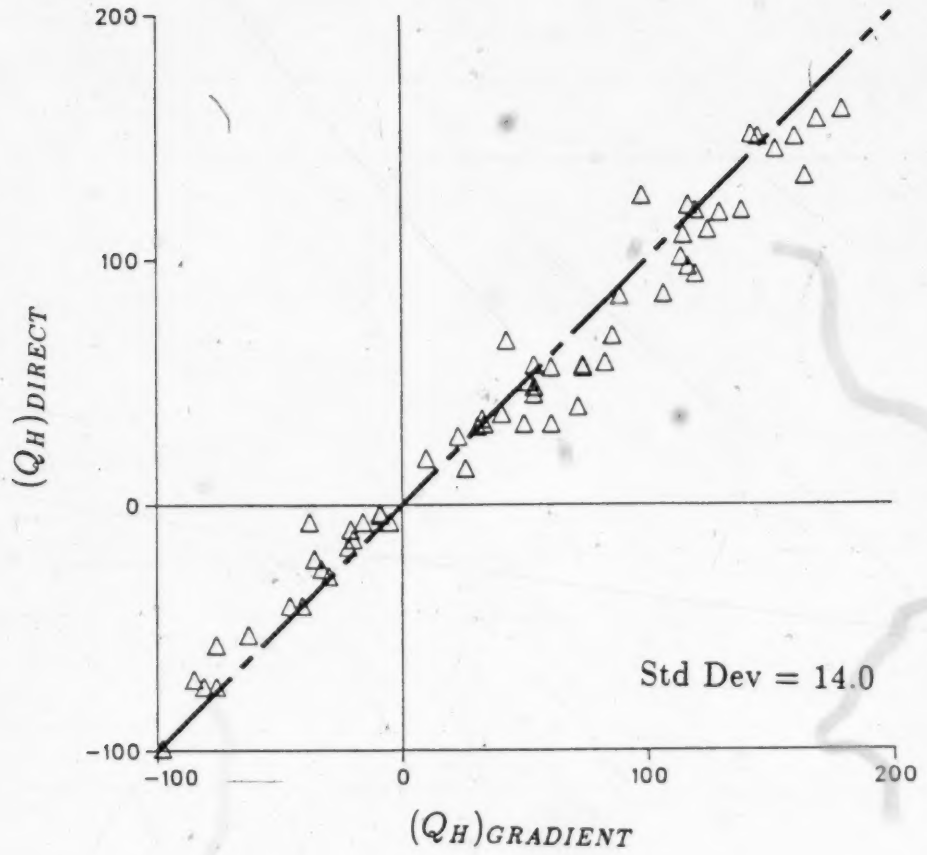

Figure 5.6 Comparison of sensible heat flux $Q_H[W/m^2]$ determined by the gradient method and by direct measurement using eddy correlation. The diagonal is the 1:1 line.

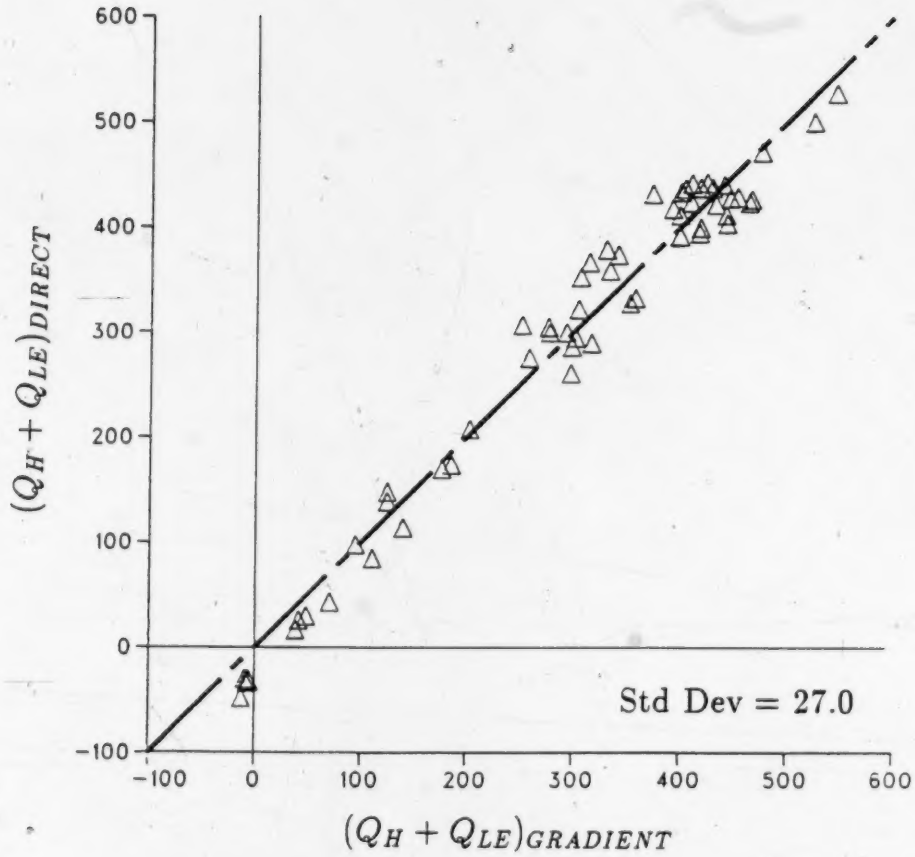

Figure 5.7 Comparison of the total energy flux $Q_H + Q_{LE}[W/m^2]$ determined by gradient method and by direct measurement using the combined energy balance and eddy correlation approach. The diagonal is the 1:1 line.

in Figure 5.8. The consistent agreement of values ($S.D. = 0.02$ ms^{-2}) for the two sonics precluded the need to apply any correction factors to the σ_w values.

One of the predictions of the M-O similarity theory which has been verified by various authors is

$$\frac{\sigma_w}{u_*} = f(\frac{z}{L}) \tag{5.28}$$

Panofsky et al. (1977) suggested the equation

$$\frac{\sigma_w}{u_*} = 1.3[1 + 3(\frac{z}{-L})]^{\frac{1}{3}} \tag{5.29}$$

which provided good fit for observations at large $\frac{z}{-L}$. For stable stratification, Nieuwstadt (1984) obtained the relation

$$\frac{\sigma_w}{u_*} = 1.96[1 - (\frac{z}{\lambda})]^{\frac{3}{2}} \tag{5.30}$$

The boundary layer depth λ is defined as the height at which the vertical heat flux falls to 5% of its surface value. The value of λ was obtained by accoustic sounder. The sonics were positioned at heights 20 m to 200 m.

Results of σ_w/u_* measurements at $z = 0.31$ m in the approach flow in the April-May, 1987 experiment were plotted against $\frac{z}{L}$ in Figure 5.9. The expected variation of σ_w/u_* with $(\frac{z}{-L})^{\frac{1}{3}}$ was roughly approximated, as well as the trend for the stable case, but values were on the whole underestimated. As $\frac{z}{L}$ approached zero, $\frac{\sigma_w}{u_*} \rightarrow 0.8$. Some of the high frequency variance was almost certainly not measured because of the path length of the anemometer (10 cm) which is not small with respect to the measurement height. It should be noted that at distances very close to the ground, the roughness parameter z_o becomes important. In this case, the M-O predictions should be relaxed.

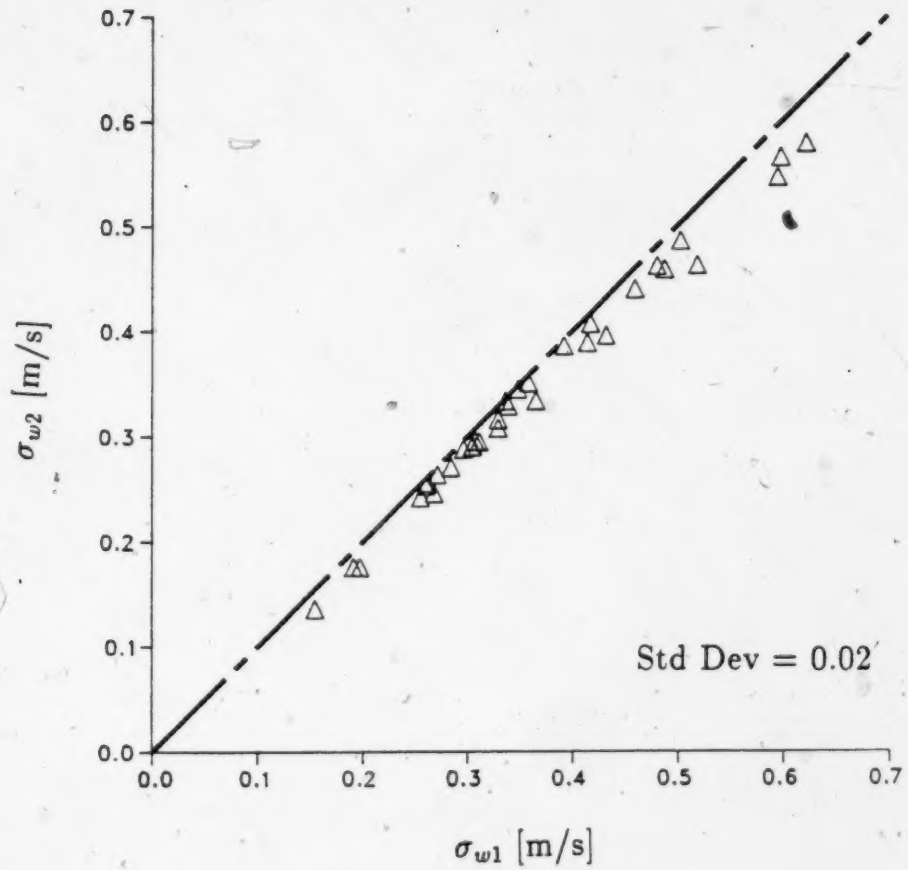

Figure 5.8 Field comparison of two sonic anemometers positioned at z = 0.31 m. Each data point represents σ_w [m/s] averaged over a 15-min period. The diagonal is the 1:1 line.

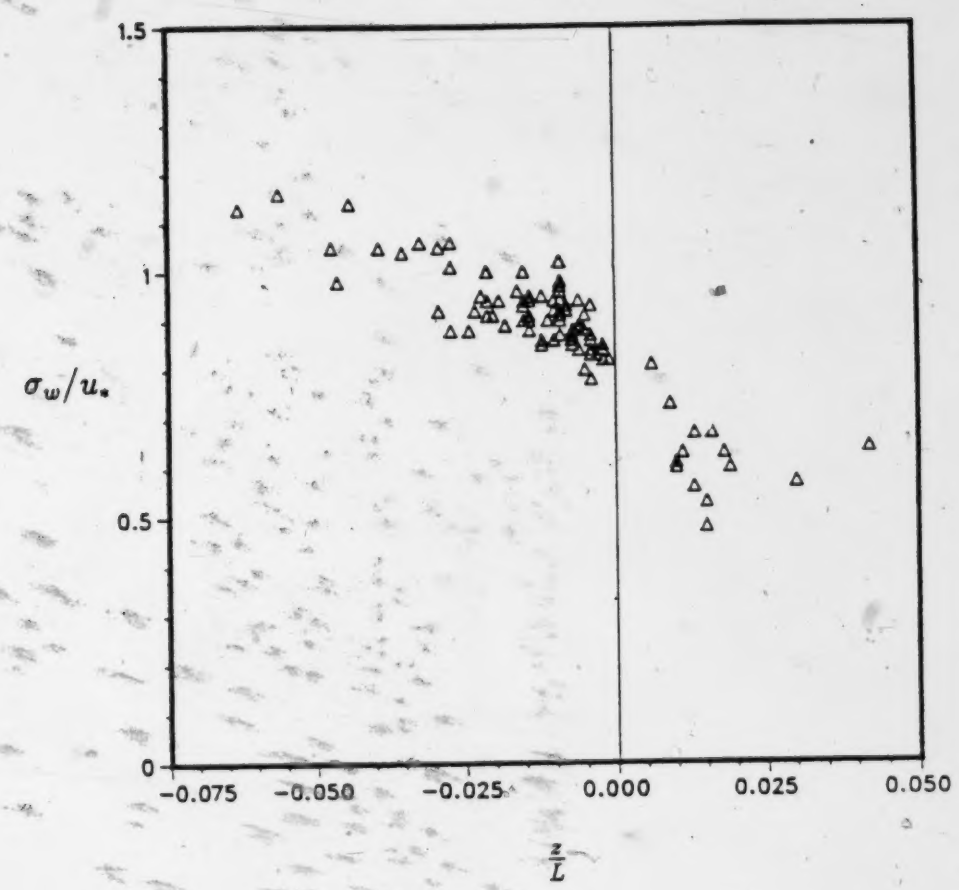

Figure 5.9 Variation of σ_w/u_* with $\frac{z}{L}$ ($z = 0.31$ m) in the approach flow.

CHAPTER VI

RESULTS AND DISCUSSION

6.1 Trends in windspeed reduction $\Delta\bar{u}/\bar{u}_o$

6.1.1 Influence of $\beta, \frac{x}{H}, \frac{D}{H}$

Windspeed reduction determined in the center of the four quadrants of the big plot at $\frac{s}{H} = 0.5$ is shown as a function of wind direction β in Figure 6.1. The wind is blowing normal to that side of the fence facing the tower at $\beta = 90$ and the quadrants are numbered as shown. The dependence of $\Delta\bar{u}/\bar{u}_o$ on β is evident in the quadrants close to the fence, but not for quadrants II and and IV which are situated farther leeward. The most obvious factor underlying this trend is the actual horizontal distance from the fence, $\frac{x}{H}$. Thus, at $\beta = 90$, quadrants I and III being situated about 4H leeward should receive more protection than quadrants II and IV which are at 12H. Additionally, wind reduction in quadrant I should be of comparable magnitude to that in quadrant III; quadrant II to that in quadrant IV. As β departs from normality, say at $\beta = 135$, it would be reasonable to expect quadrants I, III and IV to receive comparable protection, leaving II as the least protected. This trend is qualitatively shown in the figure, notwithstanding the scatter of points attributable to the three-dimensionality of flow in the square plot - the corner effect which was

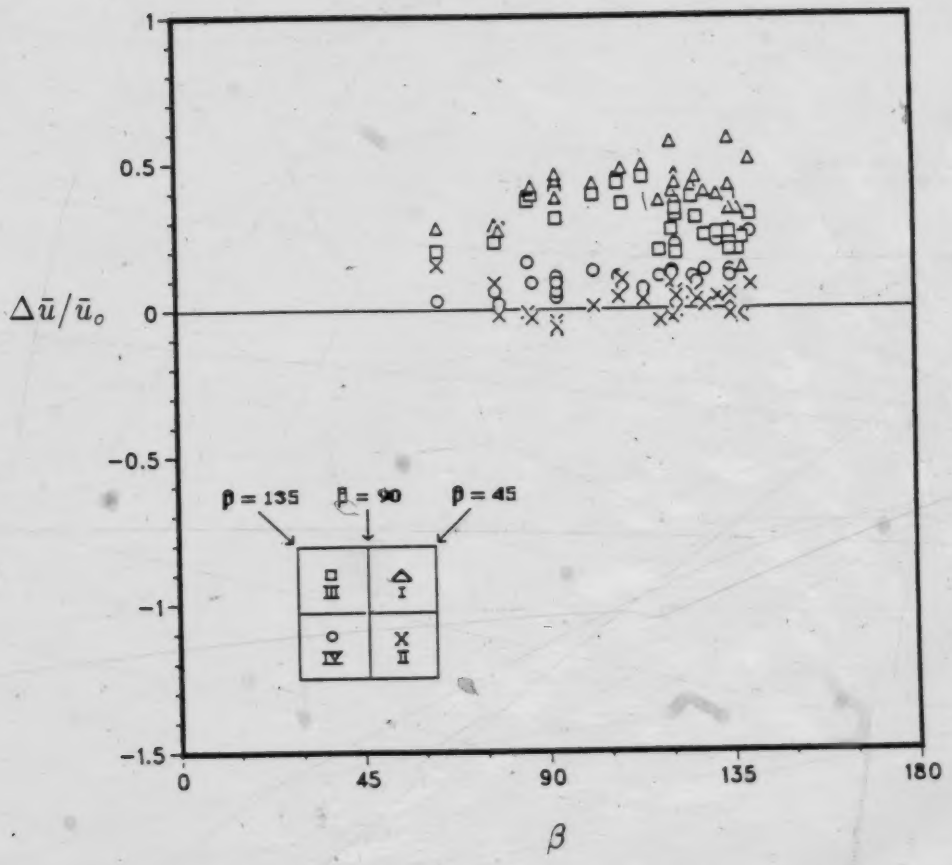

Figure 6.1 Plot of wind reduction $\Delta\bar{u}/\bar{u}_o$ taken at the center of the four quadrants of the big plot as a function of wind direction β.

observed by Gandemer (1979) to shed high energy edddies into the quiet zone, and the confining effect of the fence observed by Mulhearn and Bradley (1977) which brings about a strong surface divergence. These effects, both observed in a wind tunnel, are involved although they cannot be quantified in many of the results of this field experiment.

Further insight may be derived from the data points of Figure 6.1 if windspeed reduction is plotted against $\frac{z}{H}$. Referring to the layout of the big plot shown below, some geometry shows that

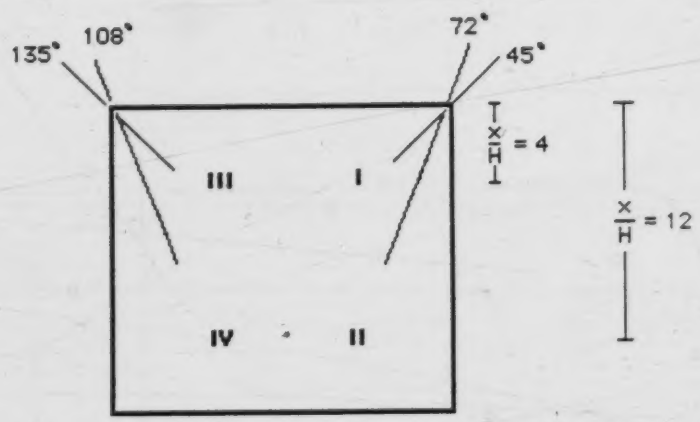

$$
\begin{aligned}
(\frac{x}{H})_I = (\frac{x}{H})_{III} &= \frac{4.0}{\sin\beta} \qquad 45 \le \beta \le 135 \\
(\frac{x}{H})_{II} &= \frac{4.0}{\cos\beta} \qquad 45 \le \beta \le 72 \\
(\frac{x}{H})_{II} &= \frac{12.0}{\sin\beta} \qquad 73 \le \beta \le 135 \\
(\frac{x}{H})_{IV} &= \frac{12.0}{\sin\beta} \qquad 45 \le \beta \le 108 \\
(\frac{x}{H})_{IV} &= \frac{-4.0}{\cos\beta} \qquad 109 \le \beta \le 135
\end{aligned}
$$

and only the range $45 \le \beta \le 135$ need be specified due to the square plot symmetry.

Windspeed reduction as a function of $\frac{x}{H}$ is plotted in Figure 6.2. Three extra runs when a cup anemometer was positioned at $\frac{x}{H} = 1$ were included. The solid curve represents wind reduction behind a straight porous fence ($\frac{D}{H} = 45; \frac{x}{H} = 0.5; \phi = 0.5; \frac{H}{z_o} = 75$) at Ellerslie, Alberta (Wilson, 1987). Wind reduction in the square plot dropped off dramatically at about $\frac{x}{H} = 6$, and remained much lower than the wind reduction behind the straight fence at greater distances. There were even occasions at about $\frac{x}{H} = 12$ when the mean windspeed exceeded that of the open values. The quite rapid recovery of the streamwise velocity as well as the scatter of points beginning at 4H imply the existence of significant lateral flows arising from the square plot configuration. This feature was apparently minimal in Wilson's two-dimensional treatment wherein only runs with winds blowing normal ($\pm 15^o$) to the fence were included.

Windspeed reductions in the middle of the big ($\frac{D}{H} = 16$) and small ($\frac{D}{H} = 8$) plots as a function of β are compared in Figure 6.3. As expected, the mean windspeed was reduced less in the big plot at the center of which $\frac{x}{H}$ ranged from 8.0 (for $\beta = 90$) to 11.3 (for $\beta = 135$) than in the small plot, where $\frac{x}{H}$ varied from 4.0 to 5.7 for the respective values of β. It may be said that the influence of β on $\Delta\bar{u}/\bar{u}_o$ is apparent for both plot sizes, although the trend was more evident for the big plot. Two possible causes of the scatter of points for the small plot may be noted. First, the two-dimensional argument of attibuting wind reduction to changes in β (which is transformed into $\frac{x}{H}$) becomes less predictive as the surface flow patterns become more complicated, a certainty as the effects of small aspect ratio and the confining walls become dominant. Independent measurements of surface shear stresses, for

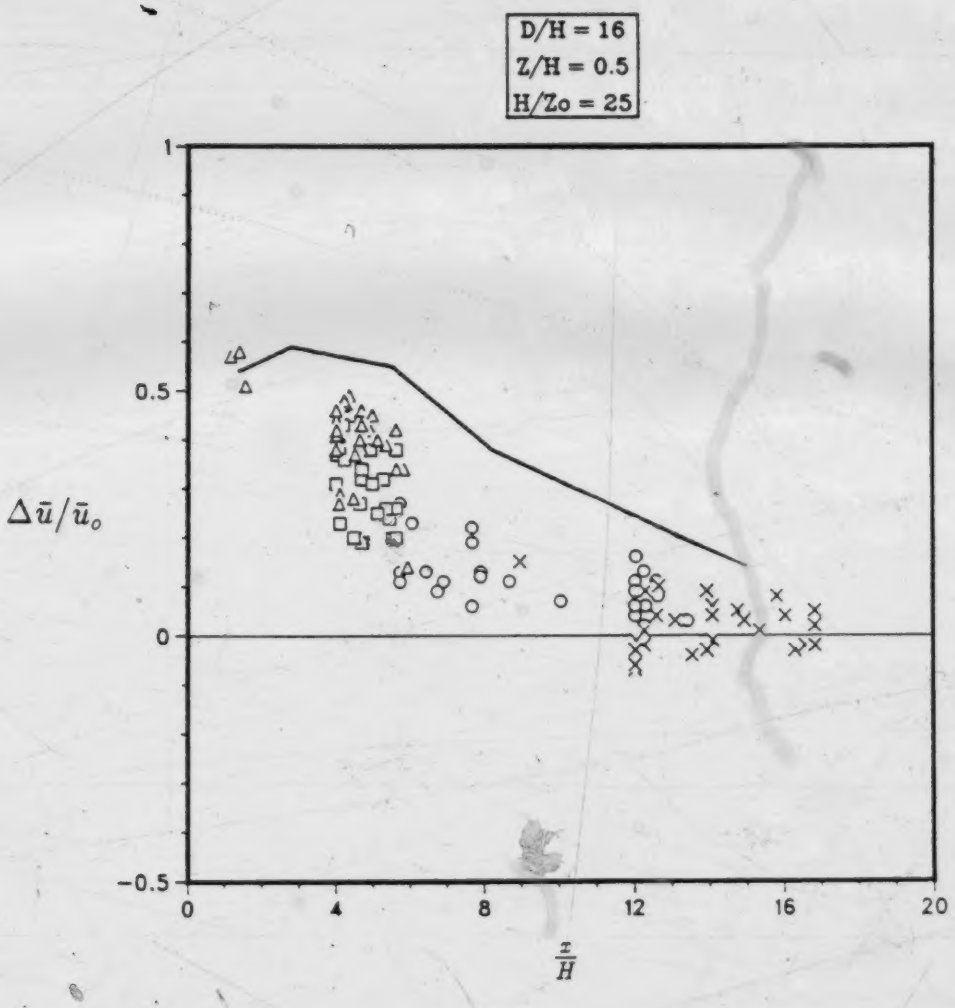

Figure 6.2 Data points of Figure 6.1 plotted as a function of the scaled horizontal distance $\frac{x}{H}$. The solid curve denotes wind reduction in the lee of a straight porous fence ($\frac{z}{H} = 0.5$; $\phi = 0.50$; $\frac{H}{z_o} = 75$; $\frac{D}{H} = 45$) measured in Ellerslie by Wilson (1987).

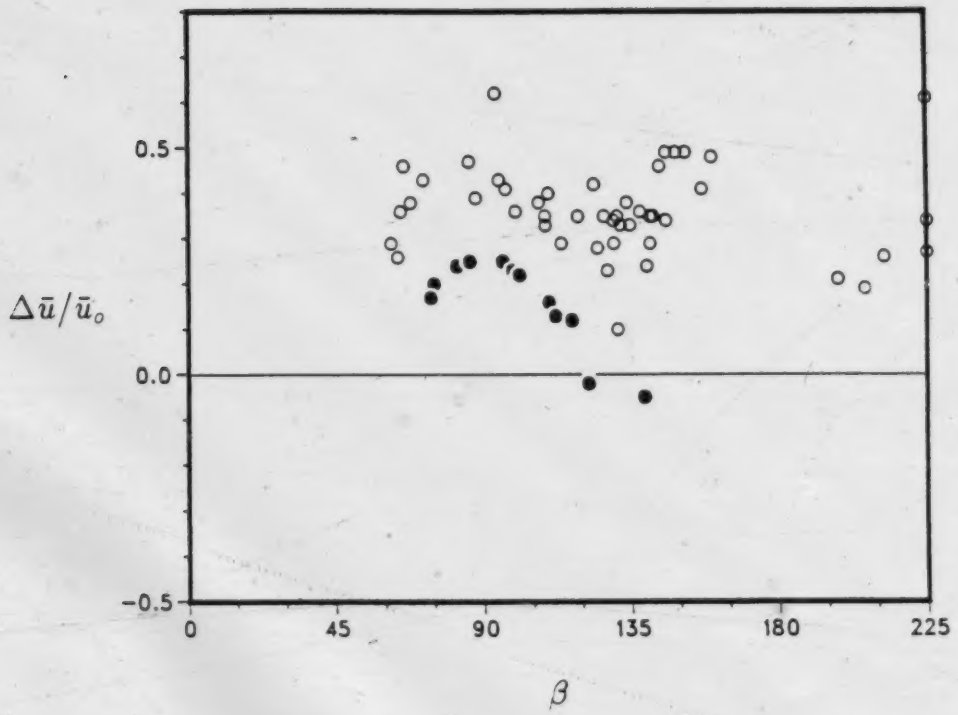

Figure 6.3 Wind reduction for two plot sizes: ○ $\frac{D}{H} = 8$; ● $\frac{D}{H} = 16$, as a function of β, with $\frac{z}{H} = 0.5$, $\frac{H}{z_o} = 25$.

example, could have been instructive at this point. Second, data points for the small plot were taken at a rather wide range of atmospheric stability so that the precise dependence of $\Delta\bar{u}/\bar{u}_o$ on β may have been masked by a dependence upon $\frac{H}{L}$.

6.1.2 Influence of $\frac{H}{L}$, $\frac{H}{z_o}$

Data in Figure 6.3 were plotted as a function of $\ln(\frac{H}{-L})$ in Figure 6.4. These are daytime (unstable stratification) runs. Here, an averaging procedure was imposed on $\frac{H}{-L}$ by

- dividing the runs into stability classes in which the upper and lower bounds were set in such a way that the number of runs is approximately evenly distributed in each stability class;
- taking the mean $\bar{Y}$ for each stability class, where Y represents $\Delta\bar{u}/\bar{u}_o$, $\Delta\bar{T}_{eq}/T_{eq}$, or $\Delta\sigma_w/\sigma_{wo}$ of each run; and
- calculating the sample standard deviation from the mean

$$SD_{\bar{Y}} = \left(\frac{\sum^n (Y_i - \bar{Y})^2}{n^2}\right)^{1/2}$$

In all other figures involving $\frac{H}{L}$ and showing deviation bars, this averaging procedure was applied.

Recalling the definition of L

$$L = -\frac{u_*^3}{\frac{kg}{T_o}\frac{Q_H}{\rho c_p}}$$

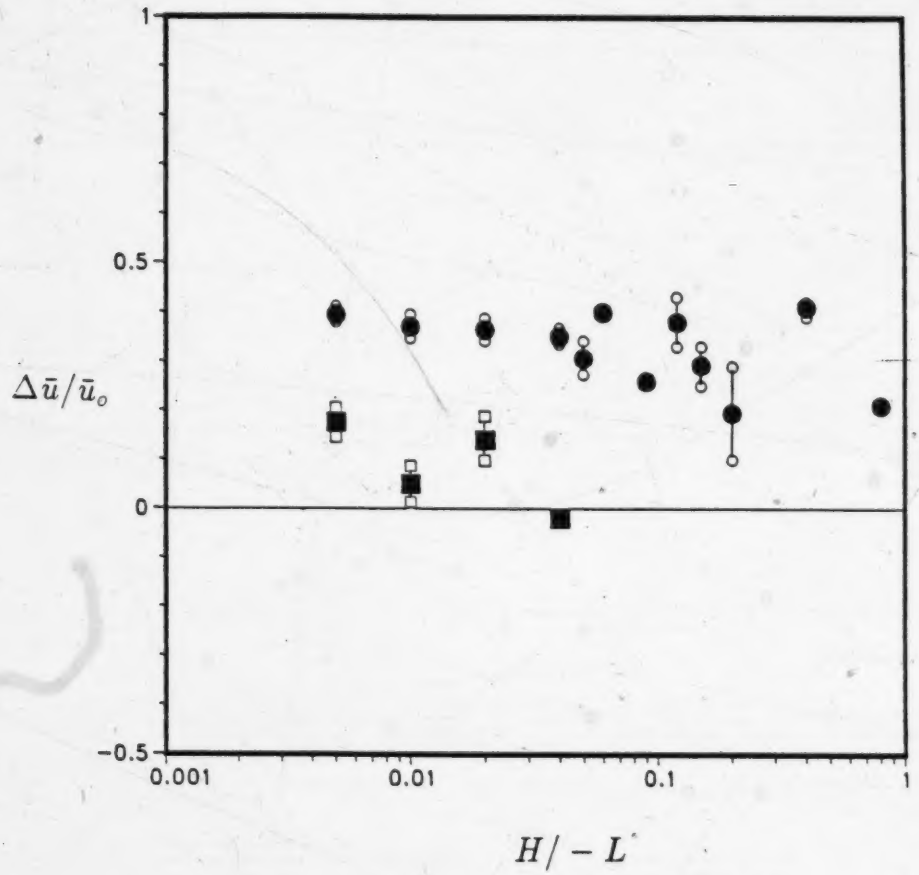

Figure 6.4 Wind reduction for two plot sizes: • $\frac{D}{H} = 8$; ■ $\frac{D}{H} = 16$, with atmospheric stability ranging from near-neutral to unstable. The bars indicate the deviation from the mean within a stability class and data points without bars represent single observations.

and noting that $Q_H > 0$ during the day, it will be seen that large $\frac{H}{-L}$ may be reached by either increasing Q_H or decreasing u_*. Similarly, the near-neutral condition ($\frac{H}{-L} \rightarrow 0$) is obtained by either decreasing Q_H or increasing u_*. Since u_* is roughly proportional to $\bar{u}$, it may be said that at low windspeeds and high insolation typical of very unstable runs, the effect of the fence on the airflow is very small, hence the reduction in $\Delta\bar{u}/\bar{u}_o$ as $\frac{H}{-L}$ increases. For the two square plot dimensions tested, Figure 6.4 indicates that atmospheric stability effect on wind reduction is minimal for the range $0 < \frac{H}{-L} < 1$ at $\frac{x}{H} \approx 4$ and $\frac{x}{H} \approx 8$.

While L is a length scale whose magnitude and sign are indicative of the relative effects of buoyant and mechanical forces and hence the convective state of the atmosphere, z_o is a length scale representative of the roughness elements of the ground which tend to influence the vertical profile of the wind blowing over it. Note that the turbulence parameters $\sigma_{u,v,w}$ do not depend explicitly on z_o but do depend on u_*. With increasing upstream roughness at constant free stream velocity, the drag and hence u_* would correspondingly increase, causing a faster recovery of leeward momentum and a smaller zone of reduced windspeed (van Eimern et al., 1964). The value of $\frac{H}{z_o}$ may be increased (to create a *smoother* surface) by using a higher fence at a fixed z_o, or equivalently by decreasing z_o at a fixed H. In Figure 6.5, an eight-fold increase in $\frac{H}{z_o}$, from 25 to 200, showed a corresponding increase in wind reduction of roughly 50%. The corner effect ($\beta = 45, 135$) was also evident. These latter results constitute the only reliable data from the October experiment.

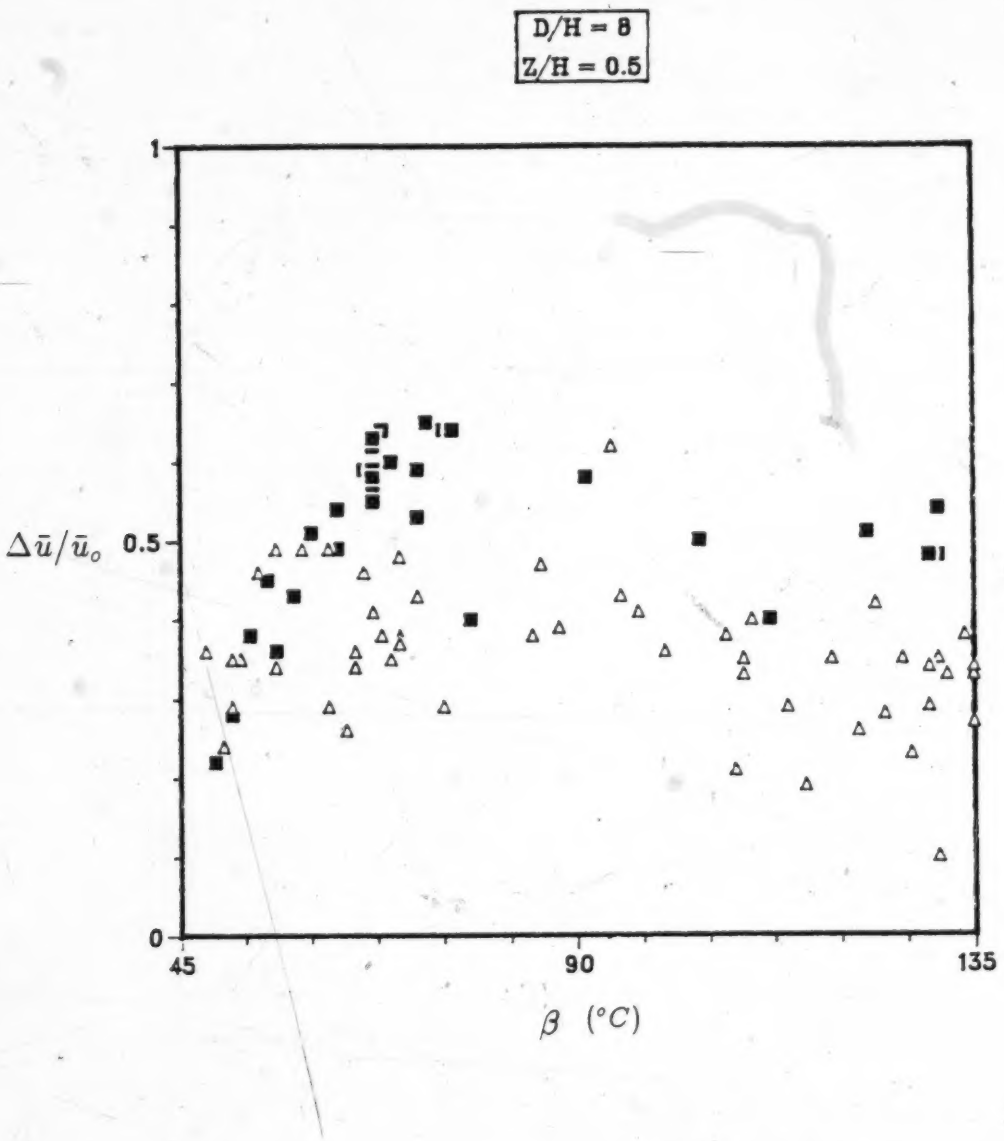

Figure 6.5 Wind reduction as a function of β for the small plot at two values of surface roughness: △ $\frac{H}{z_o} = 25$; ■ $\frac{H}{z_o} = 200$

6.2 Trends of w' in the quiet and turbulent zones

As many of the results of this experiment are analyzed in terms of the quiet and turbulent zones, it is first important to show the existence of these zones for the two square plots considered. One manifestation of the difference in the degree of turbulence between these zones is the magnitude of the vertical velocity fluctuation w' compared to the open value, here expressed as scaled standard deviations of w', $\frac{\Delta\sigma_w}{\sigma_{wo}}$. Positive (negative) values imply decreased (increased) turbulence in the plot relative to the upstream value. The contrast of values for the big and small plots is explicit in Figure 6.6. For the entire range of atmospheric stability shown, the middle of the big plot was consistently in the turbulent zone. For the small plot, its center was most of the time in the quiet zone. Hereafter, the middle of the small plot is termed the *quiet* zone and that of the big plot the *turbulent* zone. A definite trend with $\frac{H}{-L}$ cannot be identified with certainty for both cases.

The variation of the scaled σ_w with wind direction β was investigated in order to explain the scatter of points noted by the deviation bars. In Figure 6.7, aside from showing a clear trend with β both for stable and unstable stratification runs, there is a strong suggestion from the negative values of the scaled σ_w at $\beta = 45, 135$ that the extent of the quiet zone for the small plot is quite short, about $4H$, compared to Wilson's (1987) measurement of $7 - 8H$ for a straight porous fence in atmospheric flow. This is likely to be a manifestation of the *corner* effect observed by Gandemer (1979), which exacerbates turbulence generation by the fence and would probably shorten the horizontal extent of the quiet zone. In Figure 6.8 for the large plot,the

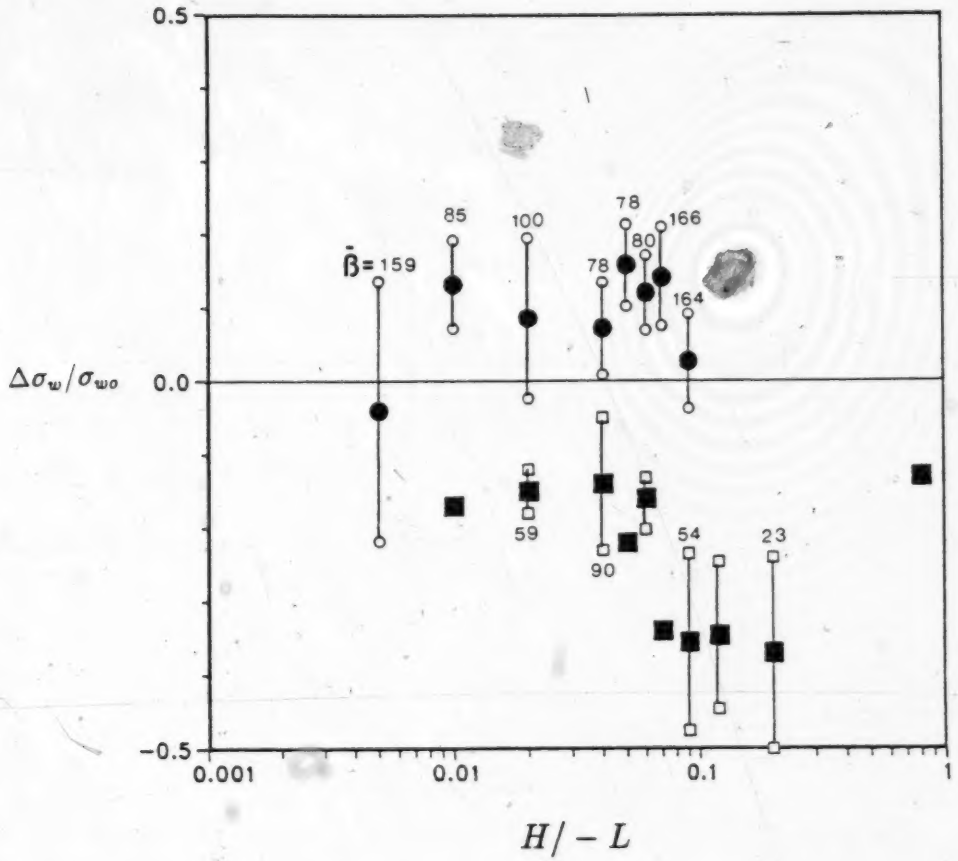

Figure 6.6 Scaled standard deviation of w' at two plot sizes: • $\frac{D}{H} = 8$; ■ $\frac{D}{H} = 16$, with atmospheric stability ranging from near-neutral to unstable and $\frac{z}{H} = 0.25$; $\frac{H}{z_o} = 200$.

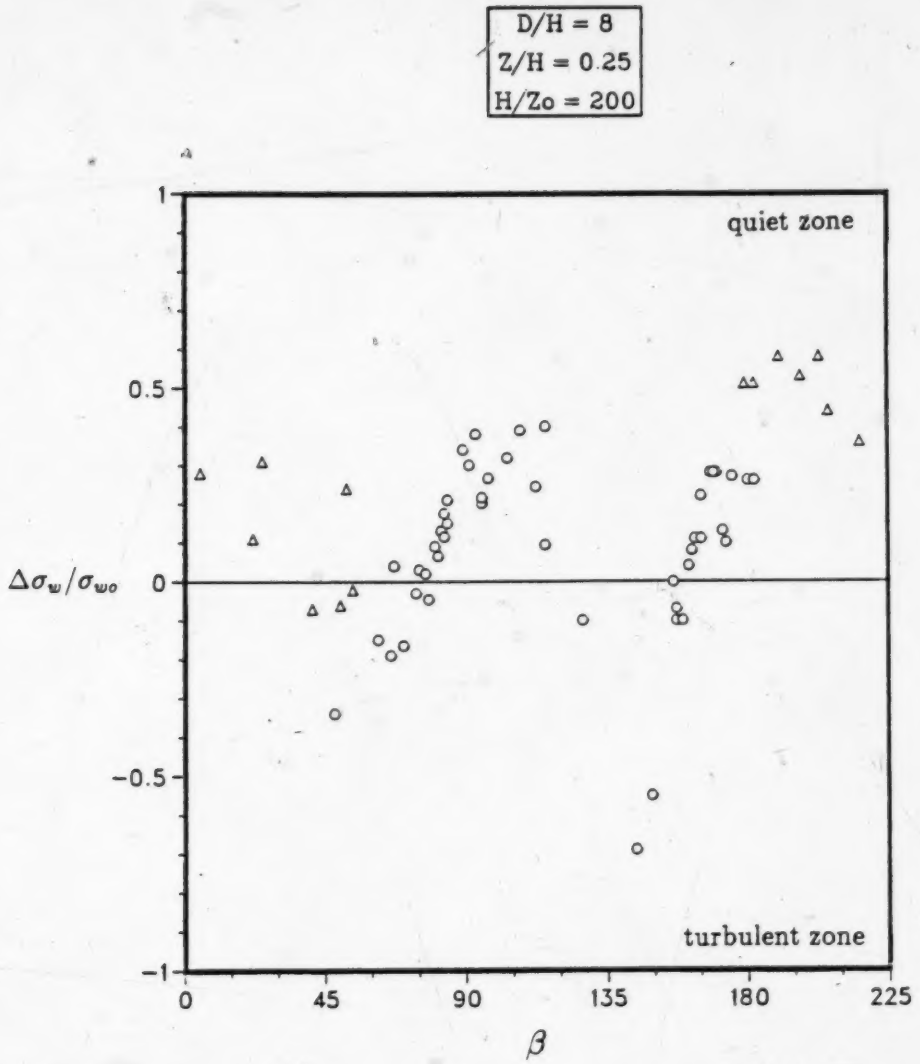

Figure 6.7 Scaled standard deviation of w' for the small plot as a function of β for two stability classes: ○ near-neutral to unstable; △ stable.

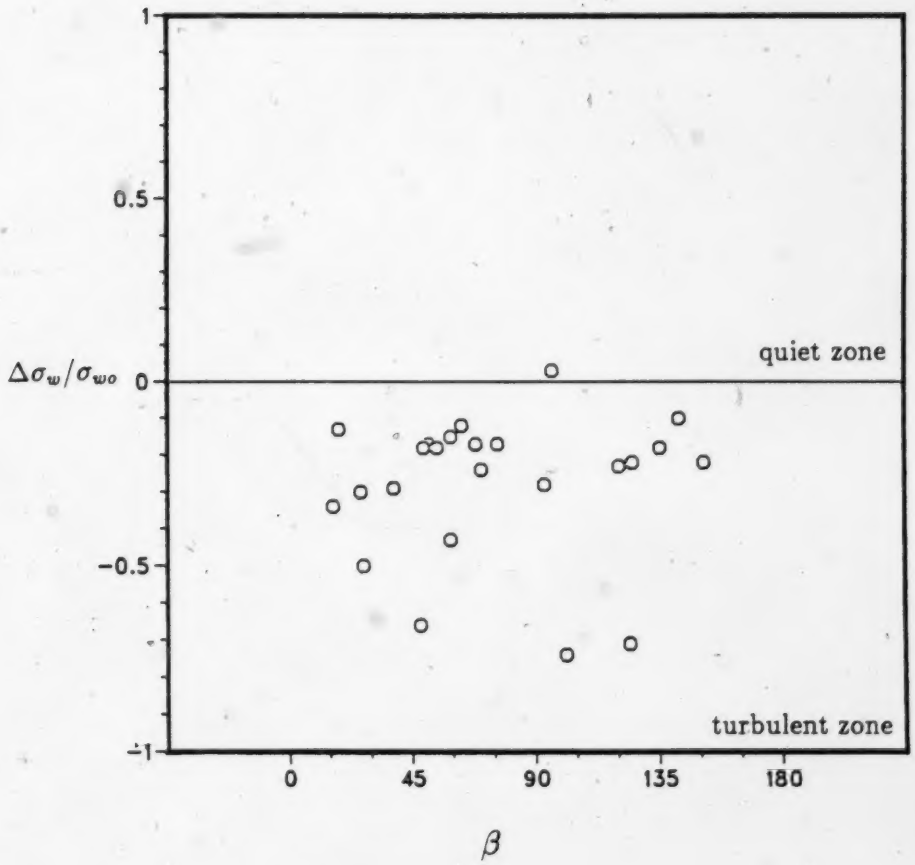

Figure 6.8 Standard deviation of w' for the big plot as a function of β for near-neutral to unstable runs.

negative values of the scaled σ_w show that at $\frac{z}{H} \approx 8$, eddies more energetic than upstream prevail, and that the scaled σ_w was not sensitive to β.

6.3 Trends in $\Delta\bar{T}_{eq}/T_{eq*}$

Recalling the sign conventions for fluxes set in Section 3.3.3 and the definitions of Q_H, Q_{LE}, L, T_{eq*} (Equations 3.1, 3.2, 2.32, 3.7), and noting that Δ denotes difference from upstream value (tower - plot), it will be seen that for daytime runs when conditions are generally lapse and the total energy flux $(Q_H + Q_{LE})$ is positive, $T_{eq*} < 0$, and $\frac{H}{L} < 0$. At night when stable stratification prevails so that the fluxes of sensible and latent heat are both directed downwards, T_{eq*} turns positive with $\frac{H}{L}$. Positive values of $\Delta\bar{T}_{eq}/T_{eq*}$ are therefore indicative of warming in T_{eq} in the plot during the day and cooling at night. Negative values indicate daytime cooling and nighttime warming in T_{eq} in the plot relative to that upstream. In reality, the shift in direction of the surface energy fluxes does not take place simultaneously but passes through a gradual period of transition. At sundown when the ground starts to radiate heat to the cold sky so that $Q_H < 0$, evaporation may still proceed for a few more hours until dewfall. In this case, $\frac{H}{L}$ is positive but T_{eq*} may still be negative on account of the large magnitude of Q_{LE} relative to Q_H. Table 6.1 summarizes the interpretation of the scaled T_{eq} based on the possible combinations of fluxes and derived variables. For a given value of $\frac{H}{L}(+)$, it is possible to interpret the sign of the scaled T_{eq} in two quite opposite ways. Inclusion of transition runs may therefore tend to confuse any correlation with atmospheric stability that may actually exist. Partly for this reason, those runs in which $\frac{H}{L} > 0$ but $T_{eq*} < 0$

were not included in the analysis. Another reason of equal importance relates to the intermittency observed during this period. In the late afternoon when winds start to settle, the calm is punctuated by bursts of activity evidenced by the very irregular profiles of wind and temperatures that were obtained.

Table 6.1 Scaled T_{eq} interpretation

	Q_H	Q_{LE}	$(Q_H + Q_{LE})$	H/L	T_{eq}.	$\Delta\bar{T}_{eq}/T_{eq}$.	Interpretation
Daytime	+	+	+	-	-	+	w
(unstable)						-	c
Night	-	-	-	+	+	+	c
(stable)						-	w
Transition	-	+	+	+	-	+	w
						-	c

w=warming in T_{eq} in plot relative to tower

c=cooling in T_{eq} in plot relative to tower

6.3.1 Influence of $\frac{D}{H}$

The daytime trends of warming in T_{eq} in the center of the small plot and cooling in the center of the big plot predicted in Section 3.3.3 were consistently observed in the August (Figure 6.9) and April-May (Figure 6.10) experiments. For the moment, the influence of $\frac{H}{L}$ will be ignored and we will concentrate on the magnitude of the scaled change in T_{eq}.

It is clear from Section 3.3.3 that where the conditions of reduced windspeed and less energetic eddies prevail, a situation is created wherein coupling of the air

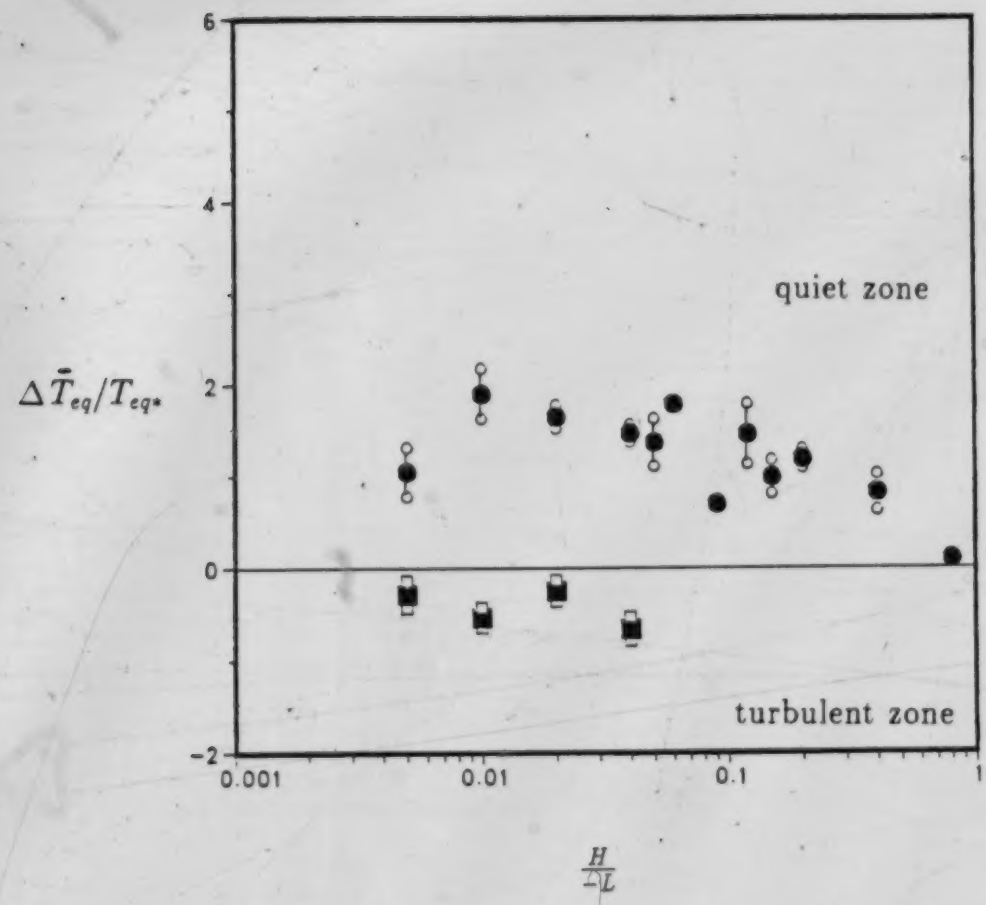

Figure 6.9 Scaled T_{eq} at two plot sizes: $\bullet \frac{D}{H} = 8$; $\blacksquare \frac{D}{H} = 16$ with atmospheric stability ranging from near-neutral to unstable and $\frac{z}{H} = 0.5$; $\frac{H}{z_o} = 25$.

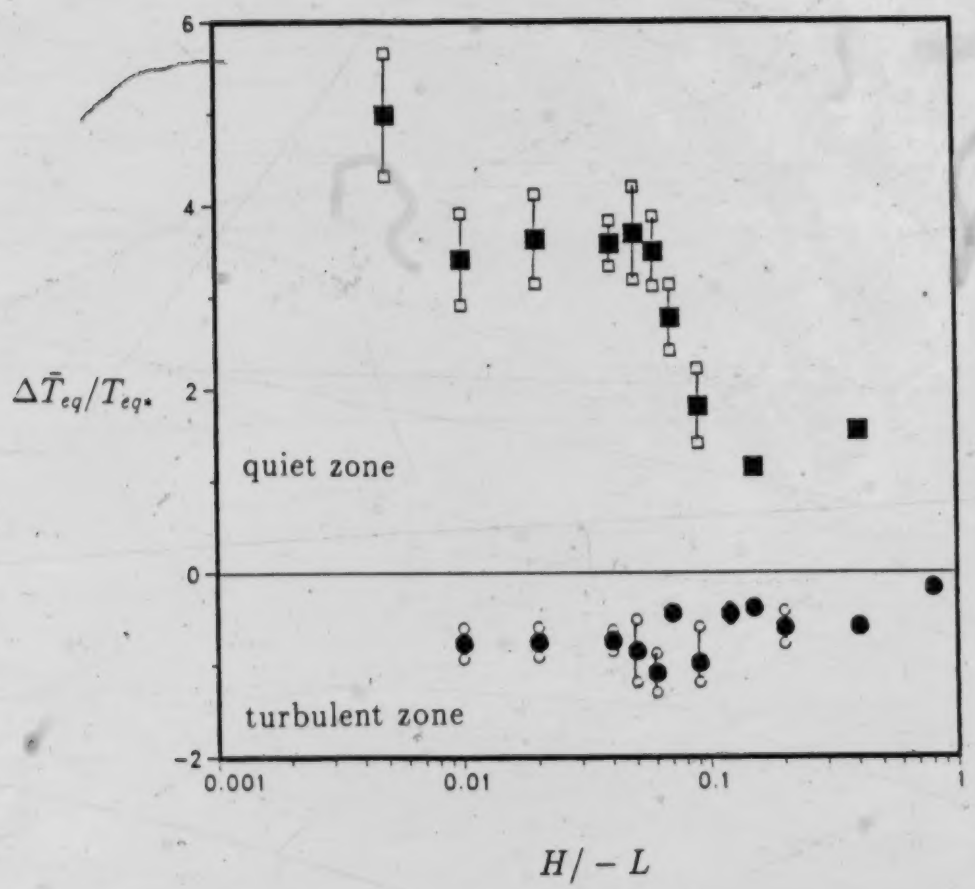

Figure 6.10 Scaled T_{eq} at two plot sizes: ■ $\frac{D}{H} = 8$; • $\frac{D}{H} = 16$. $[\frac{z}{H} = 0.25$; $\frac{H}{z_o} = 200]$.

mass in the lee with the cooler becomes limited. Vertical gradients in total energy are created, strong close to the ground and growing weaker towards the edge of the quiet zone. As a result of the limited vertical mixing, the scaled T_{eq} increases, with a trend expected to follow closely that of the vertical gradients, that is, higher values deep within the quiet zone, decreasing towards the edge of the quiet zone and finally assuming negative values within the turbulent zone. As the observation point is therefore moved from the quiet zone to the turbulent zone, as was done when comparing measurements in the small and big plots (in this case, for $\frac{D}{H} = 8, 16$), the trends of daytime warming and cooling in T_{eq} as shown in Figures 6.9 and 6.10 are qualitatively expected outcomes. Similar results are expected in the small plot if the measurement height is raised from, say, $0.5H$ to H.

6.3.2 Influence of $\frac{H}{L}, \frac{H}{z_o}, \frac{z}{H}$

In the literature, the turbulence of the approach flow (which depends on surface roughness and atmospheric stability) has been suggested to influence the horizontal extent of the quiet zone. For a flow under very strong convection (influence of Q_H dominates over u_* so that $|\frac{H}{L}|$ is big), and over rough terrain, the extent of the quiet zone has been found to be shorter: reattachment point at smaller x for a solid fence (Jacobs, 1980); faster momentum recovery for a porous fence (Raine and Stevenson, 1977); and a shorter extent of the warmer zone in the lee of shelterbelts during the day (Woodruff et al., 1959). In this study, with the measurements mostly done at points definitely deep within the quiet zone (small plot) and turbulent zone (big plot), the specific point of changeover from one zone to the other cannot be

pinpointed but can just be inferred from the results based on two markers $\frac{z}{H} = 4$ and $\frac{z}{H} = 8$. Figures 6.11 and 6.12 compare respectively the magnitudes of daytime warming in T_{eq} in the small plot and the daytime cooling in the big plot. Although plotted against $\frac{H}{-L}$, the two figures also incorporate variations in $\frac{H}{z_o}$ and $\frac{z}{H}$, viz., for the given range of $\frac{H}{-L}$, comparison of the August (•) with the April-May (■) results involve an eight-fold increase in $\frac{H}{z_o}$, from 25 to 200; and a 50% decrease in $\frac{z}{H}$, from 0.50 to 0.25. The October experiment which was intended to separate these two factors by taking data at $\frac{H}{z_o} = 200, \frac{z}{H} = 0.5$ was, as explained, excluded from analysis. Thus, if the magnitude of $|\Delta\bar{T}_{eq}/T_{eq_\infty}|$ is to be used as an indicator of the degree of the leeward protection provided by the fence, it is logical to expect that the April-May data which were taken at a lower measurement height and smoother surface should give values of the scaled T_{eq} much higher than those of August. This expectation is realized in the data of Figure 6.11 for runs taken under near-neutral conditions ($\frac{H}{-L} < 0.1$). The magnitudes of the scaled T_{eq} were almost doubled as $\frac{H}{z_o}$ increased (8x) and $\frac{z}{H}$ decreased (2x). Furthermore, the April-May data showed a more pronounced dependence on $\frac{H}{-L}$. However, with increasing instability ($\frac{H}{-L} \to 1$) the two curves showed a common tendency to decrease until they finally converged at a rather low value of the scaled T_{eq}. Again, if the magnitude of the scaled T_{eq} is to be translated into fence effects, the above trend with $\frac{H}{-L}$ in the quiet zone proves that indeed the influence of the fence becomes small as the flow becomes very unstable. In fact, this is actually a restatement of the observation in the literature regarding the influence of stratification on the horizontal extent ($\frac{x}{H}$) of the quiet zone.

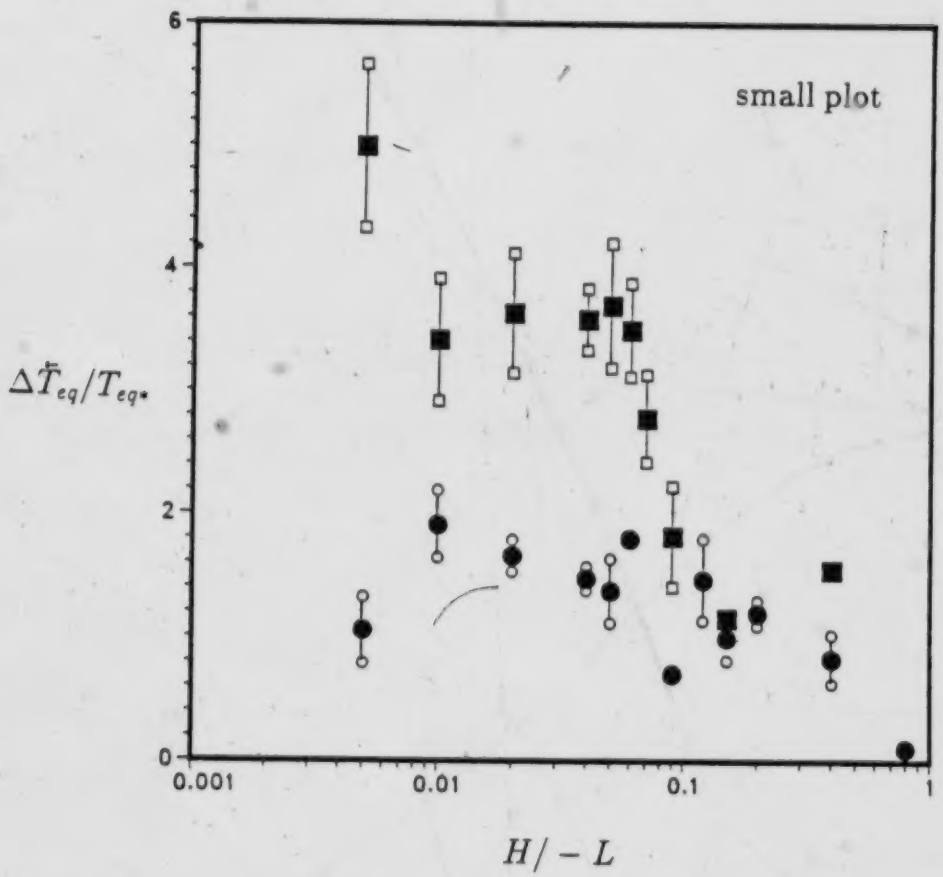

Figure 6.11 Scaled T_{eq} comparison in the small plot: ■ $\frac{z}{H} = 0.25$, $\frac{H}{z_o} = 200$; • $\frac{z}{H} = 0.5$, $\frac{H}{z_o} = 25$.

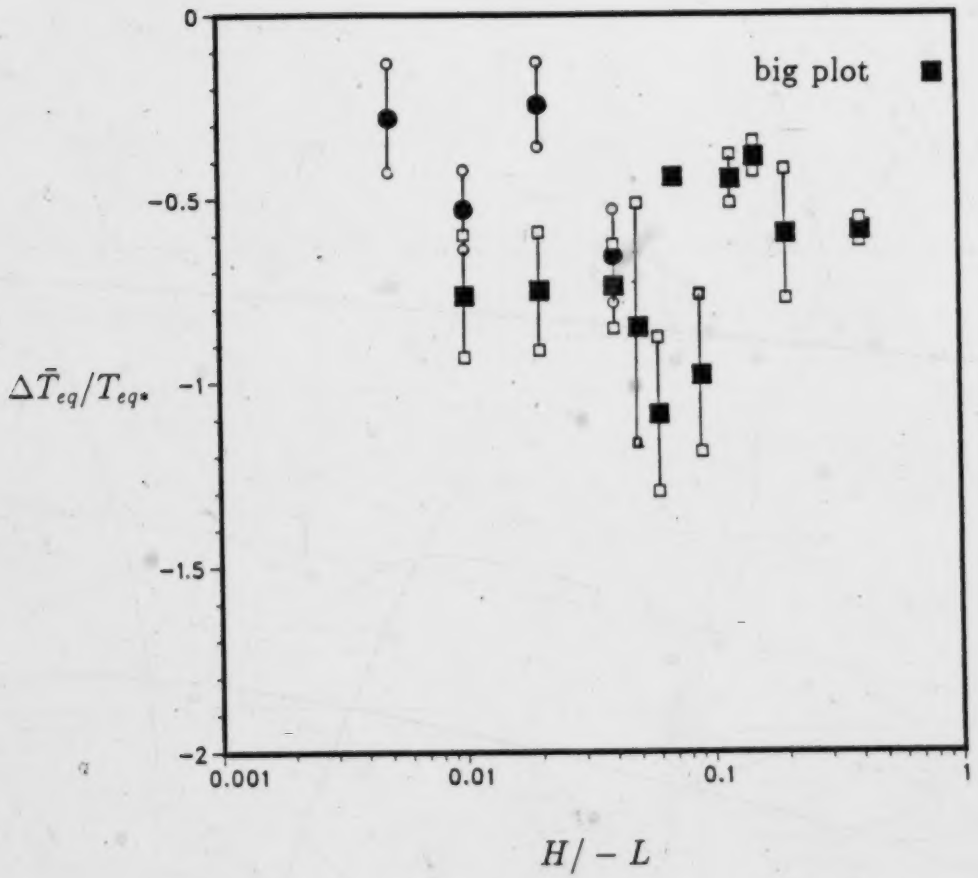

Figure 6.12 Scaled T_{eq} in the big plot. Notation same as in Figure 6.11.

In Figure 6.12, except for the consistently negative values of the scaled T_{eq} denoting daytime cooling, it may be said that the respective influences of $\frac{H}{-L}, \frac{H}{z_o}, \frac{z}{H}$ on the scaled T_{eq} are indistinguishable in the turbulent zone. A possible suggestion from this is that the additional turbulence that an unstable atmosphere or increased surface roughness may introduce into the wake zone is small and not of comparable magnitude to the turbulence generated by the fence itself. A carefully designed experiment intended to determine the relative magnitudes of the various terms in the TKE budget for the wake and quiet zones will be necessary to confirm this. To date, very little effort has been exerted in this respect.

6.3.3 Influence of $\beta, \frac{z}{H}$

The influence of β on mean wind reduction has been shown to be relatively significant for both plot sizes. Such a trend is the result of the vectorial nature of the wind. For a scalar such as total energy, this dependence on β is not expected to follow closely that of its vector (wind) counterpart, although the changes in the airflow are linked to the consequent behavior of these scalars. Figures 6.13 and 6.14 present the variations of wind reduction and scaled T_{eq} for the small and big plots at $\frac{z}{H} = 0.5, \frac{H}{z_o} = 25$. There is a discernible dependence of wind reduction on β for the small and big plots which are hardly defined for that of the scaled T_{eq}. At $\frac{z}{H} = 0.25$, Figure 6.15 shows that for both plot sizes and under a wide range of atmospheric stability, the scaled T_{eq} was not influenced by β.

The horizontal profiles of wind reduction and scaled T_{eq} obtained from u and T_{eq} mapping in the big plot are shown in Figure 6.16. The zone of maximum wind

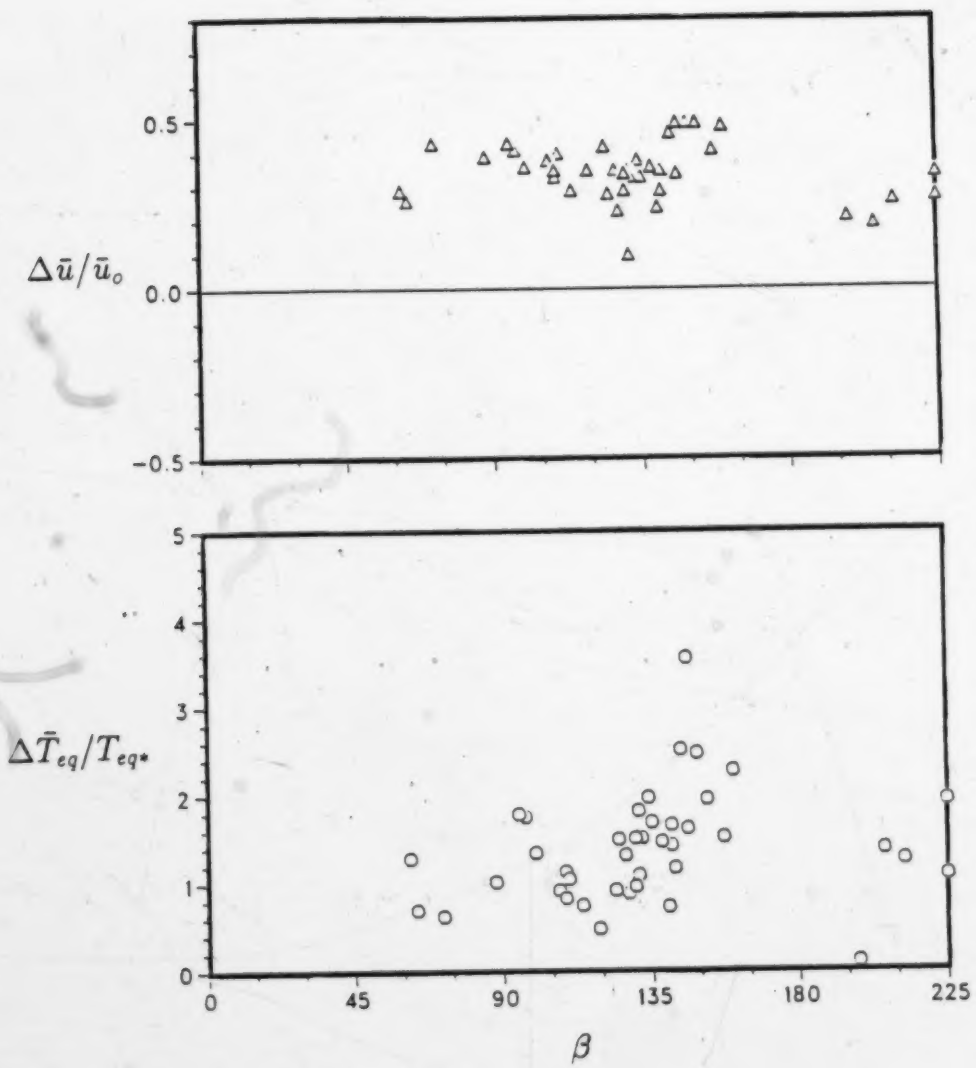

Figure 6.13 Influence of wind direction β on wind reduction and scaled T_{eq} in the small plot ($\frac{z}{H} = 0.5, \frac{H}{z_o} = 25$).

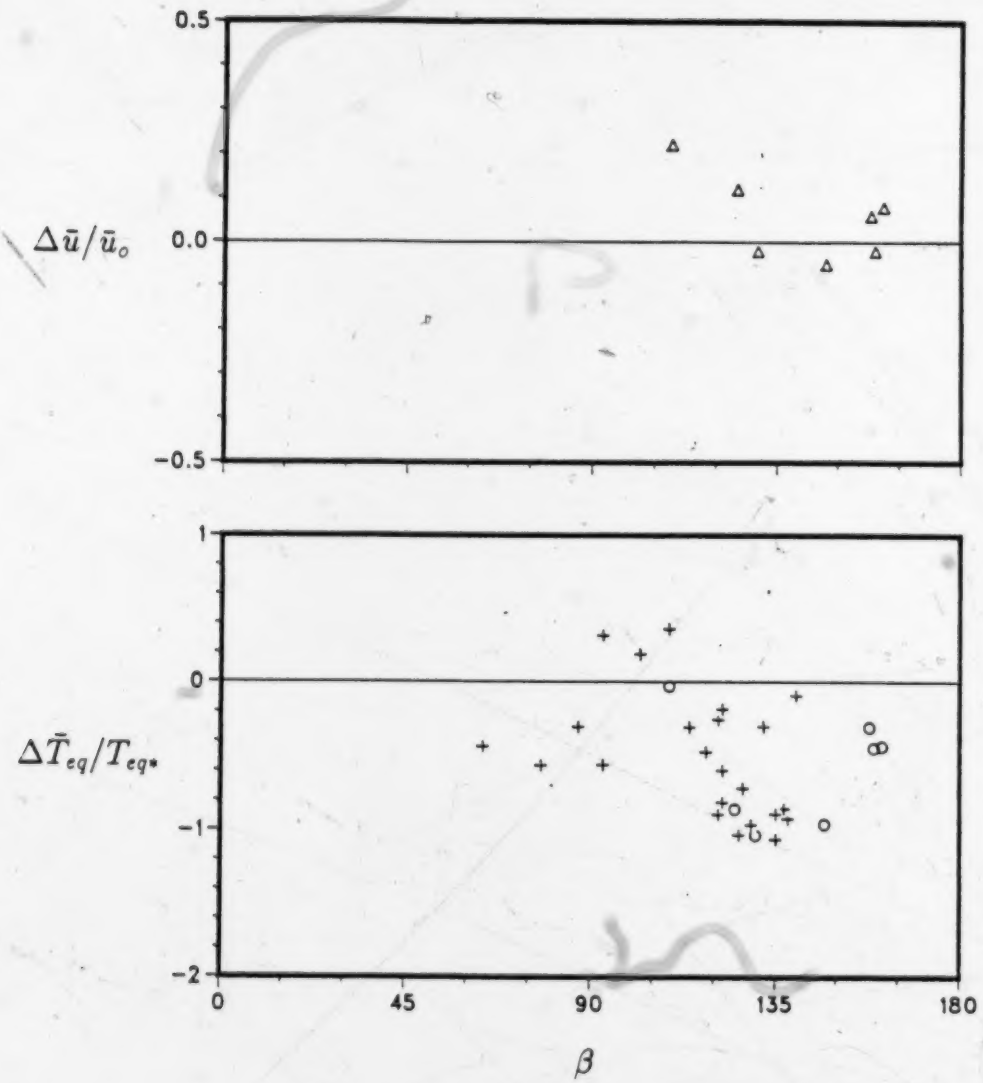

Figure 6.14 Influence of wind direction β on wind reduction and scaled T_{eq} in the big plot ($\frac{z}{H} = 0.5, \frac{H}{z_o} = 25$). Runs denoted by (+) have no corresponding wind data.

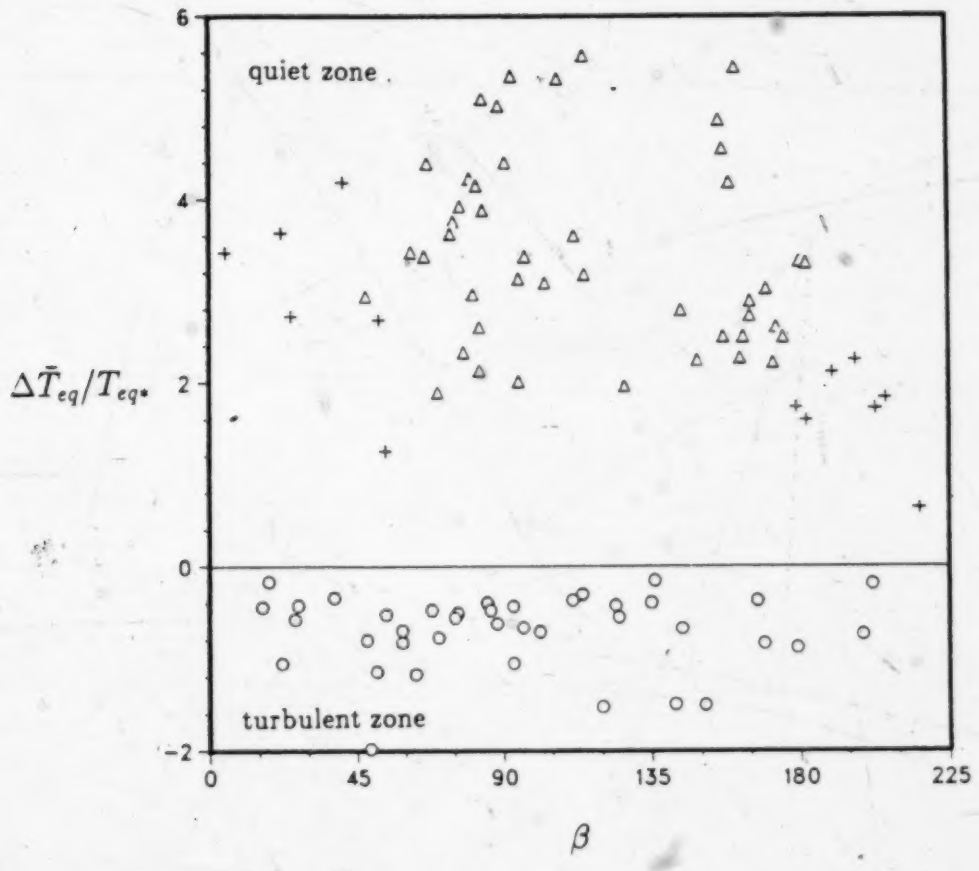

Figure 6.15 Influence of β on scaled T_{eq} for the small plot ($\triangle$ unstable; + stable) and big plot ($\circ$ unstable stratification), with $\frac{z}{H} = 0.25$, $\frac{H}{z_o} = 200$.

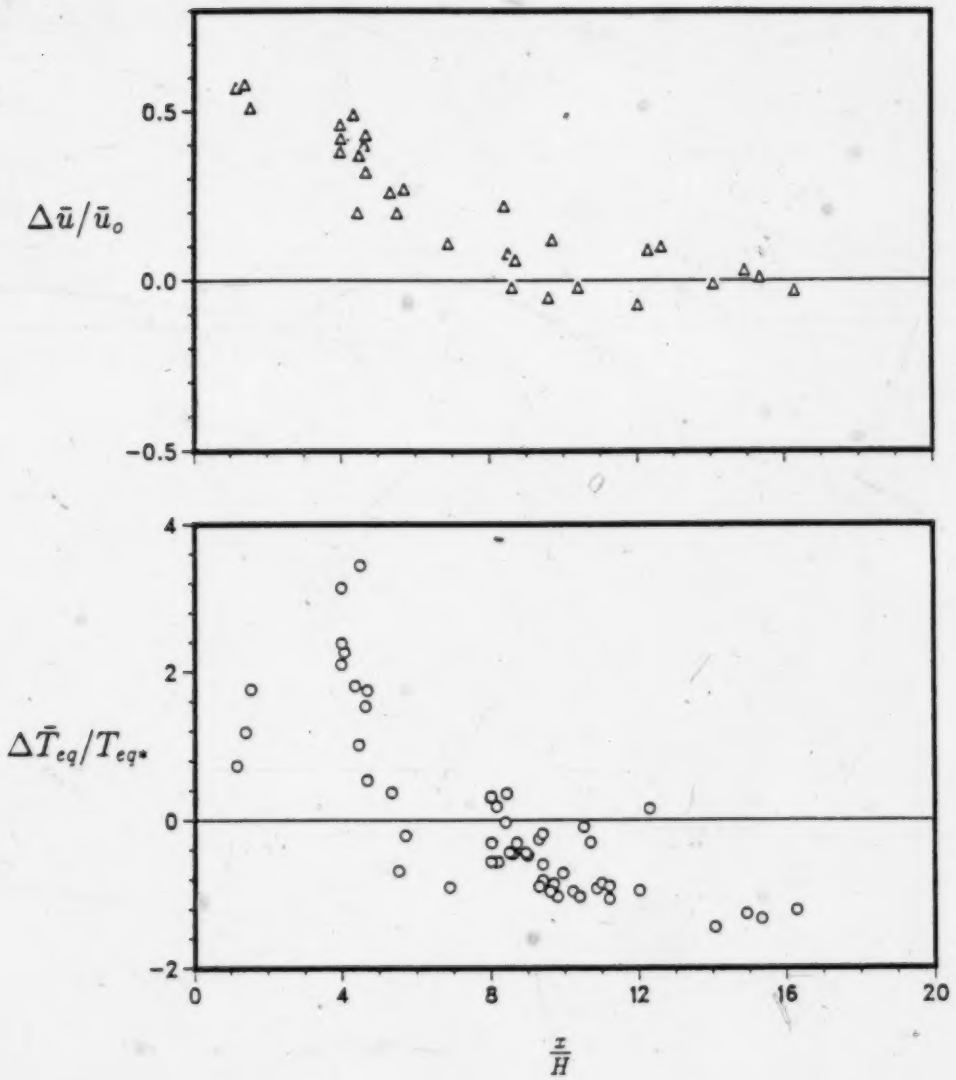

Figure 6.16 Horizontal profiles of wind reduction and scaled T_{eq} based on measurements in the center and four quadrants of the big plot ($\frac{x}{H} = 0.5, \frac{H}{z_o} = 25$).

reduction in the plot did not correspond to that of maximum increase in scaled T_{eq} as the data at $\frac{z}{H} = 1$ show. However, this need not be surprising given the different mechanisms at work. At $\frac{z}{H} = 1; \frac{z}{H} = 1$, Wilson (1985b) noted that $\frac{\partial \bar{p}}{\partial x}$ (> 0) is very large so that the pressure term $-\frac{1}{\rho}\frac{\partial \bar{p}}{\partial x}$ in equation (3.1) acts to further retard the flow: the minimum velocity falls to the lee of the fence. For energy transport, there is no corresponding pressure-gradient term. The slight reduction in scaled T_{eq} at small $\frac{z}{H}$ may have resulted from mixing due to the turbulence shed by the fence elements. The length scale of turbulence at this point $(\frac{z}{H} = 1, \frac{z}{H} = 0.5)$ was most probably of the order of the fence interstices which is smaller than the length scale of the fence-top-generated turbulence. This might explain the observation that the scaled T_{eq} at $\frac{z}{H} = 1$, although small in magnitude, has a positive value, indicative of a quiet zone situation. At $\frac{z}{H} = 5$ and beyond, the scaled T_{eq} started to acquire negative values as large eddies from the fence-top started to dominate.

It will be recalled from the horizontal profile of the scaled T_{eq} for a straight fence (Figure 3.9) that the change-over from quiet to wake zone was speculated to occur at $\frac{z}{H} = 8$, following closely that of Raine and Stevenson's turbulence (u) measurements. For the square plot with the specifications in Figure 6.16, it seems by interpolation that this occurs at $\frac{z}{H} \approx 5$.

6.3.4 Trends in $\Delta T_{eq}/T_{eq*}$ under stable stratification

Towards midnight when both Q_H and Q_{LE} are directed downwards, so that $T_{eq*} > 0, \frac{H}{L} > 0$, the winds start to die down to such an extent that the accuracy of estimation of u_* and all the variables derived from it $(T_*, T_{eq*}, L, Q_H, Q_{LE})$ are compro-

mised. Taking night runs proved to be a frustrating experience. Strong temperature gradients were associated with extremely light winds and conversely, when moderate winds do manage to blow, the temperature gradients start to diminish. Thus, it was not surprising to find that upon imposing the rather stringent criteria for accepting runs set in Chapter 5, only half of the stable runs were considered acceptable. The scaled T_{eq} of these stable runs are plotted against $\frac{H}{L}$ in Figure 6.17. Despite the scarcity of data points, the following generalizations may be drawn:

1. The center of the small plot is cooler in T_{eq} and may be considered to be in the quiet zone. The temperature profiles upstream and inside the plot are both inverted (cooler at the ground and warmer aloft). With limited mixing in the quiet zone, the gradient in the plot is enhanced, leading to cooling in T_{eq} relative to the upstream value.

2. The center of the big plot is warmer in T_{eq} and may be considered in the turbulent zone. Again starting with two inverted T_{eq} profiles in and out of the plot, efficient mixing of air layers in the wake zone due to fence-top generated turbulence leads to decreased gradients in T_{eq}, leading to warming in T_{eq} relative to the upstream value. This observation proved to be contrary to what was expected at the onset of the experiment, that under stable conditions, the horizontal extent of the quiet zone would reach $\frac{x}{H} \approx 8$. Apparently, the fence-generated turbulence although small in magnitude becomes significant relative to stably stratified condition of the surrounding air. Hence, under the general situation of *calm* (i.e., very light winds), a turbulent zone is still

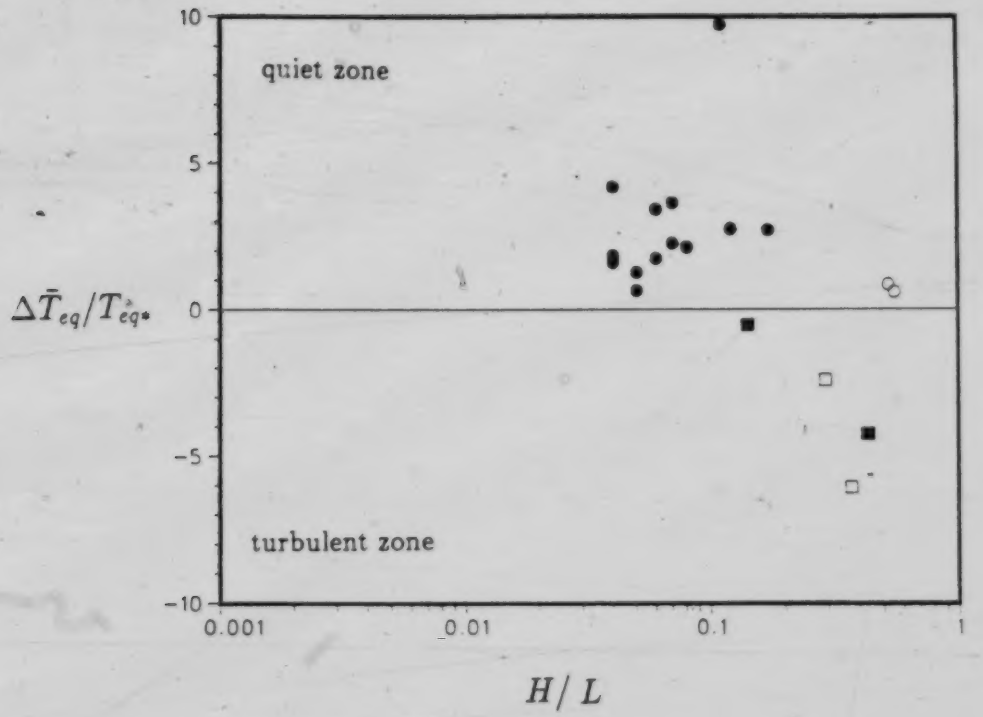

Figure 6.17 Variation of scaled T_{eq} with $\frac{H}{L}$ under stable stratification:
●■ $\frac{D}{H} = 8, 16$ $\frac{z}{H} = 0.25$ $\frac{H}{z_o} = 200$
○□ $\frac{D}{H} = 8, 16$ $\frac{z}{H} = 0.50$ $\frac{H}{z_o} = 25.$

generated in the big plot.

3. Differences in the scaled T_{eq} due to differences in $\frac{H}{z_o}$ and $\frac{z}{H}$ seem to be insignificant for stable runs. Data points taken at a higher elevation over a rough surface ($\frac{z}{H} = 0.5, \frac{H}{z_o} = 25$) are not distinguishable from those taken at $\frac{z}{H} = 0.25, \frac{H}{z_o} = 200$.

4. The pattern of decreasing influence of the fence as the atmosphere becomes very stable is weakly indicated at least for the small plot.

More data points are necessary to raise the level of confidence of the above qualitative assertions. As in all experimental studies of the stably stratified layers, aside from the difficulty of dealing with a process involving intermittency, the major constraint is instrumentation. However, it may be stated that the expectations of warming and cooling in the plot as measured by the formulation $\Delta\bar{T}_{eq}/T_{eq}$. and as outlined in Table 6.1 hold under conditions of stable stratification as well. If the data points in Figure 6.17 were to be plotted as a function of $\frac{z}{H}$, the trend would apparently follow that of the unstable case in Figure 6.16. As the observation point in the big plot is moved from $\frac{z}{H} = 4$ to $\frac{z}{H} = 8$, values of $\Delta\bar{T}_{eq}/T_{eq}$. would go from positive to negative, with the changeover in sign occuring anywhere between $\frac{z}{H} = 4$ and $\frac{z}{H} = 8$.

CHAPTER VII

SUMMARY

Notable results of this study are as follows:

1. From the horizontal profile of wind reduction, the mean windspeed was shown to be reduced less and the return to upstream value $\bar{u}_o$ was faster in the big plot than in the lee of a long straight fence. $\Delta\bar{u}_o/\bar{u}_o$ was a strong function of wind direction β for the big plot ($\frac{D}{H} = 16$) and slightly less so for the small plot ($\frac{D}{H} = 8$). A suggestion of three-dimensionality of the mean flow in the square-plot configuration is apparent in these results and arises from the small aspect ratio; the corner effect which sheds high-energy eddies into the quiet zone; and the confining effect of the fence which brings about a strong surface divergence.

2. In the small plot, $\Delta\bar{u}/\bar{u}_o$ at $\frac{z}{H} = 0.5$ was about 50% higher over a smooth surface ($\frac{H}{z_o} = 200$) than over a relatively rough surface ($\frac{H}{z_o} = 25$). No significant influence of atmospheric stability ($\frac{H}{L}$) was observed for near-neutral to unstable cases.

3. Turbulence (w') measurements showed that the center of the small plot ($\frac{z}{H} = 4$) was most of the time in the quiet zone (reduced vertical velocity fluctuations relative to the approach flow) and that of the big plot ($\frac{z}{H} = 8$) was always in the turbulent zone at all values of β. In the small plot, $\Delta\sigma_w/\sigma_{wo}$ was sensitive to β, becoming negative (turbulent zone situation) at β= 45, 135, again in agreement with the observed corner effects.

4. The scaled change in equivalent temperature, $\Delta\bar{T}_{eq}/T_{eq}$., was consistently positive (warming in T_{eq}) in the center of the small plot and negative in the center of the big plot for all daytime unstable runs ($\frac{H}{L} < 0$). Nightime stable runs showed the reverse. The magnitude of the change in scaled T_{eq} in the small plot was observed to be influenced by $\frac{z}{H}$ and $\frac{H}{z_o}$ (bigger at lower measurement height and smoother surface) at near-netral stratification, but with increasing instability ($\frac{H}{L} \rightarrow -1$), $|\Delta\bar{T}_{eq}/T_{eq}.| \rightarrow 0$ regardless of the values of $\frac{z}{H}$ or $\frac{H}{z_o}$. This suggests decreasing aerodynamic fence effect and implies a shorter extent of the quiet zone with increasing instability. The influence of $\frac{z}{H}$, $\frac{H}{z_o}$ and $\frac{H}{L}$ were not distinguishable in the wake zone.

5. Horizontal profiles of the scaled T_{eq} set the extent of the quiet zone in the big plot to be $\frac{z}{H} \approx 5$, in close agreement with the $\Delta\sigma_w/\sigma_{wo}$ interpolation.

6. Measurements under stable stratification ($\frac{H}{L} > 0$) showed the small plot in the quiet zone (cooling in T_{eq}) and the big plot in the wake zone (warming in T_{eq}). Apparently, the fence-generated turbulence although small in magnitude is still significant relative to the stably-stratified surrounding air so that under

the general situation of *calm*, a turbulent zone was still generated. Since T_{eq} is by definition negative for unstable (daytime) and positive for stable (night) runs, the expectations of warming and cooling in T_{eq} in the plot based on the diffusivity concept in the quiet/wake zones holds for the entire range of atmospheric stability.

One direct application of these results is that in the agronomic practice of sheltering, rather small plots (or tall fences) have to be employed in order to derive a shelter benefit other than that of a reduction in windspeed. While a square-plot configuration provides protection from the wind at all β, the shelter itself may generate turbulence which is advected into the plot if the plot size is not carefully considered. Consequences of increased turbulence on the microclimate may include increased evapotranspiration, decreased protection for livestock, fruit windrub, etc.

While the trends in the change in equivalent temperature determined in this study are a first step in describing the aerodynamically-induced microclimatic changes in a square-fenced plot, it will be noted that some of the results were left unexplained. The reason is that the available information on the shelter/fence aerodynamics in the literature concern two-dimensional treatment of the problem which is not sufficient to explain the obviously three-dimensional flow in a square plot. Rigorous measurements of the component terms of the TKE budget in this plot configuration are necessary.

BIBLIOGRAPHY

Alcorn, K.L. and M.W. Dodd. 1984. Windbreaks for conservation: an annotated bibliography. Calif. Dept. Conserv., Div. of Land Resource Protection. 145 pp.

Black, T.A. and K.G. McNaughton. 1972. Psychrometric apparatus for Bowen-ratio determination over forests. Boundary-Layer Meteorol. 2:246-254.

Bradley, E.F. 1968. A micrometeorological study of velocity profiles and surface drag in the region modified by a change in surface roughness. Quart. J. R. Meteorol. Soc. 94:361-379.

Businger, J.A. 1975. Aerodynamics of vegetated surfaces. In: de Vries, D.A. and N.H. Afgan (eds). Heat and Mass Transfer in the biosphere. Part I. Transfer processes in the plant environment. Scripta Book Co. Washington D.C. 139-165.

Businger, J.A. 1982. Equations and concepts. In: Nieuwstadt, F.T.M. and H. van Dop (eds). Atmospheric Turbulence and Air Pollution Modelling. D. Reidel Publishing Co. Holland. 358 pp.

Busch, N.E. 1973. On the mechanics of atmospheric turbulence. In: Haugen, D.A. (ed). Workshop on Micrometeorology. American Meteorological Society. Boston. 392 pp.

Calder, K.L. 1966. Concerning the similarity theory of A.S. Monin and A.M. Obukhov for the turbulent structure of the thermally stratified surface layer of the atmosphere. Quart. J. R. Meteorol. Soc. 92:141-146.

Campbell, G.S. 1977. An Introduction to Environmental Biophysics. Springer-Verlag. New York.

Cellier, P. 1986. On the validity of flux-gradient relationships above very rough surfaces. Boundary-Layer Meteorol. 36:417-419.

Counihan, J., J.C.R. Hunt and P.S. Jackson. 1974. Wakes behind two-dimensional surface obstacles in turbulent boundary layers. J. Fluid Mech. 64:529-563.

Donaldson, C. 1973. Construction of a dynamic model of the production of atmospheric turbulence and the dispersal of atmospheric pollutants. In: Haugen, D.A. (ed). Workshop on Micrometeorology. American Meteorological Society. Boston. 392 pp.

Dyer, A.J. 1974. A review of flux-profile relationships. Boundary-Layer Meteorol. 7:363-372.

Dyer, A.J. and E.F. Bradley. 1982. An alternative analysis of flux- gradient relationships at the 1976 ITCE. Boundary-Layer Meteorol. 23:3-19.

Dyer, A.J. and B.B. Hicks. 1970. Flux-gradient relationships in the constant-flux layer. Quart. J. R. Meteorol. Soc. 96:715-721.

Elliot, W.P. 1958. The growth of the internal boundary layer. Trans. Amer. Geophys. Union. 39:1048-1054.

Finnigan, J.J. and E.F. Bradley. 1983. The turbulent kinetic energy budget behind a porous barrier: an analysis in streamline coordinates. J. Wind Eng. Indus. Aero. 15:157-168.

Gandemer, J. 1979. Wind shelters. J. Indus. Aero. 4:371-389.

Hagen L.J. and E.L. Skidmore. 1971. Turbulent velocity fluctuations and vertical flow as affected by windbreak porosity. Trans. ASAE. 14:634-637.

Hagen, L.J., E.L. Skidmore, P.M. Miller and J.E. Kipp. 1981. Simulation of effect of wind barriers on airflow. Trans. ASAE. 24:1002-1008.

Haugen, D.A.(ed). 1973. Workshop on Micrometeorology. American Meteorological Society. Boston. 392 pp.

Heissler, G.M. and D.R. de Walle. 1987. Effects of windbreak structures on windflow. In: Hintz, D.L.(ed) Windbreak Technology (to be published).

Hinshaw, R. and L.J. Fritchen. 1970. Diodes for temperature measurement. J. Appl. Meteorol. 9:530-532.

Högstrom, U. 1985. Von Karman's constant in atmospheric boundary layer flow: re-evaluation. J. Atmos. Sci. 42:263-270.

Iribarne, J.V. and W.L. Godson. 1973. Atmospheric Thermodynamics. D. Reidel Publishing Co. Holland. 222 pp.

Jacobs, A.F.G. 1984. Wind reduction near the surface behind a thin solid fence. Boundary-Layer Meteorol. 33:157-162.

Jacobs, A.F.G. and E. Schols. 1986. Surface roughness parameter estimated with a drag technique. J. Climat. Appl. Meteorol. 25:1577-1582.

Kaiser, H. 1959. Die strömung an windshutzsreifen. Cited by Plate (1971a).

Klug, W. 1967. Determination of turbulent fluxes of heat and momentum from the wind profile. Quart. J. R. Meteorol. Soc. 93:101-104.

Logan, E. and G.H. Fichtl. 1975. Rough to smooth transition of an equilibrium neutral constant stress layer. Boundary- Layer Meteorol. 8:525-528.

McAneney, K.H. and M.J. Judd. 1987. Comparative shelter strategies for kiwifruit: a mechanistic interpretation of wind damage measurements. Agric. For. Meteorol. 39:225-240.

McBean G.A. 1971. The variations of the statistics of wind, temperature and humidity fluctuations with stability. Boundary-Layer Meteorol. 1:438-457.

McCaughey, J.H. and J.I. Walker. 1977. A note on temperature and humidity profile measurement over forests using diodes. J. Appl. Meteorol. 16(1):106-109.

McNaughton, K.G. 1983. The direct effect of shelter on evaporation rates: theory and experimental test. Preprints for Bulls Sympo., N.Z.

McNaughton, K.G. 1985. Effects of windbreaks on microclimate. In: J.R. Brandle and D.L. Hintz (eds). Shelter Technology (to be published).

Miller, D.R., N.J. Rosenberg and W.T. Bagley. 1973. Soybean water-use in the shelter of a slat-fence windbreak. Agric Meteorol. 11:405-418.

Monin, A.S. and A.M. Obukhov. 1954. Basic laws of turbulent mixing in the ground layer of the atmosphere. Akademia Nauk SSR. Leningrad. Geofizicheskii Institut. Trudy. 24(151)163-187.

Mulhearn, P.J. and E.F. Bradley. 1977. Secondary flows in the lee of porous shelterbelts. Boundary-Layer Meteorol. 12:75-92.

Nägeli, W. 1953. Research on wind conditions in the vicinity of reed screens. Mitt. Schweiz. Anst. Forstl. Versuchswes. Cited by van Eimern et al. (1964).

Nieuwstadt, F.T.M. 1977. The computation of the friction velocity u_* and the temperature scale T_* from temperature and velocity profiles by least-squares methods. Boundary-Layer Meteorol. 14:235-246.

Nieuwstadt, F.T.M. 1984. The turbulent structure of the stable, nocturnal boundary layer. J. Atmos. Sci. 41(14):2202-2216.

Ogawa, Y. and P.G. Diosey. 1980. Surface roughness and thermal stratification effects on the flow behind a two-dimensional fence - I. Field study. Atmos. Environ. 14:1301-1308.

Panofsky, H.A., H. Tennekes, D.H. Lenschow and J.C. Wyngaard. 1977. The characteristics of turbulent velocity components in the surface layer under convective conditions. Boundary-Layer Meteorol. 11:355-361.

Pasquill, F. 1972. Some aspects of boundary layer description. Quart. J. R. Meteorol. Soc. 98:469-494.

Pasquill, F. 1974. Atmospheric Diffusion. 2nd ed. John Wiley and Sons. London. 429 pp.

Paulson, C.A. 1970. The mathematical representation of windspeed and temperature profiles in the unstable atmospheric surface layer. J. Appl. Meteorol. 9(6)857-861.

Paw U, K.T. 1987. Zero plane displacement and roughness length variation with stability as predicted by a turbulence closure model. Proc. 18th Conf. Agric. For. Meteorol. W. Lafayette, Indiana.

Perera, M.D.A.E.S. 1981. Shelter behind two-dimensional solid and porous fences. J. Wind Eng. Indus. Aero. 8:93-104

Philip, J.R. 1959. The theory of local advection: I. J. Meteorol. 16:535-547.

Plate. E.J. 1971a. The aerodynamics of shelterbelts. Agric. Meteorol. 8:203-222.

Plate, E.J. 1971b. Aerodynamic Characteristics of Atmospheric Boundary Layers. AEC Critical Review Series. Tennessee. 190 pp.

Raine, J.K. and D.C. Stevenson. 1977. Wind protection by model fences in a simulated atmospheric boundary layer. J. Indus. Aero. 2:159-180.

Rao, K.S. 1975. Effects of thermal stratification on the growth of the internal boundary layer. Boundary-Layer Meteorol. 8:227-234.

Rao, K.S., J.C. Wyngaard and O.R. Cote. 1974. Local advection of momentum, heat and moisture in micrometeorology. Boundary-Layer Meteorol. 7:331-348.

Raupach, M.R. and B.J. Legg. 1984. The uses and limitations of flux-gradient relationships in micrometeorology. Agric. Water Mgt. 8:119-131.

Richards, P.J., E.F. Kay, D. Russell and G.R.C. Wilson. 1985. Porous artificial windbreaks in oblique winds. Paper 67/84 for IPENZ Conf., Hastings, N.Z. Cited by Heissler and de Walle (1987).

Richardson, L.F. 1920. The supply of energy from and to atmospheric eddies. Proc. R. Soc. London Ser. A. 97:354-373.

Rosenberg, N.J. 1979. Windbreaks for reducing moisture stress. In B.J. Barfield and J.F. Gerber (eds.) Modification of the Aerial Environment of Plants. ASAE Monograph. Michigan. 538 pp.

Sargeant, D.H. 1965. Note on the use of junction diodes as temperature sensors. J. Appl. Meteorol. 4:644-646.

Sargeant, D.H. and C.B. Tanner. 1967. A simple psychrometric apparatus for Bowen-ratio determinations. J. Appl. Meteorol. 6:414-418.

Seginer, I. 1975a. Atmospheric stability effect on windbreak shelter and drag. Boundary-Layer Meteorol. 8:383-400.

Seginer, I. 1975b. Flow around a windbreak in oblique wind. Boundary-Layer Meteorol. 9:133-141.

Stearns, C.R. 1970. Determining surface roughness and displacement height. Boundary-Layer Meteorol. 1:102-111.

Sutton, O. 1953. Micrometeorology. McGraw-Hill. New York. 333 pp.

Tani, N. 1963. Bull. Nat. Inst. Agric. Sci. A. 10:1-99. Cited by Z. Uchijima. 1975. Maize and rice. In: Monteith, J.L. (ed) Vegetation and the Atmosphere. Vol II. Academic Press. New York.

Tanner, C.B. 1971. Application of psychrometry to micrometeorology. In: R.W. Brown and B.D. van Haveren (eds). Psychrometry in Water Relations Research. Proc. Sympo. Thermocouple Psychrometers. Utah State U. 342 pp.

Thom, A.S. 1975. Momentum, heat and mass exchange of plant communities. In: Monteith,J.L.(ed) Vegetation and the Atmosphere. Vol I. Academic Press, New York.

Thom, A.S., J.B. Stewart, H.R. Oliver and J.H.C. Gash. 1975. Comparison of aerodynamic and energy budget estimate of fluxes over a pine forest. Quart. J. R. Meteorol. Soc. 101:93-105.

Van Eimern, J., R.Karschon, L.A. Razumova and G.W. Robertson. 1964. Windbreaks and Shelterbelts. WMO Technical Note No. 59.

Webb, E.K. 1970. Profile relationships: the log-linear range and extension to strong stability. Quart. J. R. Meteorol. Soc. 96:67-90.

Wieringa, J. 1980. A re-evaluation of the Kansas mast influences on measurements and cup anemometer overspeeding. Boundary-Layer Meteorol. 18:411-430.

Wilson J.D. 1985a. Lecture notes in Meteo 525 (Micrometeorology), Div. of Meteorology, University of Alberta.

Wilson, J.D. 1985b. Numerical studies of flow through a windbreak. J. Wind Eng. Indus. Aero. 21:119-154.

Wilson, J.D. 1987. On the choice of windbreak porosity profile. Boundary-Layer Meteorol. 38:37-49.

Wilson, J.D. and F. Ustina. 1988. A perturbation analysis of turbulent flow through a porous barrier. Submitted to Quart. J. R. Meteorol. Soc.

Woodruff, N.P., R.A. Read and W.S. Chepil. 1959. Influence of a field windbreak on summer wind movement and air temperature. Kansas Tech. Bull. 100. 24 pp.

Wyngaard, J.C. 1973. On surface layer turbulence. In: Haugen, D.A. (ed). Workshop on Micrometeorology. American Meteorological Society. Boston. 392 pp.

Wyngaard, J.C. 1982. Boundary-layer modelling. In: Nieuwstadt, F.T.M. and H. van Dop (eds). Atmospheric Turbulence and Air Pollution Modelling. D. Reidel Publishing Co. Holland. 358 pp.

Yaglom, A.M. 1977. Comments on wind and temperature flux-profile relationships. Boundary-Layer Meteorol. 11:89-102.